Advances in Motion Estimators for

Applications in Computer Vision

by

Berkay Kanberoglu

A Dissertation Presented in Partial Fulfillment
of the Requirements for the Degree
Doctor of Philosophy

Approved November 2018 by the
Graduate Supervisory Committee:

David Frakes, Co-Chair
Pavan Turaga, Co-Chair
Andreas Spanias
Visar Berisha

ARIZONA STATE UNIVERSITY

December 2018

ABSTRACT

Motion estimation is a core task in computer vision and many applications utilize optical flow methods as fundamental tools to analyze motion in images and videos. Optical flow is the apparent motion of objects in image sequences that results from relative motion between the objects and the imaging perspective. Today, optical flow fields are utilized to solve problems in various areas such as object detection and tracking, interpolation, visual odometry, etc. In this dissertation, three problems from different areas of computer vision and the solutions that make use of modified optical flow methods are explained.

The contributions of this dissertation are approaches and frameworks that introduce i) a new optical flow-based interpolation method to achieve minimally divergent velocimetry data, ii) a framework that improves the accuracy of change detection algorithms in synthetic aperture radar (SAR) images, and iii) a set of new methods to integrate Proton Magnetic Resonance Spectroscopy (^{1}HMRSI) data into three-dimensional (3D) neuronavigation systems for tumor biopsies.

In the first application an optical flow-based approach for the interpolation of minimally divergent velocimetry data is proposed. The velocimetry data of incompressible fluids contain signals that describe the flow velocity. The approach uses the additional flow velocity information to guide the interpolation process towards reduced divergence in the interpolated data.

In the second application a framework that mainly consists of optical flow methods and other image processing and computer vision techniques to improve object extraction from synthetic aperture radar images is proposed. The proposed framework is used for distinguishing between actual motion and detected motion due to

misregistration in SAR image sets and it can lead to more accurate and meaningful change detection and improve object extraction from a SAR datasets.

In the third application a set of new methods that aim to improve upon the current state-of-the-art in neuronavigation through the use of detailed three-dimensional (3D) ^{1}H-MRSI data are proposed. The result is a progressive form of online MRSI-guided neuronavigation that is demonstrated through phantom validation and clinical application.

DEDICATION

To my parents and Jaye, for their support and patience since the beginning of this long journey.

Thank you...

Teşekkürler...

ACKNOWLEDGMENTS

My time at ASU has been challenging and long, but rewarding in the end. I would like to mention the people who have made a positive impact during my studies. Foremost, I have to thank Dr. David Frakes for making one of the most positive impacts on my life. This day wouldn't have come if he hadn't given me a second chance at this challenge by agreeing to be my advisor after I started my PhD. I'm forever grateful for his mentorship, understanding, and kindness. I would like to thank Dr. Pavan Turaga for his advising. His mentorship has been instrumental in my advancing to be a PhD candidate at first and then writing this dissertation and defending it. His invaluable input and encouragement have always been appreciated. I consider myself very fortunate to be among the very few who had them as mentors. I would like to thank Dr. Andreas Spanias and Dr. Visar Berisha for taking the time to be in my dissertation committee. Their valuable recommendations and support made the conclusion of this challenge much easier. I would also like to mention Dr. Josef Debbins who was my advisor during my masters studies.

I'm grateful to Science Foundation of Arizona for funding my research when I first started my studies. I'd like to thank SenSIP center at ASU for making it possible for us to collaborate with Lockheed Martin.

From the IPALab, I would like to mention Hooman Farsani and Dhritiman Das. Hooman has been good friend and a labmate whose dedication inspired me to do better. Even after Dhritiman's contributions came to an end for our project and he left for his own PhD studies, he stayed in contact with me. I appreciated our Skype calls.

Outside the lab, ASU Jujitsu club has been my escape from the pressure of

TABLE OF CONTENTS

LIST OF TABLES

LIST OF FIGURES

Chapter 1

INTRODUCTION

Motion estimation and analysis are important objectives in the field of computer vision. Many applications utilize optical flow methods as fundamental tools to analyze motion in images and videos. Today, motion estimation and optical flow can seem as interchangeable terms; however, there is a slight difference between the two. Ideally, an optical flow field would be the same as the actual motion field. In practice, we treat the opical flow field as the motion field in the scene. The real motion field is the projection of three dimensional (3D) motion on a 2D plane, i.e. image plane. On the other hand, an optical flow field is the displacement vectors of pixels between two images. Estimation of optical flow fields has been an active research area for over 35 years. Since the works of [Horn and Schunck (1980); Lucas and Kanade (1981)] marked the emergence of the field, there have been many improvements and surveys on the optical flow methods [Verri *et al.* (1989); Barron *et al.* (1994a); Beauchemin and Barron (1995); Baker and Matthews (2004); Bruhn *et al.* (2005); Fortun *et al.* (2015a)].

The contributions of this dissertation are mainly approaches and frameworks that can offer solutions to various computer vision/image processing problems. Some of the proposed frameworks include modified forms of optical flow as the chosen motion estimator because of its adaptability to different scenarios. The approaches and frameworks that are proposed in three distinct areas are:

(i) an optical-flow based framework for image interpolation that also minimizes resultant divergence in the interpolated data. Three-dimensional (3D) biomedical

1

image sets are often acquired with in-plane pixel spacings that are far less than the out-of-plane spacings between images. The resultant anisotropy, which can be detrimental in many applications, can be decreased using image interpolation. When acquired images are comprised of signals that describe the flow velocity of fluids, additional information is available to guide the interpolation process. The approach uses the additional flow velocity information to guide the interpolation process towards reduced divergence in the interpolated data.

(ii) a framework that mainly consists of optical flow methods and other image processing and computer vision techniques to improve object extraction from synthetic aperture radar images. In two-color multiview (2CMV) advanced geospatial information (AGI) products, temporal changes in synthetic aperture radar (SAR) images acquired at different times are detected, colorized, and overlaid on an initial image such that new features are represented in cyan, and features that have disappeared are represented in red. Accurate detection of temporal changes in 2CMV AGI products can be challenging because of 'speckle noise' susceptibility and false positives that result from small orientation differences between objects imaged at different times. Accordingly, 2CMV products are often dominated by colored pixels when changes are detected via simple pixel-wise cross-correlation. The state-of-the-art in SAR image processing demonstrates that generating efficient 2CMV products, while accounting for the aforementioned problem cases, has not been well addressed. The proposed framework aims to address these two problem cases. Before detecting temporal changes, speckle and smoothing filters mitigate the effects of speckle noise. To detect temporal changes, the framework includes various computer vision techniques like unsupervised feature learning algorithms in conjunction

with optical flow algorithms that track the motion of objects across time in small regions of interest. The proposed framework for distinguishing between actual motion and misregistration can lead to more accurate and meaningful change detection and improve object extraction from a SAR AGI product.

(iii) a set of new methods that aim to improve upon the current state-of-the-art in neuronavigation through the use of detailed three-dimensional (3D) ^{1}H-MRSI data. The correlation of metabolite profiles with specific regions of interest in anatomical tumor images can be useful in characterizing and treating heterogeneous tumors that appear structurally homogeneous. To establish that correlation, tissue samples must be neurosurgically extracted from specifically identified locations with high accuracy. Toward that end, a new neuronavigation technology that enhances current clinical capabilities in the context of neurosurgical planning and execution is presented. The proposed methods improve upon the current state-of-the-art in neuronavigation through the use of detailed 3D ^{1}H-MRSI data. 3D MRSI spectra are processed and analyzed, and specific voxels are selected based on their chemical contents. 3D neuronavigation overlays are then generated and applied to anatomical image data in the operating room. 3D MRSI based overlays provide comprehensive, quantitative visual cues and location information during neurosurgery. The newly proposed 3D methods also fully account for scanner calibration and leverage tools that we have now made publicly available. The result is a progressive form of online MRSI-guided neuronavigation that is demonstrated in this study through phantom validation and clinical application.

The remainder of this dissertation is structured as follows. In Chapter 2, a definition of the term optical flow will be given and one of the most well known optical

flow methods. This will provide a basis for the following chapters as most of the work described in this dissertation make use of the principles behind this method in some way. After providing the basis for optical flow, each chapter will provide background on the subject and methods as the addressed problems are from different areas. Chapter 3 describes the optical flow-based framework for interpolating minimally divergent velocimetry data. Chapter 4 presents a framework for SAR images using adaptive thresholding, well established image processing techniques, and optical flow. Chapter 5 describes a variant of the previous framework for improving change detection in SAR images using feature learning algorithms and optical flow in conjunction.and a one of its variants will be briefly described. In Chapter 6, a set of new methods to improve upon the current state-of-the-art in neuronavigation through the use of detailed three-dimensional (3D) ^{1}H-MRSI data is presented. A potential application of optical flow based interpolation is also discussed in the chapter. The general conclusions and suggestions for possible future research are discussed in Chapter 7.

Chapter 2

BACKGROUND

2.1 Optical Flow

Optical flow is the apparent motion of objects in image sequences that results from relative motion between the objects and the imaging perspective. In one canonical optical flow paper [Horn and Schunck (1980)], two kinds of constraints are introduced in order to estimate the optical flow: the *smoothness constraint* and the *brightness constancy constraint*. In this section, we give a brief overview of the original optical flow algorithm and the modified algorithm that was used in this project.

2.1.1 Theory

Optical flow methods estimate the motion between two consecutive image frames that were acquired at times t and $t + \delta t$. A flow vector for every pixel is calculated. The vectors represent approximations of image motion that are based in large part on local spatial derivatives. Since the flow velocity has two components, two constraints are needed to solve for it.

2.1.1.1 The Brightness Constancy Constraint

The brightness constancy constraint assumes that the brightness of a small area in the image remains constant as the area moves from image to image. Image brightness

at the point (x, y) in the image at time t is denoted here as $I(x, y, t)$. If the point moves by δx and δy in time δt, then according to the brightness constancy constraint:

$$\frac{dI}{dt} = 0. \tag{2.1}$$

This can also be stated as:

$$I(x + \delta x, y + \delta y, t + \delta t) = I(x, y, t). \tag{2.2}$$

If we expand the left side of Eq. 2.2 with a Taylor series expansion, then:

$$I(x, y, t) + \frac{\partial I}{\partial x}\delta x + \frac{\partial I}{\partial y}\delta y + \frac{\partial I}{\partial t}\delta t + \cdots = I(x, y, t), \tag{2.3}$$

where the ellipsis (...) denotes higher order terms in the expansion. After canceling $I(x, y, t)$ from both sides of the equation:

$$\frac{\partial I}{\partial x}\delta x + \frac{\partial I}{\partial y}\delta y + \frac{\partial I}{\partial t}\delta t + \cdots = 0. \tag{2.4}$$

We can divide this equation by δt, which leads to:

$$\frac{\partial I}{\partial x}\frac{dx}{dt} + \frac{\partial I}{\partial y}\frac{dy}{dt} + \frac{\partial I}{\partial t} = 0. \tag{2.5}$$

Substituting:

$$\alpha = \frac{dx}{dt} \ \ and \ \ \beta = \frac{dy}{dt},$$

the brightness constraint can be written in a more compact form:

$$I_x\alpha + I_y\beta + I_t = 0, \tag{2.6}$$

where $I_x = \partial I/\partial x$, $I_y = \partial I/\partial y$, and $I_t = \partial I/\partial t$. In this form α and β represent the image velocity components and (I_x, I_y) represents the brightness gradients.

2.1.1.2 The Smoothness Constraint

Fortunately, points from an object that is imaged in temporally adjacent frames usually have similar velocities, which results in a smooth velocity field. Leveraging this property, we can express a reasonable smoothness constraint by minimizing the sums of squares of the Laplacians of the velocity components α and β. The Laplacians are:

$$\nabla^2\alpha = \frac{\partial^2\alpha}{\partial x^2} + \frac{\partial^2\alpha}{\partial y^2}, \tag{2.7a}$$

$$\nabla^2\beta = \frac{\partial^2\beta}{\partial x^2} + \frac{\partial^2\beta}{\partial y^2}. \tag{2.7b}$$

2.1.1.3 Minimization

Optical flow assumes constant brightness and smooth velocity over the whole image. The two constraints described above are used to formulate an energy functional to be minimized:

$$\epsilon = \iint \left[(I_x\alpha + I_y\beta + I_t)^2 + \lambda^2 \left(\frac{\partial^2\alpha}{\partial x^2} + \frac{\partial^2\alpha}{\partial y^2} + \frac{\partial^2\beta}{\partial x^2} + \frac{\partial^2\beta}{\partial y^2} \right) \right] dx\,dy. \tag{2.8}$$

Using variational calculus, the Euler-Lagrange equations can be determined for this problem. Those equations need to be solved for each pixel in the image. Iterative methods are suitable to solve the equations since it can be very costly to solve them simultaneously. The iterative equations that minimize (2.8) are:

$$\alpha^{n+1} = \bar{\alpha}^n - \frac{I_x \left[I_x\bar{\alpha}^n + I_y\bar{\beta}^n + I_t \right]}{\lambda^2 + I_x^2 + I_y^2}, \tag{2.9a}$$

$$\beta^{n+1} = \bar{\beta}^n - \frac{I_y \left[I_x\bar{\alpha}^n + I_y\bar{\beta}^n + I_t \right]}{\lambda^2 + I_x^2 + I_y^2}, \tag{2.9b}$$
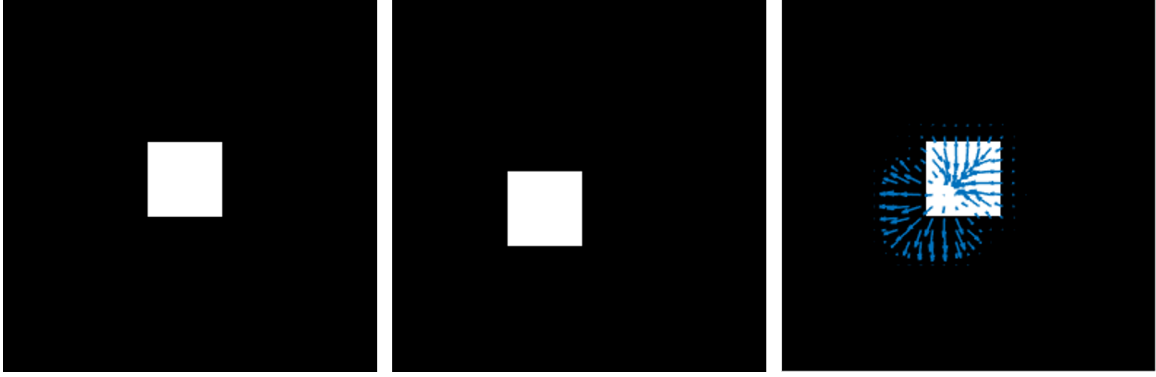
Figure 1. Image at time t (left), image at time $t + \delta t$ (middle), and Horn-Schunck optical flow field overlaid onto the first image (right).

where n denotes the iteration number and $\bar{\alpha}^n$ and $\bar{\beta}^n$ denote neighborhood averages of α^n and β^n. A sample result of this optical flow method is shown in Figure 1. More detailed information on the method can be found in [Horn and Schunck (1980)]. As this provides a basis for optical flow, the following chapters will provide background on separate subjects and build on this fundamental optical flow method in different applications.

2.2 Optical Flow with Relaxed Brightness Constraint

In the preceding section, two kinds of constraints were introduced in order to estimate the optical flow: the *smoothness constraint* and the *brightness constancy constraint*. This section gives a brief introduction to a modified optical flow algorithm that is employed in Chapters 4 and 5. The approach is explained more in detail in Chapter 4.

The brightness constancy constraint assumes that the brightness of a small area in the image remains constant as the area moves from image to image. Image brightness at the point (x, y) in the image at time t is denoted here as $I(x, y, t)$. If the point moves by δx and δy in time δt, then according to the brightness constancy constraint:

$$\frac{dI}{dt} = 0. \tag{2.10}$$

This can also be stated as:

$$I(\mathbf{r} + \delta\mathbf{r}, t + \delta t) = I(\mathbf{r}, t). \tag{2.11}$$

where $\mathbf{r} = (x, y, 1)^T$ and $\mathbf{r} + \delta\mathbf{r} = (x + \delta x, y + \delta y, 1)^T$. However, the brightness constancy constraint is restrictive. A less restrictive brightness constraint was chosen to address the intensity changes in SAR images. In [Gennert and Negahdaripour (1987)], it is proposed that the brightness constancy constraint can be replaced with a more general constraint that allows a linear transformation between the pixel brightness values. This way, the brightness change can be non-zero, or:

$$\frac{dI}{dt} \neq 0.$$

The formulation that allows a linear transformation between the pixel brightness values is less restrictive, and can be written as:

$$I(\mathbf{r} + \delta\mathbf{r}, t + \delta t) = M(\mathbf{r}, t)I(\mathbf{r}, t) + C(\mathbf{r}, t). \tag{2.12}$$

After using the Taylor series, the revised constraint equation can be obtained:

$$I_t + I_{\mathbf{r}} \cdot \mathbf{r}_t - Im_t - c_t = 0, \tag{2.13}$$

where $m_t = \lim_{\delta t \to 0} \delta m / \delta t$ and $c_t = \lim_{\delta t \to 0} \delta c / \delta t$. The relaxed brightness constraint error is:

$$\epsilon_I = \iint (I_t + I_{\mathbf{r}} \cdot \mathbf{r}_t - Im_t - c_t)^2 \, dx \, dy. \tag{2.14}$$

Equation 2.14 can be combined with the other constraint errors to produce the final functional to be minimized:

$$\epsilon_{total} = \epsilon_I + \lambda_s \epsilon_s + \lambda_m \epsilon_m + \lambda_c \epsilon_c. \tag{2.15}$$

where λ_s, λ_m, and λ_c are error weighting coefficients. The remaining errors are given as:

$$\epsilon_s = \iint ||\nabla \mathbf{r}_t||_2^2 dx dy,$$

$$\epsilon_m = \iint ||\nabla m_t||_2^2 dx dy,$$

$$\epsilon_c = \iint ||\nabla c_t||_2^2 dx dy.$$

Substituting the approximated Laplacians into the Euler-Lagrange equations, a single matrix equation can be derived:

$$\mathbf{A}\mathbf{f} = \mathbf{g}(\bar{\mathbf{f}}), \tag{2.16}$$

where

$$\mathbf{A} = \begin{pmatrix} I_x^2 + \lambda_s & I_x I_y & -I_x I & -I_x \\ I_x I_y & I_y^2 + \lambda_s & -I_y I & -I_y \\ -I_x I & -I_y I & I^2 + \lambda_m & I \\ -I_x & -I_y & I & 1 + \lambda_c \end{pmatrix}, \mathbf{f} = \begin{pmatrix} u \\ v \\ m_t \\ c_t \end{pmatrix}, \quad \mathbf{g}(\bar{\mathbf{f}}) = \begin{pmatrix} \lambda_s \bar{u} - I_x I_t \\ \lambda_s \bar{v} - I_y I_t \\ \lambda_m \bar{m}_t + I_t I \\ \lambda_c \bar{c}_t + I_t \end{pmatrix}.$$
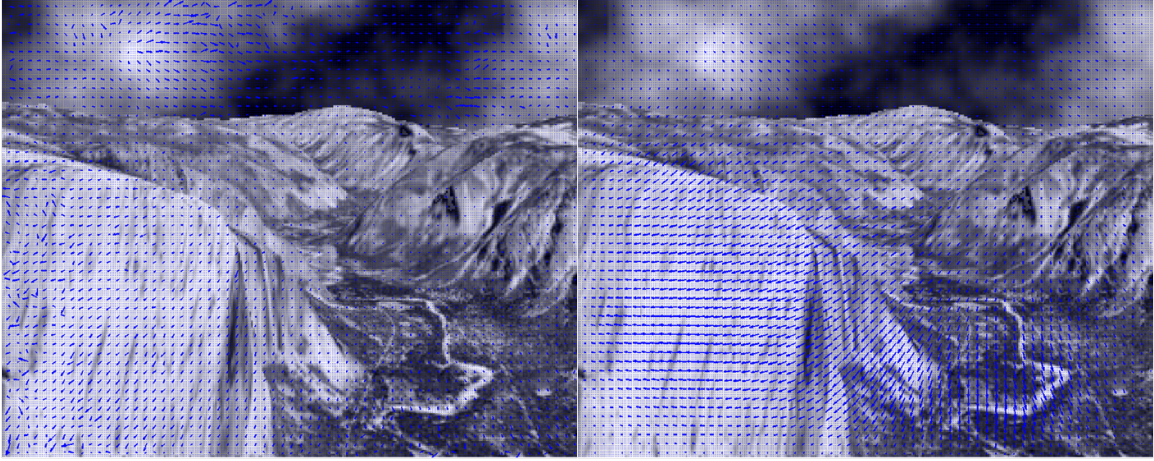
Figure 2. Original Horn-Schunck optical flow field (left) and an optical flow field produced with the Relaxed Brightness method (right). Note that the Relaxed Brightness method provides a smoother, more natural flow field than the Horn-Schunk method. Image Credit: Yosemite standard test sequence by Lynn Quam.

The rest of the steps leading to the solutions are given in section 4.2.1. Because of the flexibility in the brightness constraint, the resulting optical flow can include inexact matches in images. A comparison of the original optical flow method to the Relaxed Brightness method is provided on the Yosemite test sequence in Figure 2. The Yosemite standard test sequence is created by Lynn Quam [Barron *et al.* (1994b)].

2.3 Optical Flow with Divergence Constraint

When acquired images contain flow velocity information of fluids (e.g. velocimetry data), additional information can be used to add a new constraint in the optical flow algorithm. This section briefly introduces the formulation of using the velocity information and adding a new divergence constraint to the optical flow algorithm. This is the backbone of the interpolation framework that is presented in Chapter 3.

According to the continuity equation in fluid dynamics, the rate of mass entering a system is equal to the rate of the mass leaving the system [Pedlosky (1987)]. In the case of incompressible flow, the continuity equation takes the form:

$$\nabla \cdot \vec{u} = \frac{\partial V_x}{\partial x} + \frac{\partial V_y}{\partial y} + \frac{\partial V_z}{\partial z} = 0.$$

where $\vec{u}$ is the velocity vector field and V_x, V_y, and V_z are the velocity components. This means that the divergence of the velocity field is zero in the case of incompressible flow. Figure 3 shows the change in flow velocity of a voxel.
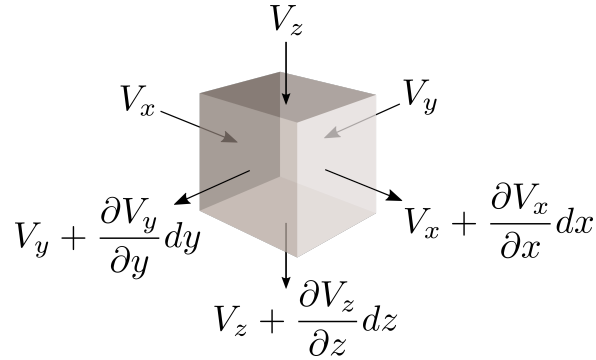
Figure 3. Velocity change in three components of the flow of a sample voxel.

If we know the divergence of a voxel is supposed to be zero, then we can for-

12

mulate a new constraint that uses this information. The new energy functional that needs to be minimized can be of the form:

$$\epsilon = \iint \underbrace{[H_x\alpha + H_y\beta + H_z]^2}_{\text{Brightness constraint}} + \gamma^2 \underbrace{[D_x\alpha + D_y\beta + D_z]^2}_{\text{Divergence constraint}} + \lambda^2 \underbrace{\left[\|\nabla\alpha\|^2 + \|\nabla\beta\|^2\right]}_{\text{Smoothness constraint}} dx\, dy$$

where α and β are the flow vectors. The formulation is expanded with new details in section 3.2.1.

Chapter 3

AN OPTICAL FLOW-BASED FRAMEWORK FOR
MINIMALLY-DIVERGENT VELOCIMETRY DATA INTERPOLATION

Three-dimensional (3D) biomedical image sets are often acquired with in-plane pixel spacings that are far less than the out-of-plane spacings between images. The resultant anisotropy, which can be detrimental in many applications, can be decreased using image interpolation. Optical flow and/or other registration-based interpolators can be useful in such interpolation roles since they can help form a correlation between the images. When acquired images are comprised of signals that describe the flow velocity of fluids, additional information is available to guide the interpolation process. In this section, the velocity information is used to form a new constraint in the optical flow algorithm. Then, a new interpolation framework that uses the new optical flow method is described. The proposed optical-flow based framework for image interpolation minimizes resultant divergence in the interpolated data.

3.1   Introduction

Image interpolation is a fundamental problem encountered in many fields [Oktay *et al.* (2016); Liu *et al.* (2018); Alves and Tavares (2015); Witwit *et al.* (2017); Roszkowiak *et al.* (2017); Titus and Geroge (2013); Teoh *et al.* (2008); Park *et al.* (2003); Lehman *et al.* (1999)]. There are countless scenarios wherein images are acquired at resolutions that are suboptimal for the needs of specific applications. For example, biomedical images spanning a 3D volume are often acquired with in-plane pixel spacings far less than

14

the out-of-plane spacings between images. This can be the case with clinical images (e.g., from computed tomography (CT) and/or magnetic resonance (MR) imaging) as well as in vitro images acquired with modalities such as particle image velocimetry (PIV) [Liberman *et al.* (2018); Karani *et al.* (2018); Chen *et al.* (2018); Pham *et al.* (2017); Lin *et al.* (2017); Hoon *et al.* (2016); Ozturk *et al.* (2003); Frakes *et al.* (2003)].

However, when acquired images are comprised of signals that describe the flow velocity of fluids, additional information is available to guide the interpolation process. Specifically, the flows of an incompressible fluid into and out of an interrogation volume must be equal according to conservation of mass [Pedlosky (1987)]. Quantifying the deviation from zero net flow that is entering (or alternatively leaving) an interrogation volume (i.e., divergence) thus provides a means to direct interpolation in such a way as to reconstruct more physically accurate data.

Optical flow and/or other registration-based interpolators have proven useful in interpolating velocimetry data in the past [Głomb *et al.* (2017); Baghaie and Yu (2014); This *et al.* (2017); Głomb and Świrniak (2018); Frakes *et al.* (2008); Penney *et al.* (2004); Casa and Krueger (2013); Brunet *et al.* (2013); Elkins and Alley (2007); Frakes *et al.* (2004); Melnikov and Shevtsova (2005); Heitz *et al.* (2010)]. Particle Image Velocimetry (PIV) is a technique that measures a velocity field in a fluid volume with the help of tracer particles in the fluid and specialized cameras [Raffel *et al.* (2013); Adrian and Westerweel (2011)]. The default technique to determine the velocity field from the raw PIV data is a correlation analysis between two frames that were acquired by the cameras [Scarano (2002)]. This technique can be extended to 3D as well. Optical flow-based approaches have been widely used in computer vision [Fortun *et al.* (2015b); Sun *et al.* (2014); Dosovitskiy *et al.* (2015); Aubert and Kornprobst (2006); Bruhn *et al.* (2006)], and they have been appealing to researchers because of the flex-

ibility of variational approaches. Regularizers can be used for different constraints in the energy functional to be minimized. In the conventional optical flow method there are two constraints, brightness and smoothness [Horn and Schunck (1980)]. Optical flow-based methods have been promising in the area of fluid flow estimation in PIV [Alvarez *et al.* (2007, 2009); Ruhnau *et al.* (2007); Ruhnau and Schnörr (2007); Herlin *et al.* (2012); Zhong *et al.* (2017)]. For example, in Alvarez *et al.* (2009), incompressibility of the flow is added as a constraint in the optical flow minimization problem. In Ruhnau *et al.* (2007), the vorticity transport equation, which describes the evolution of the fluid's vorticity over time, is used in physically consistent spatio-temporal regularization to estimate fluid motion.

Divergence and curl (vorticity) have been used in estimating optical flow previously Suter (1994); Gupta and Prince (1996b,a); Corpetti *et al.* (2006). In Suter (1994), the smoothness constraint is decomposed into two parts, divergence and vorticity, in this way, the smoothness properties of the optical flow can be tuned. In Song and Leahy (1991), both incompressibility and divergence-free constraints are used in the ill-posed minimization problem to calculate a 3D velocity field from 3D Cine CT images. In Gupta and Prince (1996a), a second order div-curl spline smoothness condition is employed in order to compute a 3D motion field. In Corpetti *et al.* (2006), a data term based on the continuity equation of fluid mechanics [Pedlosky (1987)] and a second order div-curl regularizer are employed to calculate fluid flow.

In this chapter, an optical-flow based framework for image interpolation that also minimizes resultant divergence in the interpolated data is presented. That is, the divergence constraint attempts to minimize divergence in interpolated velocimetry data, not the divergence of the optical flow field. To our knowledge, using divergence in this way as a constraint in an optical-flow framework for image interpolation has not

16

been investigated prior to the preliminary work presented in Kanberoglu *et al.* (2017). The method is applied to PIV, computational fluid dynamics (CFD), and analytical data and results indicate that the tradeoff between minimizing errors in velocity magnitude values and errors in divergence can be managed such that both are decreased below levels observed for standard truncated sinc function-based interpolators, as well as pure optical flow-based interpolators. The proposed method thus has potential to provide an improved basis for interpolating velocimetry data in applications where isotropic flow velocity volumes are desirable, but out-of-plane data (i.e., data in different images spanning a 3D volume) can not be resolved as highly as in-plane data.

The remainder of this chapter is structured as follows. In section 3.2.1, an optical flow-based framework for interpolating minimally divergent velocimetry data is described. The proposed method is built on the principles that are described in the preceding Chapter 2. The new method uses flow velocity data to guide the interpolation toward lesser divergence in the interpolated data. In section 3.3, performance of the proposed technique is presented with experiments and simulations on real and analytical data. The results and performance of the proposed method are discussed and concluded in section 3.4.

3.2   Optical Flow with Divergence Constraint

3.2.1   Methodology

In section 2.1, the methodology for the original optical flow technique is provided and two kinds of constraints are introduced in order to estimate the optical flow: the

smoothness constraint and the *brightness constancy constraint*. This section introduces a new constraint to estimate the optical flow.

3.2.1.1   Continuity Equation

According to the continuity equation in fluid dynamics, the rate of mass entering a system is equal to the rate of the mass leaving the system [Pedlosky (1987)]. The differential form of the equation is:

$$\frac{\partial \rho}{\partial t} + \nabla \cdot (\rho \vec{u}) = 0, \tag{3.1}$$

where ρ is the fluid density, t is time and $\vec{u}$ is the velocity vector field. In the case of incompressible flow, ρ becomes constant and the continuity equation takes the form:

$$\nabla \cdot \vec{u} = \frac{\partial V_x}{\partial x} + \frac{\partial V_y}{\partial y} + \frac{\partial V_z}{\partial z} = 0. \tag{3.2}$$

This means that the divergence of the velocity field is zero in the case of incompressible flow. In the previous section, Figure 3 shows the change in flow velocity of a voxel.

3.2.1.2   Symmetric Setup

For the new method, a symmetric interpolation setup is proposed as shown in Figure 4. In the figure, upper and lower slices are from the dataset and the interpolated slice is in the middle.
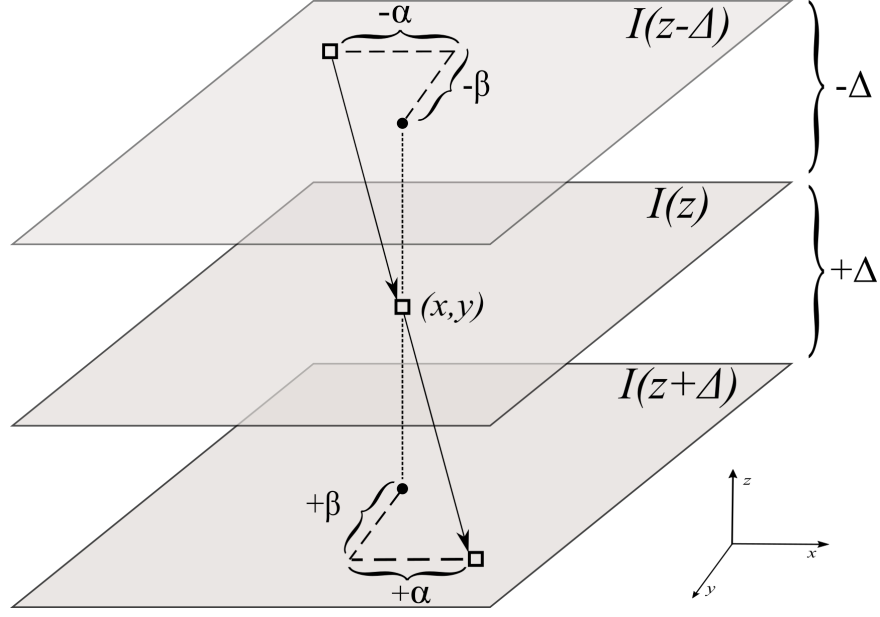
Figure 4. Illustration of the symmetric interpolation setup.

$$I(x + \alpha, y + \beta, z + \Delta) = I(x - \alpha, y - \beta, z - \Delta). \tag{3.3}$$

In this section, $I(x, y, t)$ denotes the velocity magnitude image and $\vec{V}$ denotes the velocity vector components (i.e., V_x, V_y, V_z). If one approximates the expressions with Taylor expansion around the points (x, y), we get:

$$I(x + \alpha, y + \beta, z + \Delta) = I(x, y, z + \Delta) + \frac{\partial I(x, y, z + \Delta)}{\partial x}\alpha + \frac{\partial I(x, y, z + \Delta)}{\partial y}\beta + ... ,$$

$$\tag{3.4a}$$

$$I(x - \alpha, y - \beta, z - \Delta) = I(x, y, z - \Delta) - \frac{\partial I(x, y, z - \Delta)}{\partial x}\alpha - \frac{\partial I(x, y, z - \Delta)}{\partial y}\beta + ...$$

$$\tag{3.4b}$$

After substituting Eqs. 3.4a and 3.4b into Eq. 3.3, terms can be arranged to obtain the new brightness constraint:

$$
\begin{aligned}
[I(x, y, z + \Delta) &- I(x, y, z - \Delta)] \\
&+ \alpha \left[\frac{\partial I(x, y, z + \Delta)}{\partial x} + \frac{\partial I(x, y, z - \Delta)}{\partial x} \right] \\
&+ \beta \left[\frac{\partial I(x, y, z + \Delta)}{\partial y} + \frac{\partial I(x, y, z - \Delta)}{\partial y} \right] = 0.
\end{aligned}
\tag{3.5}
$$

In the next step, the aim is to minimize the divergence of the interpolated slice. Ideally, the divergence equation of the interpolated slice should be used:

$$
\nabla \cdot \overrightarrow{\mathbf{V}}(z) = \frac{\partial V_x(x, y, z)}{\partial x} + \frac{\partial V_y(x, y, z)}{\partial y} + \frac{\partial V_z(x, y, z)}{\partial z} = 0.
\tag{3.6}
$$

Since this information is unavailable, to generate the middle slice with as little divergence as possible, we can use the fact that:

$$
\nabla \cdot \overrightarrow{\mathbf{V}}(z) = \nabla \cdot \overrightarrow{\mathbf{V}}(z + \Delta) = \nabla \cdot \overrightarrow{\mathbf{V}}(z - \Delta) = 0.
\tag{3.7}
$$

which leads to the following constraint by using the divergence expressions of the two outer slices, $I(z - \Delta)$ and $I(z + \Delta)$:

$$
\begin{aligned}
\frac{\partial V_x(x + \alpha, y + \beta, z + \Delta)}{\partial x} &+ \frac{\partial V_y(x + \alpha, y + \beta, z + \Delta)}{\partial y} \\
+ \frac{\partial V_z(x + \alpha, y + \beta, z + \Delta)}{\partial z} &+ \frac{\partial V_x(x - \alpha, y - \beta, z - \Delta)}{\partial x} \\
+ \frac{\partial V_y(x - \alpha, y - \beta, z - \Delta)}{\partial y} &+ \frac{\partial V_z(x - \alpha, y - \beta, z - \Delta)}{\partial z} = 0.
\end{aligned}
\tag{3.8}
$$

Using Taylor expansion on Eq. 3.8 yields:

$$
\begin{aligned}
&\left[\frac{\partial V_x(z+\Delta)}{\partial x} + \frac{\partial V_x(z-\Delta)}{\partial x} + \frac{\partial V_y(z+\Delta)}{\partial y} \right] \\
&+ \left[\frac{\partial V_y(z-\Delta)}{\partial y} + \frac{\partial V_z(z+\Delta)}{\partial z} + \frac{\partial V_z(z-\Delta)}{\partial z} \right] \\
&+ \alpha \left[\frac{\partial^2 V_x(z+\Delta)}{\partial x^2} - \frac{\partial^2 V_x(z-\Delta)}{\partial x^2} + \frac{\partial^2 V_y(z+\Delta)}{\partial x \partial y} \right] \\
&- \alpha \left[\frac{\partial^2 V_y(z-\Delta)}{\partial x \partial y} + \frac{\partial^2 V_z(z+\Delta)}{\partial x \partial z} - \frac{\partial^2 V_z(z-\Delta)}{\partial x \partial z} \right] \\
&+ \beta \left[\frac{\partial^2 V_x(z+\Delta)}{\partial y \partial x} - \frac{\partial^2 V_x(z-\Delta)}{\partial y \partial x} + \frac{\partial^2 V_y(z+\Delta)}{\partial y^2} \right] \\
&- \beta \left[\frac{\partial^2 V_y(z-\Delta)}{\partial y^2} + \frac{\partial^2 V_z(z+\Delta)}{\partial y \partial z} - \frac{\partial^2 V_z(z-\Delta)}{\partial y \partial z} \right] = 0.
\end{aligned}
\tag{3.9}
$$

In Eq. 3.9, we need the derivatives of $V_z(z+\Delta)$ and $V_z(z-\Delta)$ in the z-direction. Calculating these derivatives in the z-direction would require additional outer slices. To simplify this requirement, we can expand $V_z(x+\alpha, y+\beta, z+\Delta)$ and $V_z(x-\alpha, y-\beta, z-\Delta)$ around the points (x, y, z) and obtain the following,

$$
\begin{aligned}
\frac{\partial V_z(x+\alpha, y+\beta, z+\Delta)}{\partial z} &= \frac{\partial V_z(x,y,z)}{\partial z} + \alpha \frac{\partial^2 V_z(x,y,z)}{\partial x \partial z} \\
&+ \beta \frac{\partial^2 V_z(x,y,z)}{\partial y \partial z} + \Delta \frac{\partial^2 V_z(x,y,z)}{\partial z^2} + \dots
\end{aligned}
\tag{3.10a}
$$

$$
\begin{aligned}
\frac{\partial V_z(x-\alpha, y-\beta, z-\Delta)}{\partial z} &= \frac{\partial V_z(x,y,z)}{\partial z} - \alpha \frac{\partial^2 V_z(x,y,z)}{\partial x \partial z} \\
&- \beta \frac{\partial^2 V_z(x,y,z)}{\partial y \partial z} - \Delta \frac{\partial^2 V_z(x,y,z)}{\partial z^2} + \dots
\end{aligned}
\tag{3.10b}
$$

Using Eqs. 3.10a and 3.10b in Eq. 3.8, we obtain the new divergence constraint that doesn't require additional slices for the z-direction derivative,

$$
\begin{aligned}
&\left[\frac{\partial V_x(z+\Delta)}{\partial x} + \frac{\partial V_x(z-\Delta)}{\partial x} + \frac{\partial V_y(z+\Delta)}{\partial y} + \frac{\partial V_y(z-\Delta)}{\partial y} + 2\frac{\partial V_z}{\partial z} \right] \\
&+ \alpha \left[\frac{\partial^2 V_x(z+\Delta)}{\partial x^2} - \frac{\partial^2 V_x(z-\Delta)}{\partial x^2} + \frac{\partial^2 V_y(z+\Delta)}{\partial x \partial y} - \frac{\partial^2 V_y(z-\Delta)}{\partial x \partial y} \right] \\
&+ \beta \left[\frac{\partial^2 V_x(z+\Delta)}{\partial y \partial x} - \frac{\partial^2 V_x(z-\Delta)}{\partial y \partial x} + \frac{\partial^2 V_y(z+\Delta)}{\partial y^2} - \frac{\partial^2 V_y(z-\Delta)}{\partial y^2} \right] = 0.
\end{aligned}
\tag{3.11}
$$

21

Combining Eqs. 3.5, 3.11 and the optical flow smoothness constraint, we obtain the new energy functional that needs to be minimized,

$$\epsilon = \iint \left[H_x\alpha + H_y\beta + H_z \right]^2 + \gamma^2 \left[D_x\alpha + D_y\beta + D_z \right]^2 + \lambda^2 \left[\|\nabla\alpha\|^2 + \|\nabla\beta\|^2 \right] dx \, dy$$

(3.12)

where

$$H_x = \left[\frac{\partial I(x,y,z+\Delta)}{\partial x} + \frac{\partial I(x,y,z-\Delta)}{\partial x} \right]$$

$$H_y = \left[\frac{\partial I(x,y,z+\Delta)}{\partial y} + \frac{\partial I(x,y,z-\Delta)}{\partial y} \right]$$

$$H_z = \left[I(x,y,z+\Delta) - I(x,y,z-\Delta) \right]$$

$$D_x = \left[\frac{\partial^2 V_x(z+\Delta)}{\partial x^2} - \frac{\partial^2 V_x(z-\Delta)}{\partial x^2} + \frac{\partial^2 V_y(z+\Delta)}{\partial x\partial y} - \frac{\partial^2 V_y(z-\Delta)}{\partial x\partial y} \right]$$

$$D_y = \left[\frac{\partial^2 V_x(z+\Delta)}{\partial y\partial x} - \frac{\partial^2 V_x(z-\Delta)}{\partial y\partial x} + \frac{\partial^2 V_y(z+\Delta)}{\partial y^2} - \frac{\partial^2 V_y(z-\Delta)}{\partial y^2} \right]$$

$$D_z = \left[\frac{\partial V_x(z+\Delta)}{\partial x} + \frac{\partial V_x(z-\Delta)}{\partial x} + \frac{\partial V_y(z+\Delta)}{\partial y} + \frac{\partial V_y(z-\Delta)}{\partial y} + 2\frac{\partial V_z}{\partial z} \right]$$

Using variational calculus, the Euler-Lagrange equations can be determined for this problem. They need to be solved for each pixel in the image. The iterative equations that minimize the solutions are given by,

$$\alpha^{n+1} = \bar{\alpha}^n - \frac{A_1\bar{\alpha}^n + B_1\bar{\beta}^n + \gamma^2 C_1 + \lambda^2 C_2}{\gamma^2 D_1 + \lambda^2 D_2},$$

(3.13a)

$$\beta^{n+1} = \bar{\beta}^n - \frac{A_2\bar{\alpha}^n + B_2\bar{\beta}^n + \gamma^2 C_3 + \lambda^2 C_4}{\gamma^2 D_3 + \lambda^2 D_4},$$

(3.13b)

where n denotes the iteration number and $\bar{\alpha}^n$ and $\bar{\beta}^n$ denote neighborhood averages of α^n and β^n. The coefficient expressions in Eqs. 3.13a and 3.13b are given

as

$$A_1 = \gamma^2 \left(H_x D_y - H_y D_x \right)^2 + \lambda^2 \left(H_x^2 + \gamma^2 D_x^2 \right)$$

$$B_1 = \lambda^2 \left(H_x H_y + \gamma^2 D_x D_y \right)$$

$$C_1 = H_x H_z D_y^2 + H_y^2 D_x D_z - H_y H_z D_x D_y - H_x H_y D_y D_z$$

$$C_2 = H_x H_z + \gamma^2 D_x D_z$$

$$D_1 = \left(H_x D_y - H_y D_x \right)^2$$

$$D_2 = \left(H_x^2 + H_y^2 + \lambda^2 + \gamma^2 D_x^2 + \gamma^2 D_y^2 \right)$$

$$A_2 = B_1$$

$$B_2 = \gamma^2 \left(H_x D_y - H_y D_x \right)^2 + \lambda^2 \left(H_y^2 + \gamma^2 D_y^2 \right)$$

$$C_3 = H_y H_z D_x^2 + H_x^2 D_y D_z - H_x H_z D_x D_y - H_x H_y D_x D_z$$

$$C_4 = H_y H_z + \gamma^2 D_y D_z$$

$$D_3 = D_1$$

$$D_4 = D_2$$

More detailed steps of the derivation can be found in Appendix A.
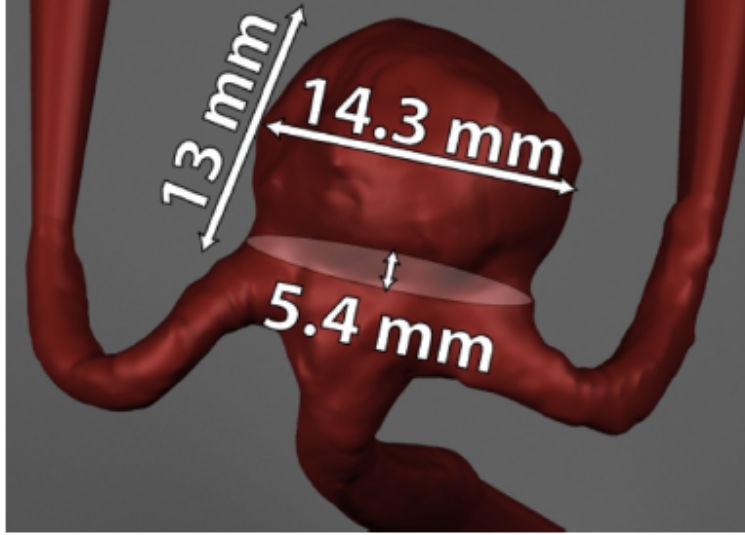
Figure 5. Dimensions of the aneurysm

3.2.2 PIV Setup

The testing datasets were acquired using particle image velocimetry, an optical experimental flow measurement technique. PIV data acquisition and processing generally consists of the following steps: (1) computational modeling, (2) physical model construction, (3) particle image acquisition, (4) PIV processing, and (5) data analysis. The testing datasets were acquired for an in-vitro model of a cerebral aneurysm. Patient-specific computed tomography (CT) images were first segmented and reconstructed to obtain the computational cerebral aneurysm model as shown in Figure 5. The computational model was then translated into an optically clear, rigid urethane model using a lost-core manufacturing methodology. The physical model was connected to a flow loop consisting of a blood analog solution seeded with 8 μm fluorescent microspheres. Fluid flow through the physical model was controlled at specific flow rates (3, 4 and 5 mL/s). PIV was performed using a FlowMaster 3D

Stereo PIV system (LaVision, Ypsilanti, MI), where the fluorescent particles were illuminated with a 532 nm dual-pulsed Nd:YAG laser at a controlled rate, while two CCD cameras captured the images across seven parallel planes (or slices) within the aneurysmal volume. A distance of 1 mm separated the planes. Two hundred image pairs, at each flow rate and slice, were acquired at 5 Hz. The image pairs were processed using a recursive cross-correlation algorithm using Davis software (LaVision, Ypsilanti, MI) to calculate the velocity vectors within region of interest (i.e., the aneurysm). Initial and final interrogation window sizes of 32 by 32 pixels and 16 by 16 pixels, respectively, were used. Detailed explanation of the experimental process can be found in Roszelle *et al.* (2014). A sample experimental model is shown in Figure 6.

The proposed algorithm was developed in MATLAB (Mathworks, Inc). Since the proposed algorithm has two separate terms for divergence and smoothness, different combinations of coefficients can be used for the terms. However, in order to get a clear idea about the performance of the method only one set of parameters were used in the simulations. The divergence term's coefficient γ was set to 150. From previous tests, it was seen that the proposed method performed better when a relatively large γ was used while keeping the smoothness coefficient λ small. The smoothness coefficient λ was set to 1. The same smoothness coefficient was also used for the Horn-Schunck based method. The iterations for both methods were set to 2000. Each PIV dataset used in testing had 7 slices. The slices were originally 154x121. They were cropped and zero-padded to reach 128x128. The size of the region where MSE and divergence were calculated is 110x110. Even though there are 7 slices in each dataset, only 3 slices were reconstructed from the datasets. These are slices 3, 4 and 5. Two different spacing steps were used between the slices. The
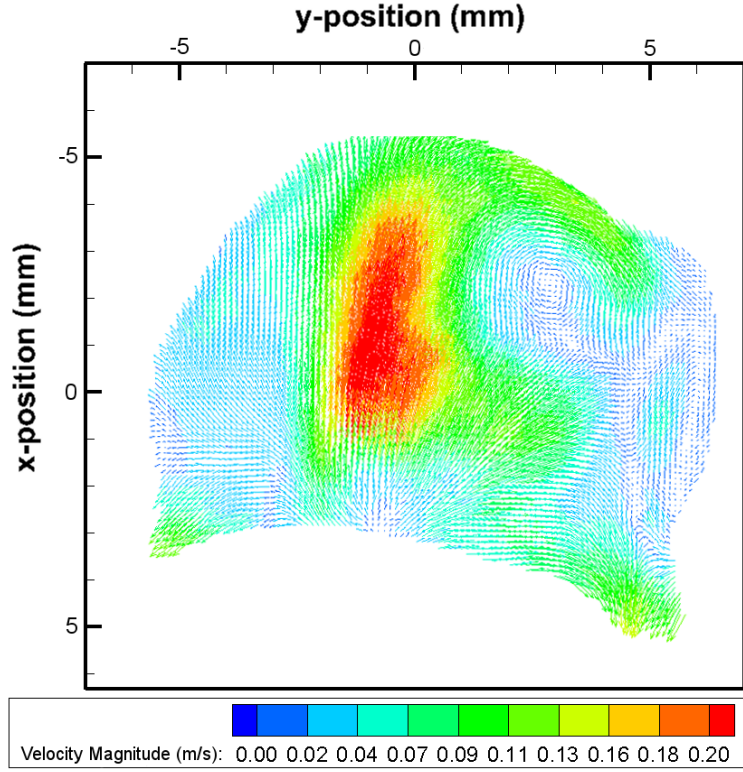
Figure 6. Example flow slice from the PIV experiments.

first one is $\Delta z=2$ where the neighboring slices z-1 and z+1 were used to reconstruct the middle slice. The second one is $\Delta z=4$ where slices z-2 and z+2 were used for the interpolation, e.g., slices 1 and 5 were used to reconstruct slice 3. The method was tested against linear interpolation and an implementation of Horn-Schunck optical flow based interpolation.

3.2.3 Analytical Datasets

The method was tested with a 3D divergence-free analytical dataset and a CFD data set with turbulent flow. The analytical dataset is given below.

$$V_x = 0.3y^2 + 0.15x^2 \tag{3.14a}$$

$$V_y = 0.3\left(1 - x^2\right)(y - 1) - 0.3yx \tag{3.14b}$$

$$V_z = -0.3\left(1 - x^2\right)z \tag{3.14c}$$

Out-of-plane distance was kept much higher than the in-plane resolution. In order to assess the robustness of the proposed method, each velocity field was perturbed by Gaussian noise. The noise had zero mean and standard deviation of 10% of the maximum velocity in each velocity field.

3.2.4 Computational Fluid Dynamics (CFD) Simulations

The original computational aneurysm model was imported into ANSYS ICEM (ANSYS, Canonsburg, PA), where the inlet and outlets of the aneurysm model were extruded. After meshing was performed to discretize blood volumes into tetrahedrons, the final mesh was imported into ANSYS Fluent where the blood volume was modeled as an incompressible fluid with the same density and viscosity as the blood analog solution used in experiments. The vessel wall was assumed to be rigid, and a no-slip boundary condition was applied at the walls. A steady flat 4ml/s flow profile was applied at the inlet of the model, and zero pressure boundary conditions were imposed at the outlets. The overall CFD approach has been described previously in [Roszelle *et al.* (2014); Babiker *et al.* (2011)].

3.3   Results

Figure 7 shows divergence and MSE comparison graphs when $\Delta z=2$. The proposed method consistently achieves lower divergence values than the Horn-Schunck-based interpolation whereas the MSE values vary between better and worse values. On average, divergence values were 11% lower than the Horn-Schunck-based interpolation. In some cases, the proposed method achieves up to 20% lower divergence values. Figure 8 shows divergence and MSE comparison graphs when $\Delta z=4$. In this case, the proposed method consistently achieves lower divergence and MSE values than the other tested methods. Figure 9 shows original, noisy, and interpolated slices from the analytical dataset for comparison. In the figure, only V_x and V_y components were plotted to show the effect of the divergence term. In Figure 10, it can be seen that the proposed algorithm reduces divergence while the MSE is increased in the CFD dataset.

The graphs in Figure 11 show the behavior of the proposed method as the divergence coefficient γ increases linearly. In this simulation, the smoothness coefficient λ was kept constant ($\lambda=1$). The graphs are taken from the PIV dataset. It should be noted that the divergence graph profiles were consistent across different images and datasets. The MSE graph profiles may differ slightly from the divergence graph profiles across different datasets, but MSE always increased with increasing γ. Figure 12 shows the behavior of the proposed method as γ and λ increase linearly. The coefficient values tested were from 0 to 2000. The profiles shown in the figure show that there needs to be a balance between the divergence and smoothing terms. The graphs in the figure are consistent with profiles of other published ℓ_2-based regularization methods [Shaw and Yalavarthy (2012); Habermehl *et al.* (2014)].
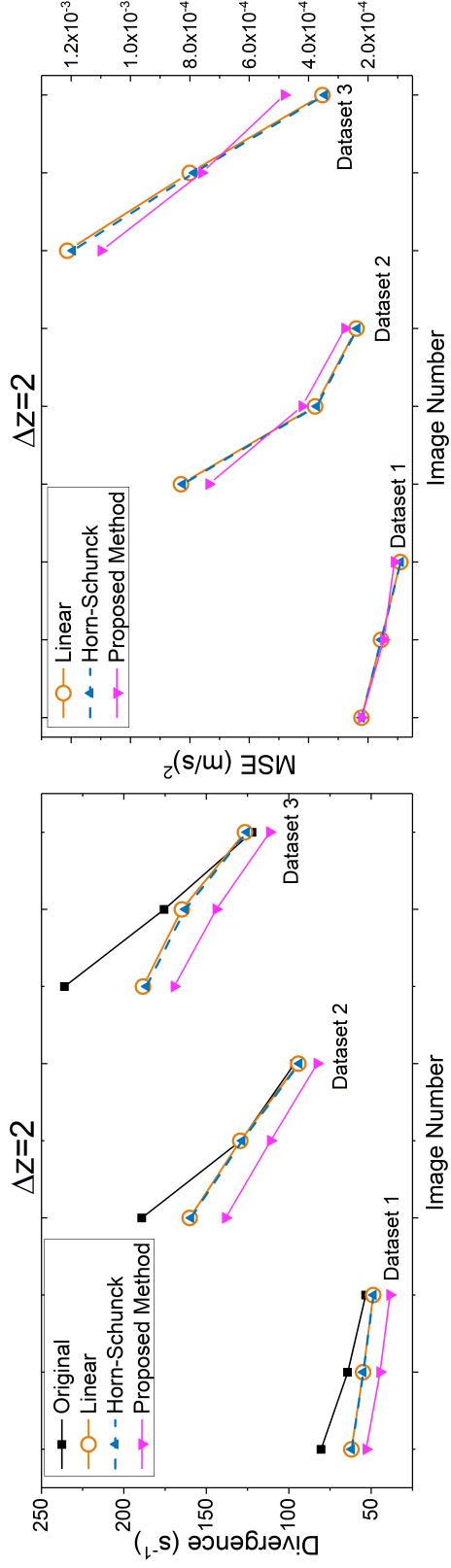
Figure 7. Divergence and MSE comparisons when slice distance is 2mm.
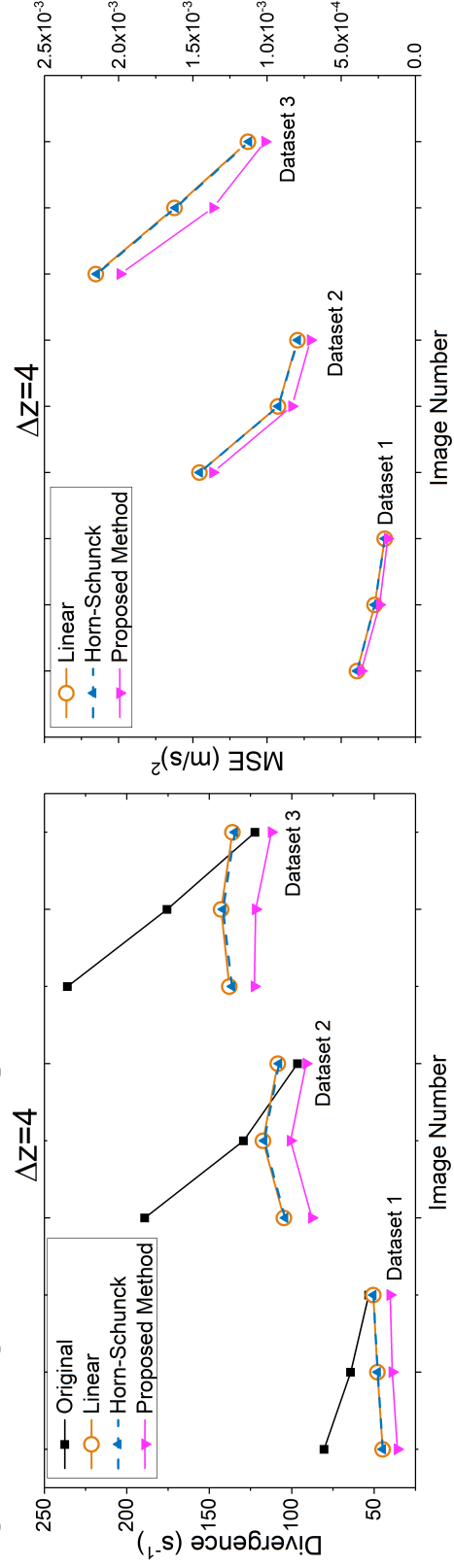
Figure 8. Divergence and MSE comparisons when slice distance is 4mm.

29
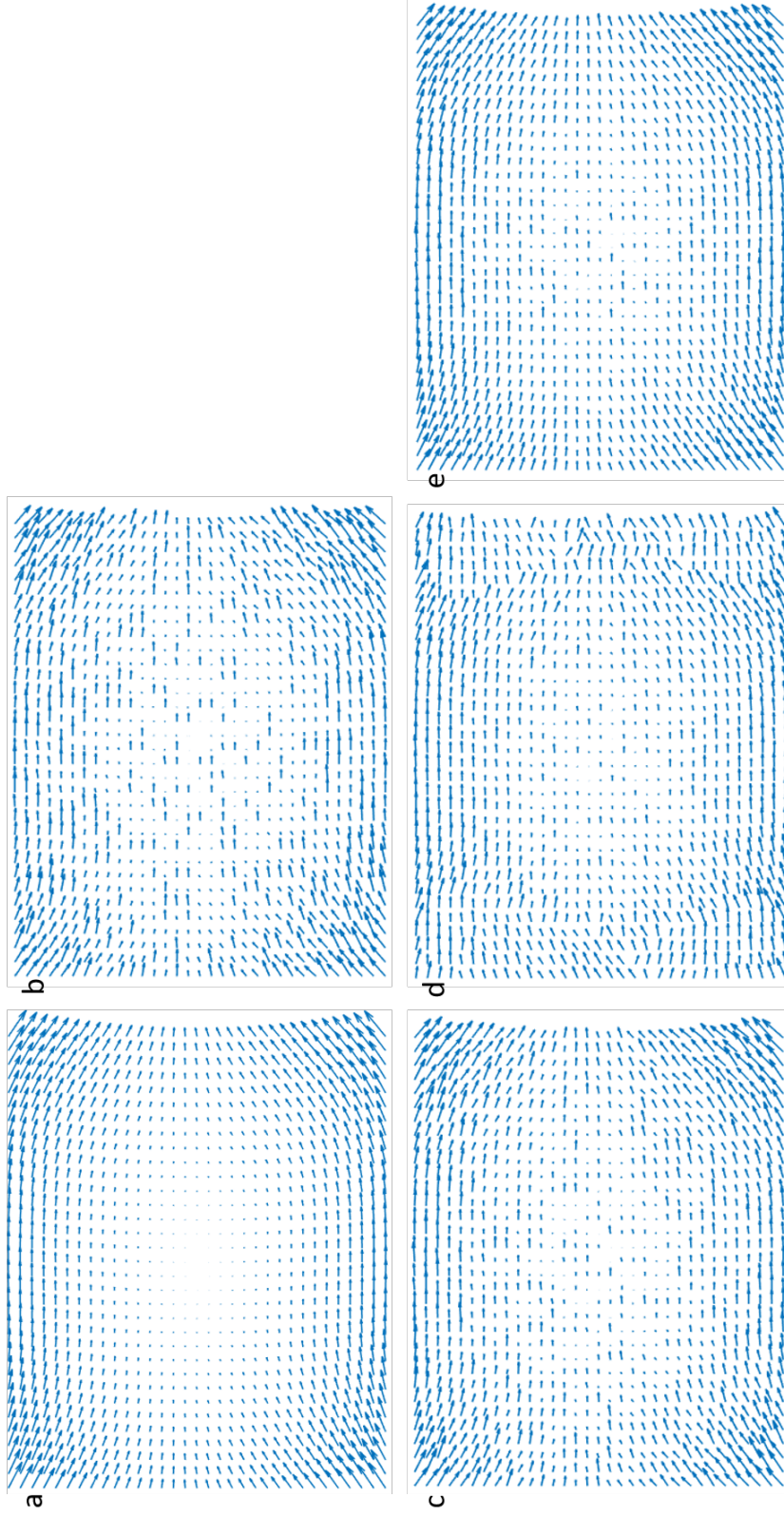
Figure 9. Plotted V_x and V_y components of the 3D analytical divergence-free vector field. a) Original, b) Gaussian noise added, c) Linear interpolation, d) Horn-Schunck based interpolation, e) Proposed method. Note that the proposed method is able to achieve a smoother velocity field in the corners of the interpolated data.
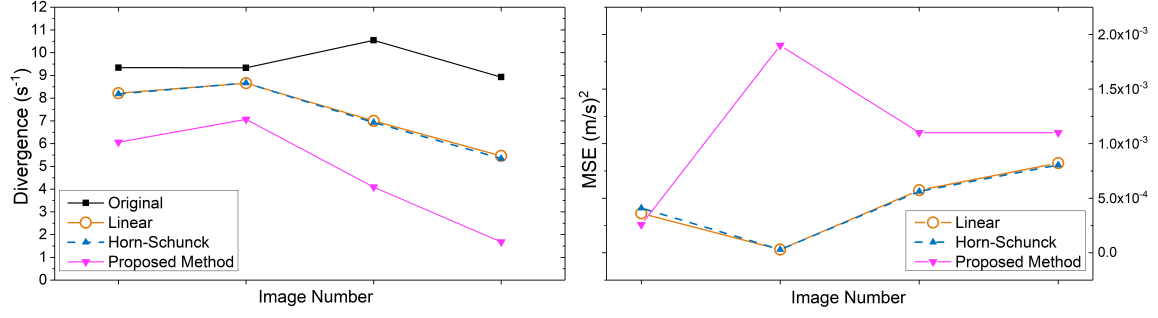
Figure 10. Divergence and MSE comparisons for the CFD dataset.

It should be noted that the computational cost of obtaining flow vectors with the proposed method is similar to that of the Horn-Schunck approach. Even though the iterative solutions of the proposed method employ several terms, these need to be computed only once and can be reduced to a simpler form that is similar to the Horn-Schunck solutions.
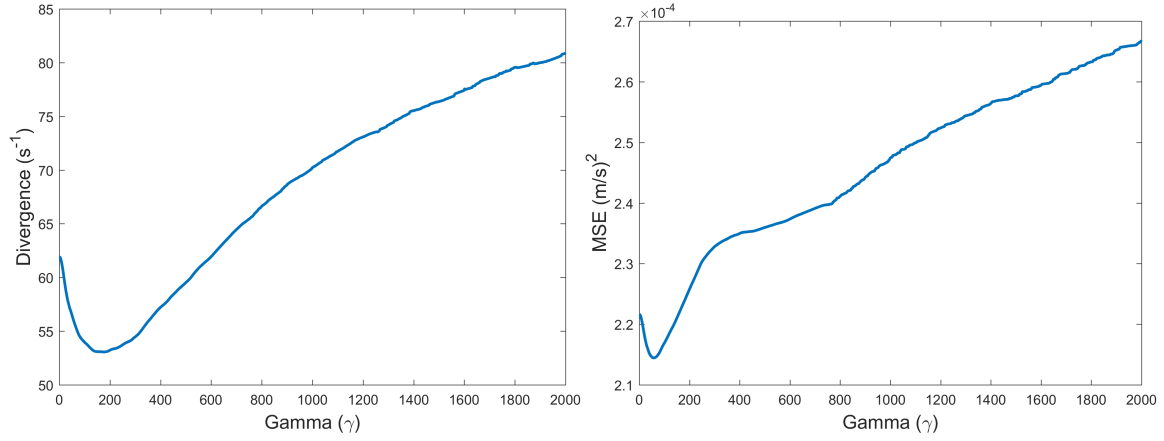
Figure 11. Divergence and MSE profiles of the proposed method as γ is increased linearly while $\lambda = 1$.

31
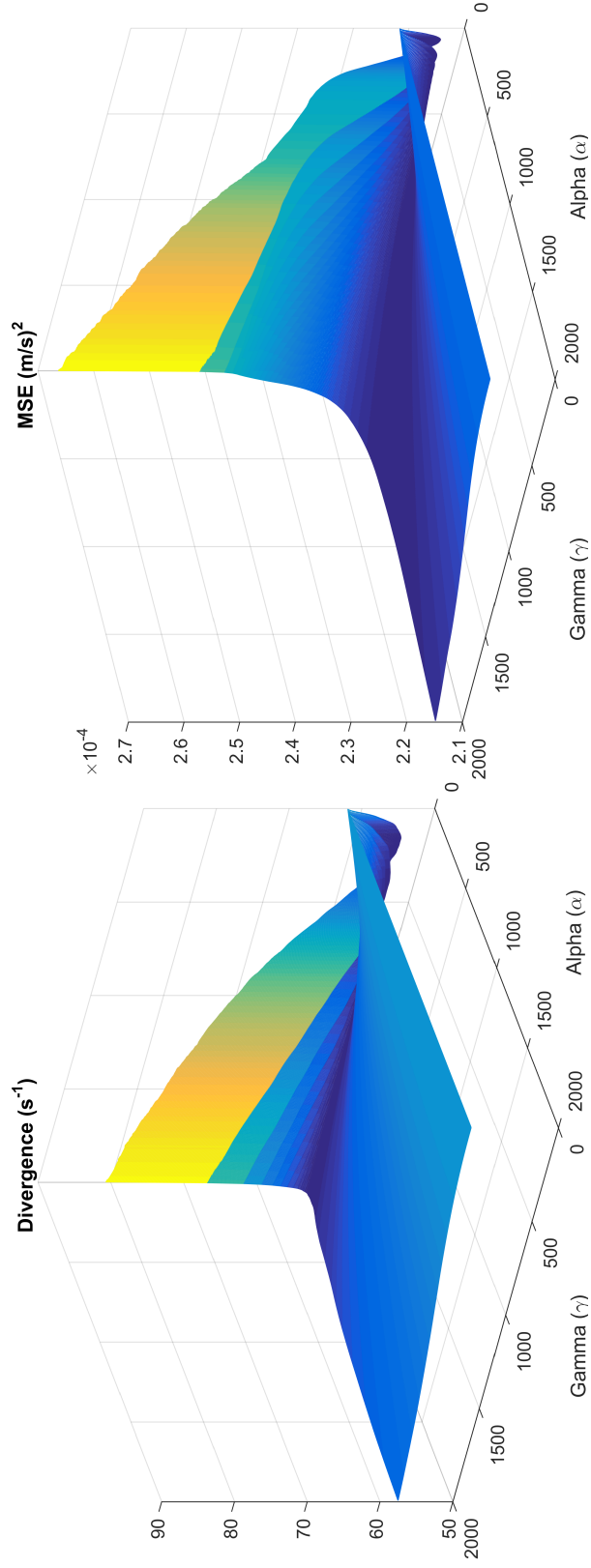
Figure 12. Divergence and MSE profiles of the proposed method as γ and λ are increased linearly.

32

3.4 Discussion & Conclusions

A new optical flow-based framework for image interpolation that also reduces divergence is proposed. The new method uses flow velocity data to guide the interpolation toward lesser divergence in the interpolated data. In addition to the symmetric interpolation setup, the method introduces a new divergence term into the canonical optical flow method. The method is applied to PIV, analytical, and CFD data. The method was tested against linear interpolation and the Horn-Schunck optical flow method since it uses a similar formulation as the Horn-Schunck method. The proposed method applies a symmetric interpolation setup and considers a new divergence term in addition to the brightness and smoothness terms in the energy functional.

In order to test the effects of the divergence term, both the Horn-Schunck and proposed methods were subject to the same smoothness coefficient. When tested on the noisy analytical data, the proposed method achieved a smoother and less noisy interpolated velocity field.

The proposed method was also applied to the PIV data with different values of smoothness and divergence term coefficients, α and γ, respectively. Results indicate that the tradeoff between minimizing errors in velocity magnitude values and errors in divergence can be managed such that both are decreased below levels observed for standard truncated sinc function-based interpolators as well as pure optical flow-based interpolators. The divergence term coefficient, γ, needs to be large enough to reduce divergence in the interpolated data but not so large as to dominate the energy functional and introduce errors into the final interpolated velocity field.

The proposed method has potential to improve the interpolation of velocime-

try data when it's difficult achieve an out-of-plane resolution close to the in-plane resolution. The results also indicate that the effect of the new divergence term in the optical flow functional can be appreciated better as the distance between the interpolated slice and the neighboring slices increases. It was noted that the proposed method outperforms the tested methods in both divergence and MSE values when the slice distance was increased. When the slice distance is small, the proposed method achieves lower divergence than the other methods while achieving similar MSE values.

Chapter 4

EXTRACTION OF ADVANCED GEOSPATIAL INTELLIGENCE (AGI) FROM COMMERCIAL SYNTHETIC APERTURE RADAR IMAGERY

One of the important goals of synthetic aperture radar (SAR) imagery is the capability of detecting changes between imaging passes. In two-color multiview (2CMV) products, the changes are colorized and overlaid on one of the images so that new features are represented in cyan, and features that have disappeared are represented in red. In order to create the change maps, images are cross-correlated pixel wise to detect the changes. The extraction of temporal changes and objects from advanced geospatial intelligence (AGI) products based on SAR imagery is complicated by a number of factors. Accurate detection of temporal changes and objects represented in 2CMV AGI products can be challenging because of speckle noise susceptibility and false positives that result from small orientation differences between objects imaged at different times. 2CMV images were chosen as the focus of work documented in this paper because of the lack of published methods to generate efficient 2CMV images from SAR imagery.

4.1   Introduction

One important use of SAR imagery is in detecting changes between datasets from different imaging passes. Target and coherent change detection in SAR images have been extensively researched [El-Darymli *et al.* (2013, 2016); Ashok and Patil (2014); Ren *et al.* (2014)]. In 2CMV AGI products, the changes are colorized and overlaid on

an initial image such that new features are represented in cyan, and features that have disappeared are represented in red. In order to create the change maps, images are cross-correlated pixel-by-pixel to detect the changes. 2CMV products show changes at the pixel level and are dominated with red and cyan colors. Figure 13 shows a portion of a sample 2CMV image. It can be seen that most of the pixels in the 2CMV image are colored either red or cyan even if there is no change in the area.

Useful interpretation of temporal changes represented in 2CMV AGI products can be challenging because of speckle noise susceptibility and false positives that result from small orientation differences between objects imaged at different times. When every small intensity change creates a colored pixel, it becomes more difficult for operators and/or algorithms to detect meaningful changes and identify corresponding objects of interest.

Before false positive and object detections, smoothing filters are used to attenuate the effects of speckle noise. Then, the number of false positive detections are reduced by applying: 1) object intensity and area thresholding and 2) optical flow algorithms that track the motion of objects across time in small regions of interest. Optical flow fields can be used to distinguish between objects that have actually moved between frames and those that are in the same location but are slightly misregistered. Both cases of apparent motion can result in 2CMV detection, but they obviously differ greatly in terms of significance. Investigation of the state-of-the-art in SAR image processing indicates that differentiating between these two general cases is a problem that has not been well addressed. The algorithms that were proposed for mitigating speckle noise effects and distinguishing between actual motion and misregistration can lead to more accurate and meaningful change detection. A lack of published
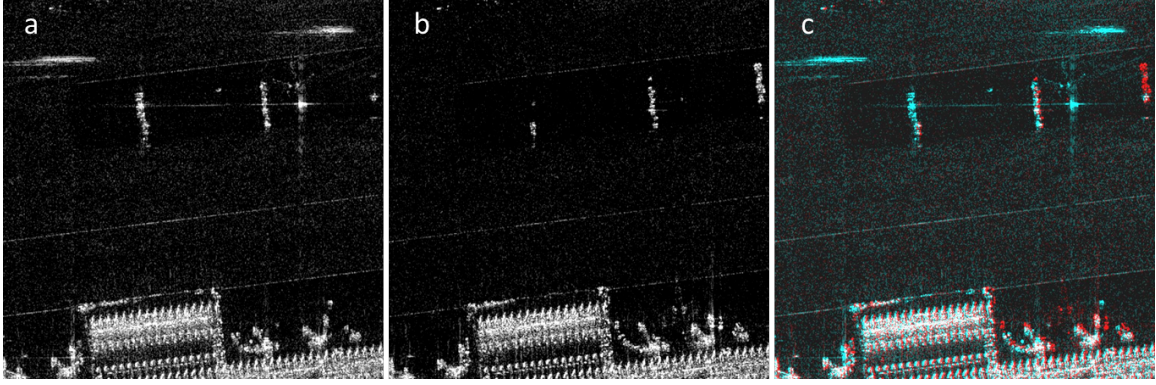
Figure 13. a) Reference image, b) Mission image, c) Two-color multiview (2CMV) image. In all the images, there is an airplane visibly parked next to a building near the bottom center.

methods for efficient generation of 2CMV products from SAR images serves as another motivating factor for this work.

The remainder of this chapter is organized in four sections. Following the introduction, Section 4.2 gives a brief background on the filtering and optical flow techniques that were used in this work and describes the stages of the proposed framework. Section 4.4 presents simulation results. Section 4.5 discusses the results and the contributions of the proposed methods.

4.2   Methods

In this section, we describe the key methods and steps of our image processing approach for eliminating false positives in the difference maps that drive the 2CMV representation. Some background information on the optical flow that was used in the framework and filtering of speckle noise is given first. The stages of the framework are explained in the subsequent sections.

4.2.1 Optical Flow with Relaxed Brightness Constraint

In section 2.1, two kinds of constraints were introduced in order to estimate the optical flow: the *smoothness constraint* and the *brightness constancy constraint*. In this section, we give an overview of the steps that modify the original optical flow approach. The modified optical flow method is employed in the proposed framework.

The brightness constancy constraint assumes that the brightness of a small area in the image remains constant as the area moves from image to image. Image brightness at the point (x, y) in the image at time t is denoted here as $I(x, y, t)$. If the point moves by δx and δy in time δt, then according to the brightness constancy constraint:

$$\frac{dI}{dt} = 0. \tag{4.1}$$

This can also be stated as:

$$I(\mathbf{r} + \delta\mathbf{r}, t + \delta t) = I(\mathbf{r}, t). \tag{4.2}$$

where $\mathbf{r} = (x, y, 1)^T$ and $\mathbf{r} + \delta\mathbf{r} = (x + \delta x, y + \delta y, 1)^T$. However, the brightness constancy constraint is restrictive. A less restrictive brightness constraint was chosen to address the intensity changes in SAR images. In Gennert and Negahdaripour (1987), it is proposed that the brightness constancy constraint can be replaced with a more general constraint that allows a linear transformation between the pixel brightness values. This way, the brightness change can be non-zero, or:

$$\frac{dI}{dt} \neq 0.$$

The formulation that allows a linear transformation between the pixel brightness values is less restrictive, and can be written as:

$$I(\mathbf{r} + \delta\mathbf{r}, t + \delta t) = M(\mathbf{r}, t)I(\mathbf{r}, t) + C(\mathbf{r}, t). \tag{4.3}$$

After using the Taylor series, the revised constraint equation can be obtained:

$$I_t + I_{\mathbf{r}} \cdot \mathbf{r}_t - I m_t - c_t = 0, \tag{4.4}$$

where $m_t = \lim_{\delta t \to 0} \delta m / \delta t$ and $c_t = \lim_{\delta t \to 0} \delta c / \delta t$. The relaxed brightness constraint error is:

$$\epsilon_I = \iint (I_t + I_{\mathbf{r}} \cdot \mathbf{r}_t - I m_t - c_t)^2 \, dx \, dy. \tag{4.5}$$

Equation 4.5 can be combined with the other constraint errors to produce the final functional to be minimized:

$$\epsilon_{total} = \epsilon_I + \lambda_s \epsilon_s + \lambda_m \epsilon_m + \lambda_c \epsilon_c. \tag{4.6}$$

where λ_s, λ_m, and λ_c are error weighting coefficients. The remaining errors are given as:

$$\epsilon_s = \iint ||\nabla \mathbf{r}_t||_2^2 dx dy,$$

$$\epsilon_m = \iint ||\nabla m_t||_2^2 dx dy,$$

$$\epsilon_c = \iint ||\nabla c_t||_2^2 dx dy.$$

Substituting the approximated Laplacians into the Euler-Lagrange equations, a single matrix equation can be derived:

$$\mathbf{A}\mathbf{f} = \mathbf{g}(\bar{\mathbf{f}}), \tag{4.7}$$

where

$$\mathbf{A} = \begin{pmatrix} I_x^2 + \lambda_s & I_x I_y & -I_x I & -I_x \\ I_x I_y & I_y^2 + \lambda_s & -I_y I & -I_y \\ -I_x I & -I_y I & I^2 + \lambda_m & I \\ -I_x & -I_y & I & 1 + \lambda_c \end{pmatrix}, \mathbf{f} = \begin{pmatrix} u \\ v \\ m_t \\ c_t \end{pmatrix}, \quad \mathbf{g}(\bar{\mathbf{f}}) = \begin{pmatrix} \lambda_s \bar{u} - I_x I_t \\ \lambda_s \bar{v} - I_y I_t \\ \lambda_m \bar{m}_t + I_t I \\ \lambda_c \bar{c}_t + I_t \end{pmatrix}.$$

These equations have to be solved iteratively. The solution is given by:

$$\mathbf{f} = \mathbf{A^{-1}} \mathbf{g}(\mathbf{\bar{f}}),\tag{4.8}$$

where

$$\mathbf{A^{-1}} = \frac{1}{\alpha} \begin{pmatrix} \lambda_c\lambda_m\lambda_s + \lambda_m\lambda_s + I^2\lambda_c\lambda_s + I_y^2\lambda_c\lambda_m & -I_xI_y\lambda_c\lambda_m & I_xI\lambda_c\lambda_s & I_x\lambda_m\lambda_s \\ -I_xI_y\lambda_c\lambda_m & \lambda_c\lambda_m\lambda_s + \lambda_m\lambda_s + I^2\lambda_c\lambda_s + I_y^2\lambda_c\lambda_m & I_yI\lambda_c\lambda_s & I_y\lambda_m\lambda_s \\ -I_xI\lambda_c\lambda_s & I_yI\lambda_c\lambda_s & (I_x^2 + I_y^2)\lambda_c\lambda_s + \lambda_c\lambda_s^2 + \lambda_s^2 & -I\lambda_s^2 \\ I_x\lambda_m\lambda_s & I_y\lambda_m\lambda_s & -I\lambda_s^2 & (I_x^2 + I_y^2)\lambda_m\lambda_s + \lambda_m\lambda_s^2 + I^2\lambda_s^2 \end{pmatrix}$$

and

$$\alpha = \lambda_m\lambda_s^2 + I^2\lambda_c\lambda_s^2 + (I_x^2 + I_y^2 + \lambda_s)\lambda_c\lambda_m\lambda_s.$$

The equations can then be solved iteratively for other pixels with:

$$\mathbf{f^{k+1}} = \mathbf{A^{-1}}\mathbf{g}(\mathbf{\bar{f}^k}),\tag{4.9}$$

where k is the iteration number. This way the matrix $\mathbf{A^{-1}}$ need only be computed once. More details about this optical flow algorithm can be found in Gennert and Negahdaripour (1987). Two side-by-side sample flow fields generated by the original optical flow method and the Relaxed Brightness method are provided in Figure 14.

40
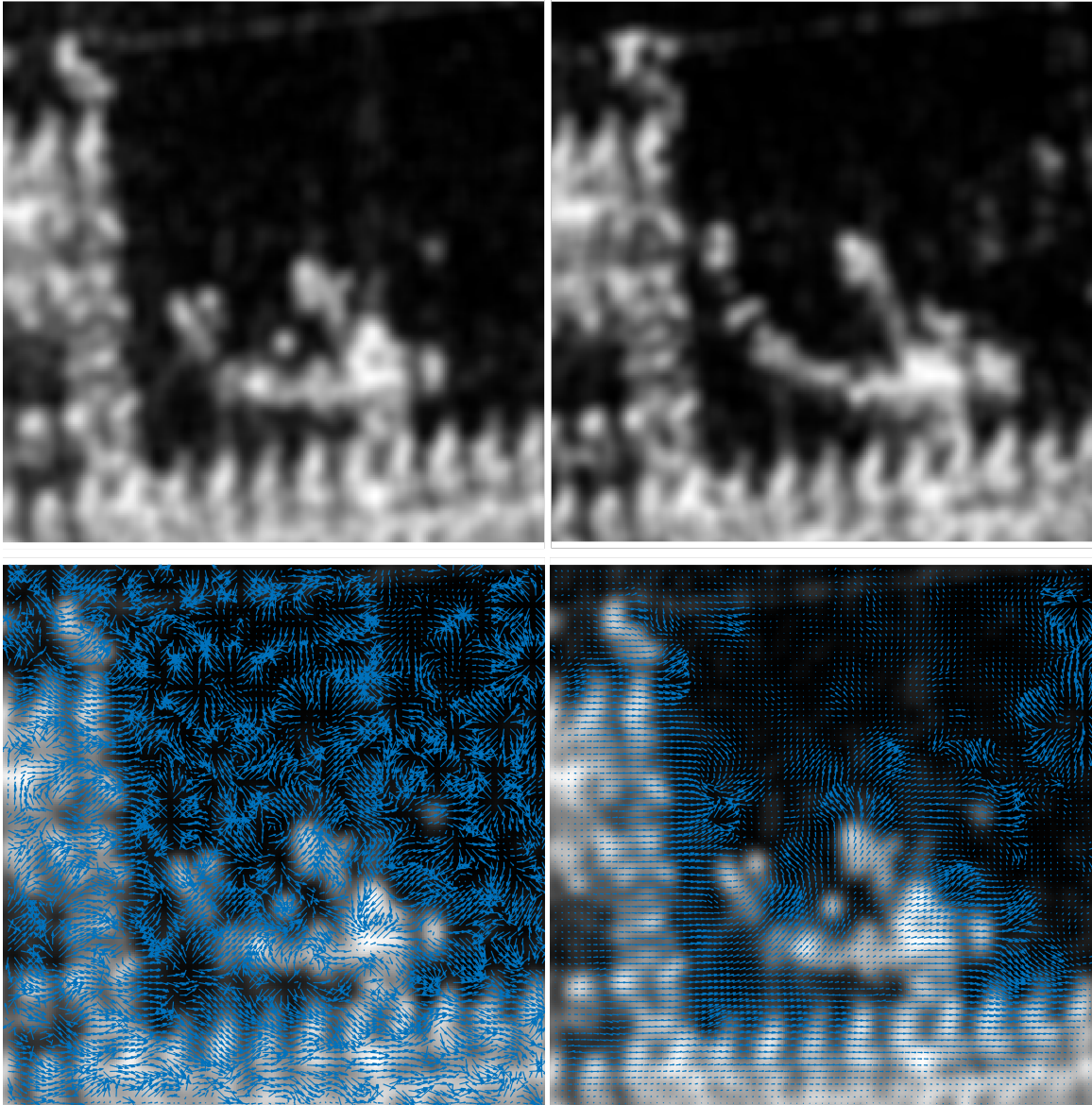
Figure 14. Reference image (top left), Mission image (top right), original Horn-Schunck optical flow field (bottom left) and the optical flow field produced with the Relaxed Brightness method (bottom right). Note that the Relaxed Brightness method provides a smoother, more natural flow field than the Horn-Schunk method. (Flow field vectors in the images are enlarged and binned to better illustrate flow field behavior.)

4.2.2   Denoising

Speckle noise is an inherent problem in SAR images [Dekker (1998)] and causes difficulties for image interpretation by increasing the mean grey level of a local region. It is caused by coherent processing of backscattered signals from multiple distributed targets.

In order to mitigate speckle noise effects, we tested different speckle filter designs. Filters that were included in the testing were Frost [Frost *et al.* (1982)], Enhanced Frost [Lopes *et al.* (1990b)], Lee [Lee (1980)], Gamma-MAP [Lopes *et al.* (1990a)], SRAD [Yu and Acton (2002)] and Non-Local Means [Coupe *et al.* (2009)]. In the end, Enhanced Frost filter was used in the algorithm due its relatively straightforward implementation and comparable performance. In this section, some of the tested filters are briefly presented.

4.2.3   Lee Filter

The Lee filter uses an adaptive approach. If the variance over an area is low or constant, then this area will be smoothed. In the case of high variance, smoothing will not be performed. It is assumed that the speckle noise is multiplicative, and the SAR image is approximated by a linear model.

$$I(t) = R(t) \cdot u(t). \tag{4.10}$$

where $t = (x, y)$, $I(t)$ is the recorded value, $u(t)$ is the multiplicative speckle noise that is independent of $R(t)$ and, $R(t)$ denotes the corresponding terrain reflectivity. Following Lopes *et al.* (1990b), the general speckle reduction filter estimate $\hat{R}(t)$ can

be formulated as

$$\hat{R}(t) = I(t)W(t) + \bar{I}(t)(1 - W(t)). \tag{4.11}$$

where $W(t)$ is the weighting function and, $\bar{I}(t)$ is the local mean. The weighting function $W(t)$ for the Lee filter is given by

$$W(t) = 1 - \frac{C_u^2}{C_l^2(t)}. \tag{4.12}$$

where $C_u = \sigma_u/\bar{u}$ is the noise variation coefficient of the image and, $C_l = \sigma_l(t)/\bar{I}(t)$ is the variation coefficient of the local region (filter window) [Shi and Fung (1994)].

4.2.4   Frost Filter

The Frost filter estimates the scene reflectivity by convolving the observed image with the impulse response of the SAR system. The impulse response is obtained by minimizing the mean square error (MSE) between the image and the scene reflectivity model which is assumed to be an autoregressive process. The Frost filter can be given as

$$m(t) = K_1 \exp\left[-KC_l^2(t_o)|t|\right]. \tag{4.13}$$

where K is the filter parameter, $C_l(t_o)$ is computed over a uniform moving window centered at t_o, K_1 is normalizing constant and, $|t|$ is the absolute value of the pixel distance from the center pixel to its neighbors in the filter window [Lopes *et al.* (1990b)].

4.2.4.1   Enhanced Frost Filter

In Lopes *et al.* (1990b), it was proposed to divide images into areas of three classes. The first class takes the homogeneous areas. The second class takes the heterogeneous areas in which the speckle noise is to be reduced, while preserving texture.

The third class corresponds to the areas containing isolated point targets which the filter should preserve. The Enhanced Frost filter output can be given as

$$
\hat{I}(t_o) = \begin{cases} \bar{I} & \text{for } C_l(t_o) < C_u \\ I * K_1 \exp\left[-K(C_l(t_o) - C_u)/(C_{max} - C_l(t_o))|t|\right] & \text{for } C_u \leq C_l(t_o) \leq C_{max} \\ I & \text{for } C_l(t_o) \geq C_{max}. \end{cases}
$$

(4.14)

where $t_o = (x_o, y_o)$ is the spatial coordinate, $\bar{I}$ is the mean intensity value inside the kernel, K is the filter parameter, K_1 is a normalizing constant, and $|t|$ is the absolute value of the pixel distance from the center of the kernel at t_o. The rest of the parameters are

$$
C_u = \sqrt{\frac{1}{L}}
$$

$$
C_l(t_o) = \sigma/\bar{I}
$$

$$
C_{max} = \sqrt{1 + \frac{2}{L}}
$$

where C_u is the speckle coefficient of variation of the image, $C_l(t_o)$ is the local coefficient of variation of the filter kernel centered at t_o, C_{max} is the upper speckle coefficient of variation of the image, and L is the number of looks. In our implementation, instead of L, we used "equivalent number of looks" (ENL). It can be defined as $ENL = \mu^2/\sigma^2$.

Other filters that were included in the testing were Gamma-MAP filter [Lopes *et al.* (1990a)], SRAD filter [Yu and Acton (2002)] and a Non-Local Means filter [Coupe *et al.* (2009)]. In the end, the Enhanced Frost filter was chosen to be used in the algorithm due its relatively straightforward implementation and comparable performance. Implementations of SRAD and Non-Local Means filters were readily available on the authors' websites. The need for parameter adjustments was a dis-

44

advantage for these filters. Figures 15 and 16 show the sample test results for the implemented filters.
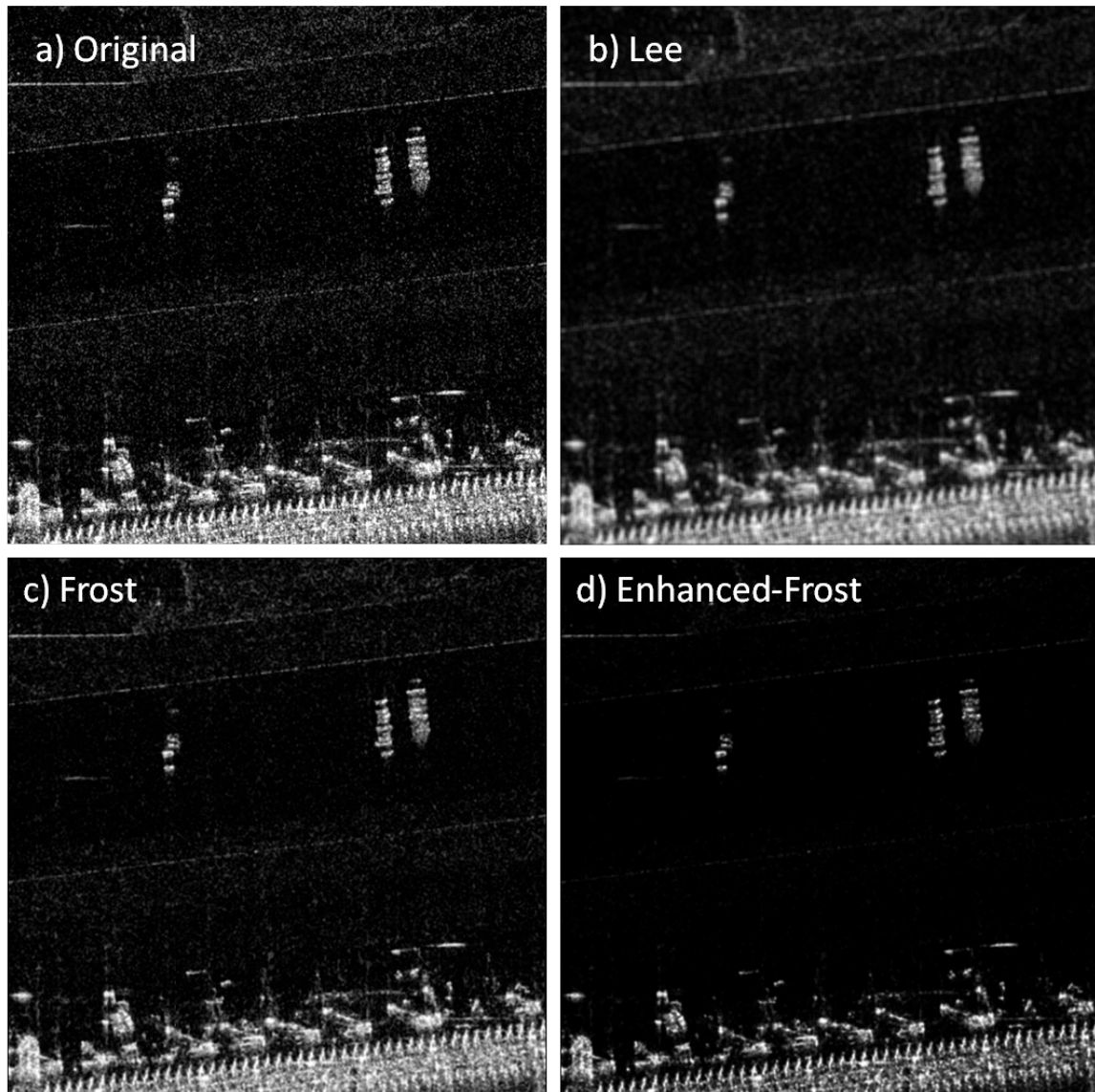
Figure 15. Samples of the filter tests. a)Original b)Lee filter c)Frost filter d)Enhanced Frost filter. Note that Enhanced Frost is more effective in removing the speckle noise.
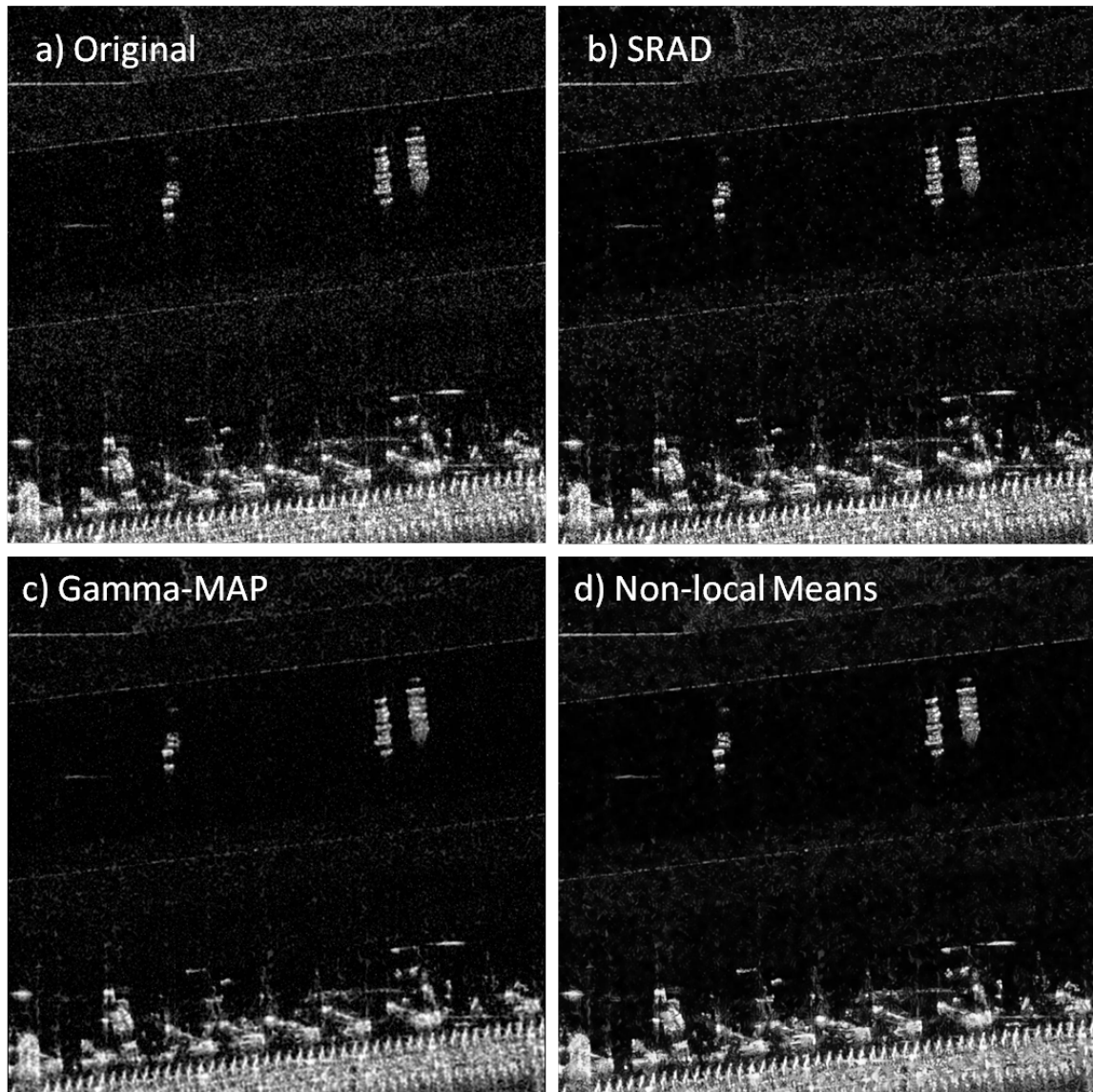
Figure 16. Samples of the filter tests. a)Original b)SRAD c)Gamma-Map filter
d)Non-local Means filter. The code for SRAD and Non-local Means can be found
online. Different results can be obtained by changing the parameters of these filters.

46

4.3 Image Processing Steps

In this section, the image processing approach for extracting difference maps is described step-by-step. All of the underlying code was written in the MATLAB computing environment. The inputs are two registered SAR images of the same field of view that were taken at different times, i.e. "reference" image and "mission" image. Due to the large size of the images, a block based approach was employed. The steps that were implemented are summarized in Table 1. Each step is detailed in the following subsections and example outputs are provided. A detailed flow diagram can be seen in Figure 17.

Table 1. Steps of the proposed framework.

Outline

- Preprocessing
    - Read NITF images (a SAR image format)
    - Denoising
    - Smoothing

- First Stage: Difference Maps
    - Image Subtraction
    - Calculate image differences based on adaptive thresholds
    - Keep significant difference areas

- Second Stage: Optical Flow
    - Execute block-based optical flow
    - Perform object matching on difference maps from the first stage
    - Matched objects are excluded from the final image because they are false positives

- Third Stage: Object Extraction & Optical Flow
    - Use adaptive thresholds to extract possible objects from the original images
    - Match the results from the second stage with extracted possible objects
    - Parts of the larger objects are eliminated
    - Perform Optical Flow matching on the extracted objects (improves performance)

- Fourth Stage: Final Elimination
    - Determine all the eliminated areas
    - Check whether the eliminated areas are related to the existing areas or not

- Fifth Stage: Intensity Changes without Objects (Optional)
    - Downsample the original images by a factor of 5
    - Use 2D Wiener Filter and an averaging filter on the downsampled images.
    - Image Subtraction
    - Use adaptive threshold to find areas with significant intensity changes
    - Upsample
    - Overlay the areas on the original images

- Sixth Stage: Merging
    - Use a moving window to merge all the areas that are very close to each other
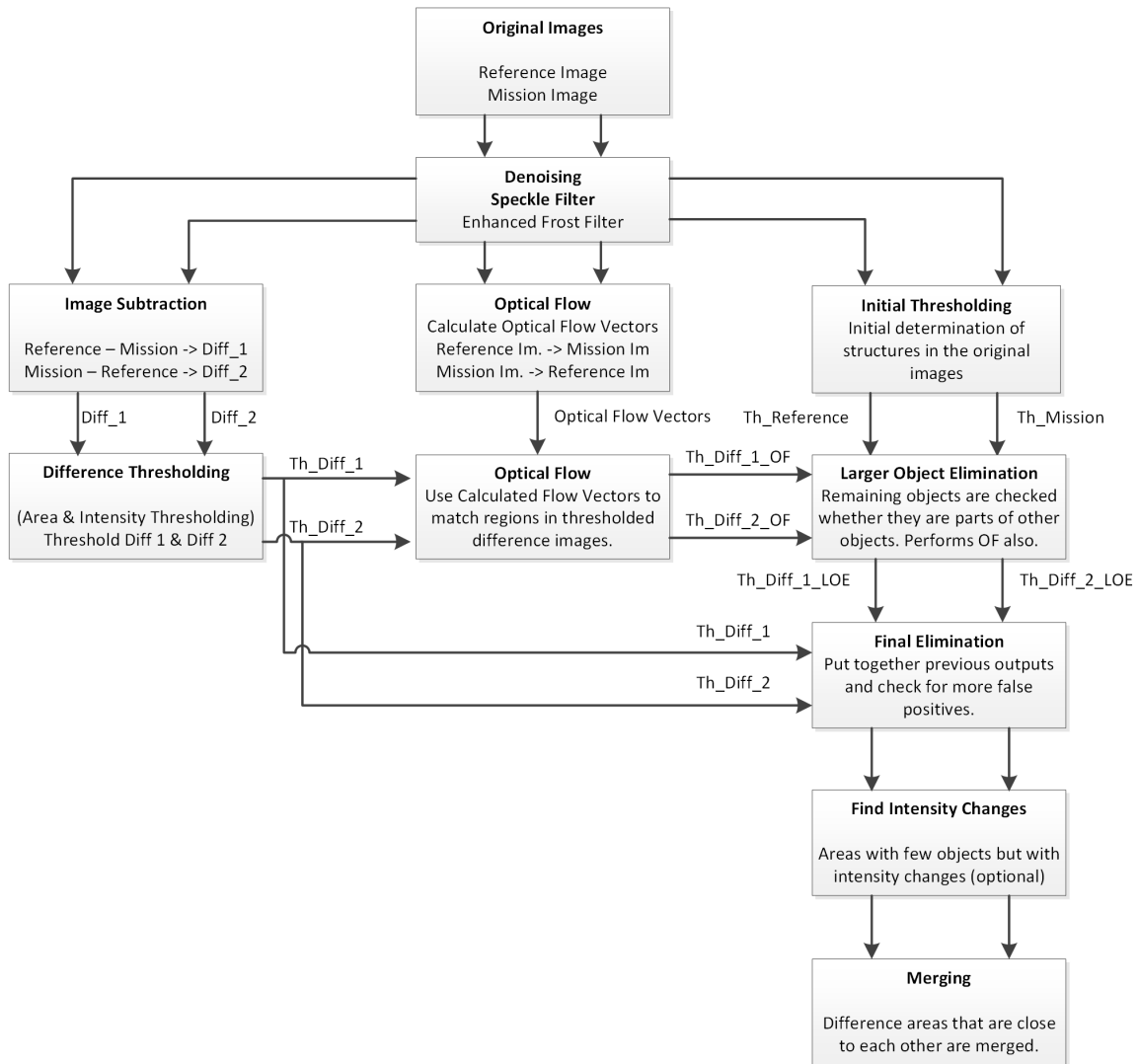
Figure 17. Flow diagram of the proposed algorithm.
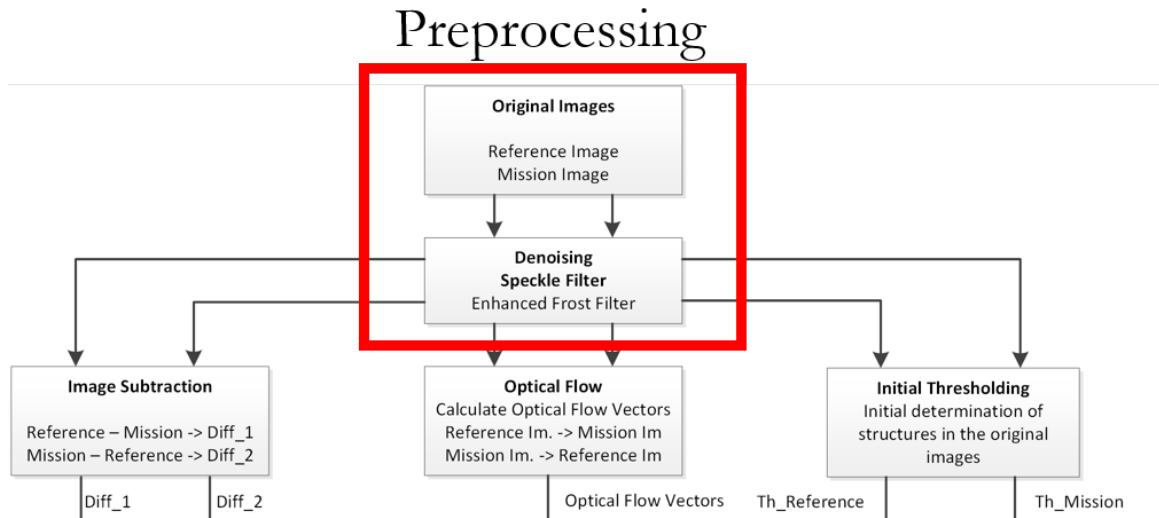
Preprocessing

Figure 18. Preprocessing portion of the flow diagram.

4.3.1   Preprocessing

An NITF-reader script was developed to read the NITF image header informa-
tion and extract the image data for processing. Preprocessing is the first step in the
flow diagram, and it is shown in Figure 18. Small test areas were chosen for pro-
cessing based on guidance from LMC. A sample test area is shown in Figure 19. An
Enhanced Frost filter with a 5x5 window size was first used to denoise the images.
Then, a 9x9 pixel low pass filter was used to smooth the test areas in order to atten-
uate the effects of the remaining speckle noise. Figure 20 shows the residual image
after subtracting the filtered image from the original one.
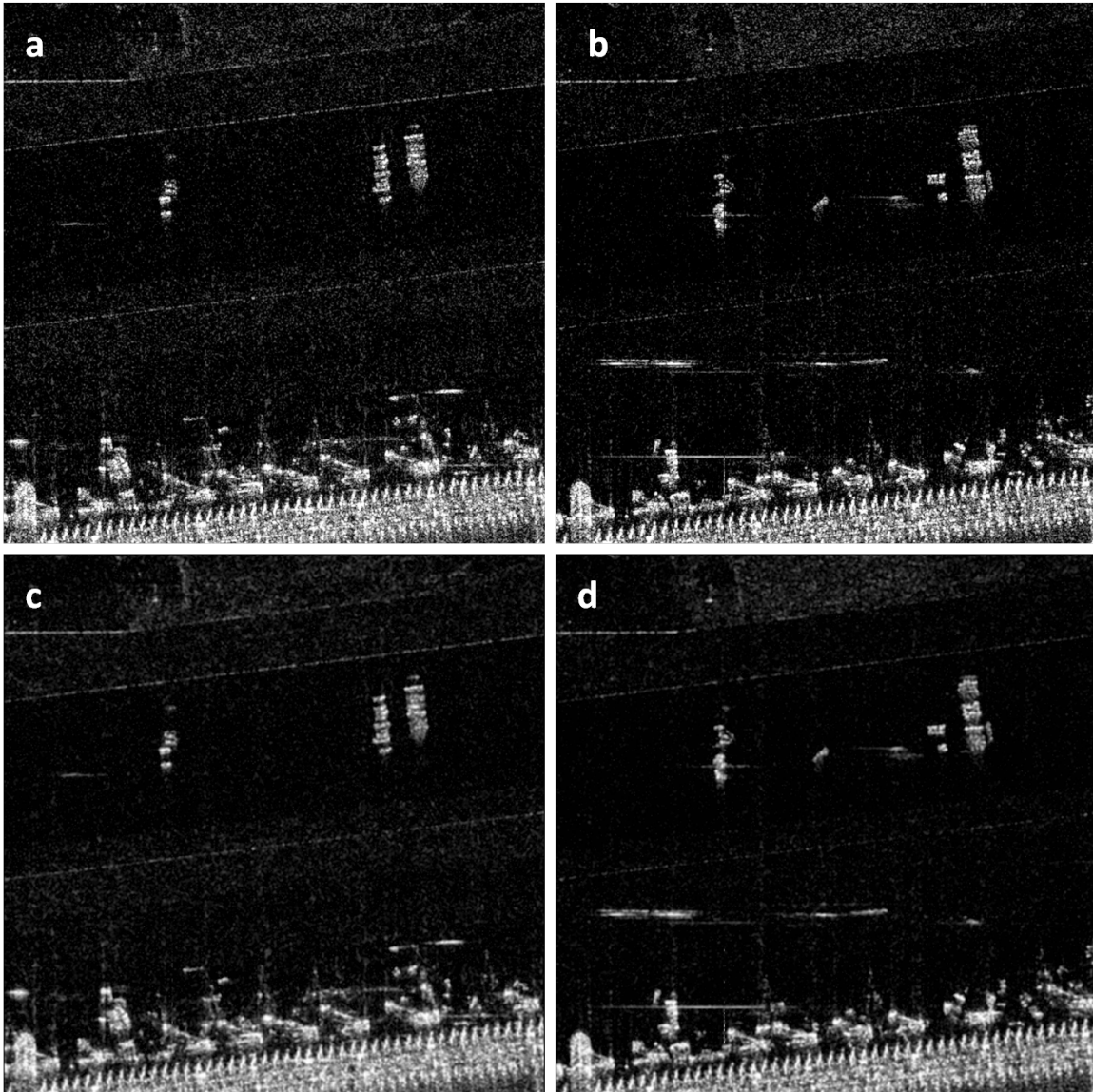
Figure 19. A small image test area of an airport from: a) the reference image, b) the mission image, c) Enhanced Frost Filtered reference image, and d) Enhanced Frost Filtered mission image.
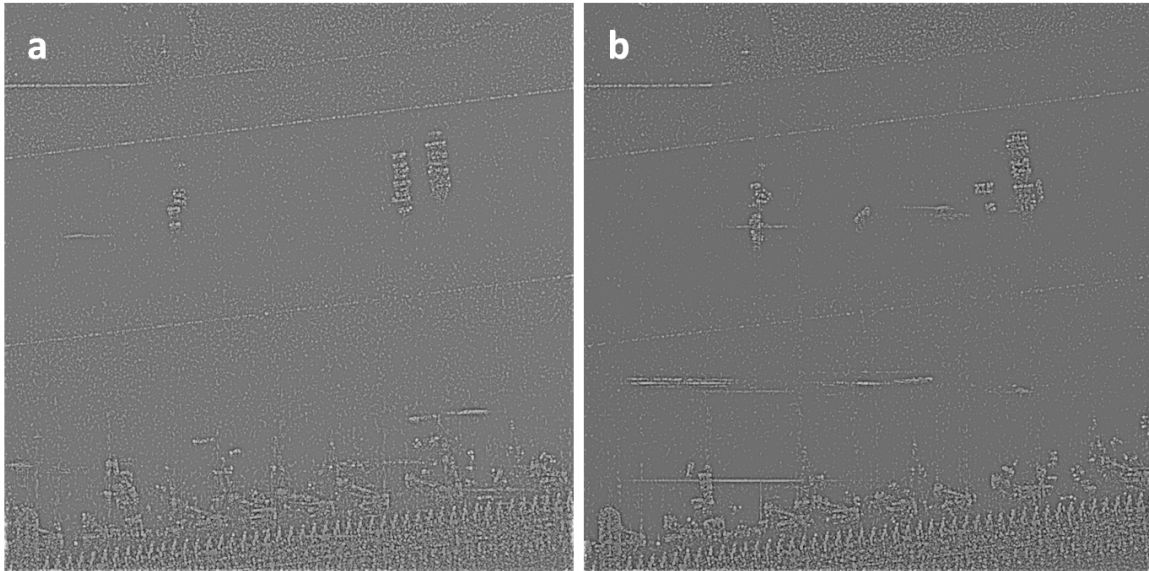
Figure 20. Residual after filtering a) original reference image - filtered reference image, b) original mission image - filtered mission image.

4.3.2   First Stage Difference Maps

This portion of the algorithm is shown in Figure 21. Since the reference and mission images are pre-registered, meaningful differences between the two can be identified by simply subtracting one image from the other. The result of this operation is shown in Figure 22. Initially, after subtraction, a local intensity threshold was applied to identify significant differences between the two images. The local intensity threshold was calculated as:

$$T = \mu_{dif} - \alpha\sigma_{dif}, \tag{4.15}$$

where μ_{dif} and σ_{dif} are the mean and standard deviation of the difference image intensity, respectively, and α is a user-defined constant. Based on the feedback from LMC, it was noted that this was not a good assumption for the noise distribution in the image, because the SAR signal is Rayleigh distributed. In order to keep the complexity simple, a block based approach was used. Because each block has different content, the thresholds might differ significantly. For this reason, fixed upper and lower thresholds were set so that the threshold would not go below a certain value. This method improved the difference object extractions.

Next, in the binary difference maps, object properties such as area and location are calculated. Based on a user-defined area threshold (30 pixels), insignificant difference areas are excluded from the difference maps. Figure 22 shows images before and after this operation. The remaining difference areas are then overlaid onto the original images. To create a 2CMV image, the areas that exist only in the reference image are colored in cyan and the areas that exist only in the mission image are colored in red. A sample 2CMV image is shown in Figure 23.
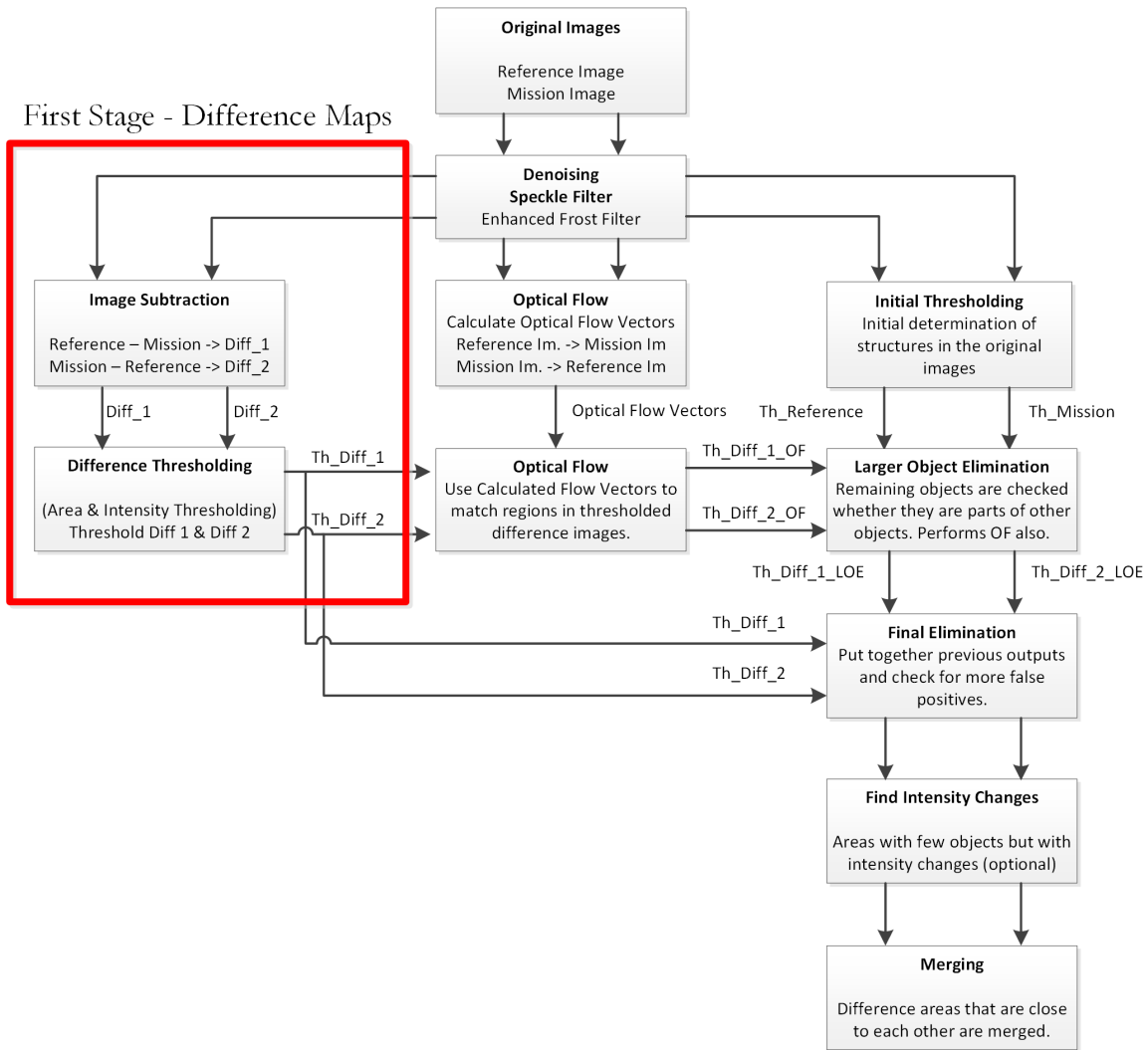
Figure 21. Flow diagram first stage: difference maps.
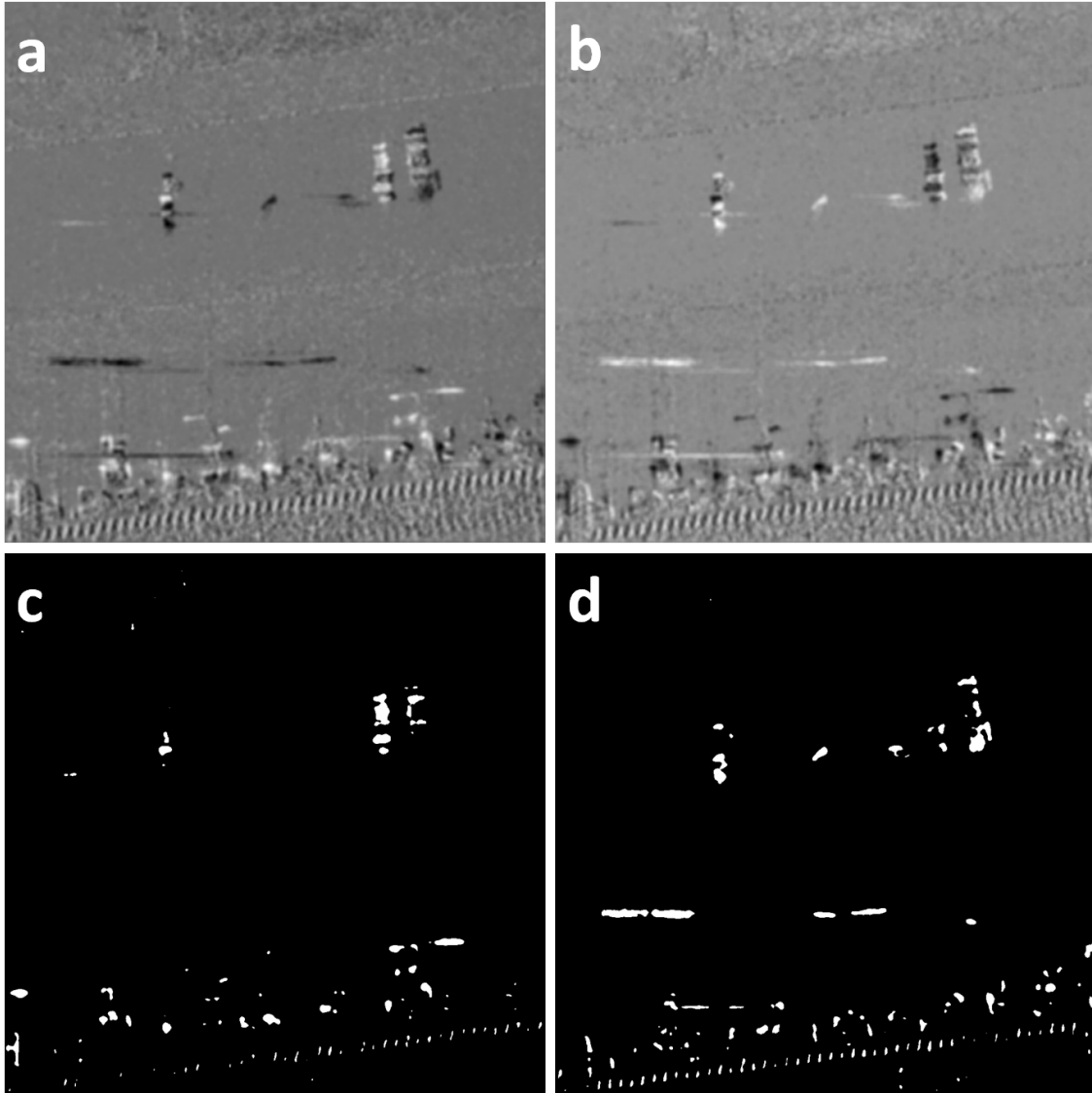
Figure 22. Raw difference images: a) (reference-mission), b) (mission-reference). Thresholded images: c) thresholded version of (a), d) thresholded version of (b).
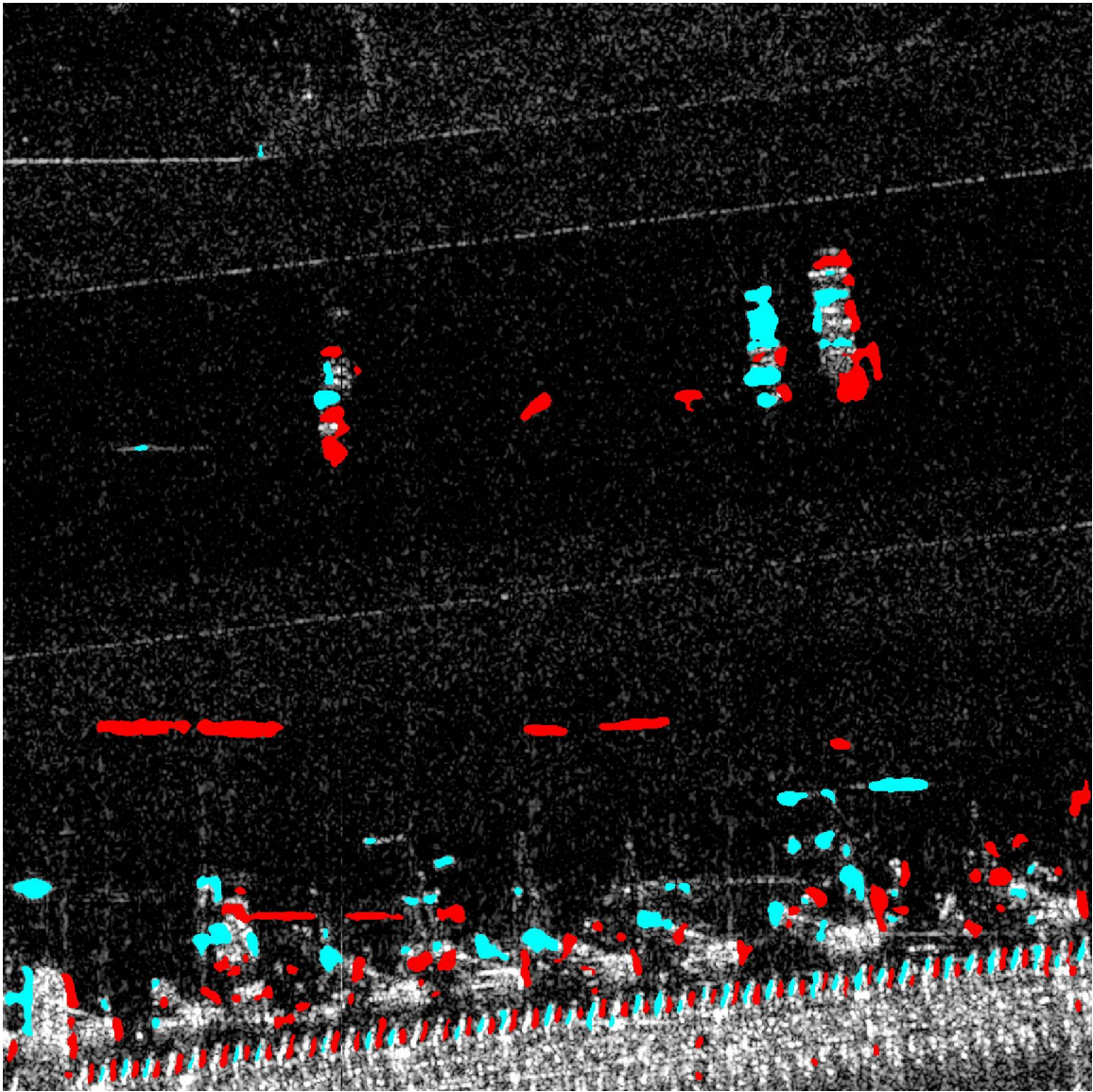
Figure 23. 2CMV image after filtering, smoothing, intensity thresholding, and area thresholding. Color coded difference areas are overlaid onto the original image. Note that there are several false positives.

4.3.3 Second Stage Optical Flow

Figure 23 displays a 2CMV image wherein it is clear that additional processing is needed to improve results. The primary improvement that is targeted with additional processing is reducing the number of false positives in the image. This step is shown in Figure 24. This goal can be accomplished with the use of the optical flow method described in section 4.2.1. After testing several values, it was seen that setting λ_s in (4.7) to a small value around 0.01 gives the best results. To manage computational complexity, the optical flow algorithm is performed on 256x256 pixel image blocks. Note that optical flow is calculated based on the original reference and mission images. Figure 25 shows a 256x256 block from the original image. This block was used to produce the sample figures shown later in this section. After executing the optical flow algorithm, the resultant flow vectors are applied to the two first stage difference maps to find object matches. Optical flow vectors are used to move the difference objects in the reference image in the flow direction toward the mission image. The destination of an object is then compared with the same location in the mission image. If there is a matching object in the mission image, then the two objects are excluded from the difference maps. The same process is performed in the opposite direction to match mission image difference objects in the reference image. Figures 26-27 illustrate these steps. Red areas indicate the destinations of difference objects after the optical flow vectors are applied. Note that after applying the optical flow vectors to the reference image difference objects, their destinations overlap with difference object locations in the mission image (in many cases). The overlapped objects are then removed from both. After removal, 15 labeled difference objects remain in the example instead of 30. Note again that this process is performed for both the ref-

erence and mission images. The final 2CMV image is shown in Figure 28. Another illustration of optical flow is shown in Figure 29.
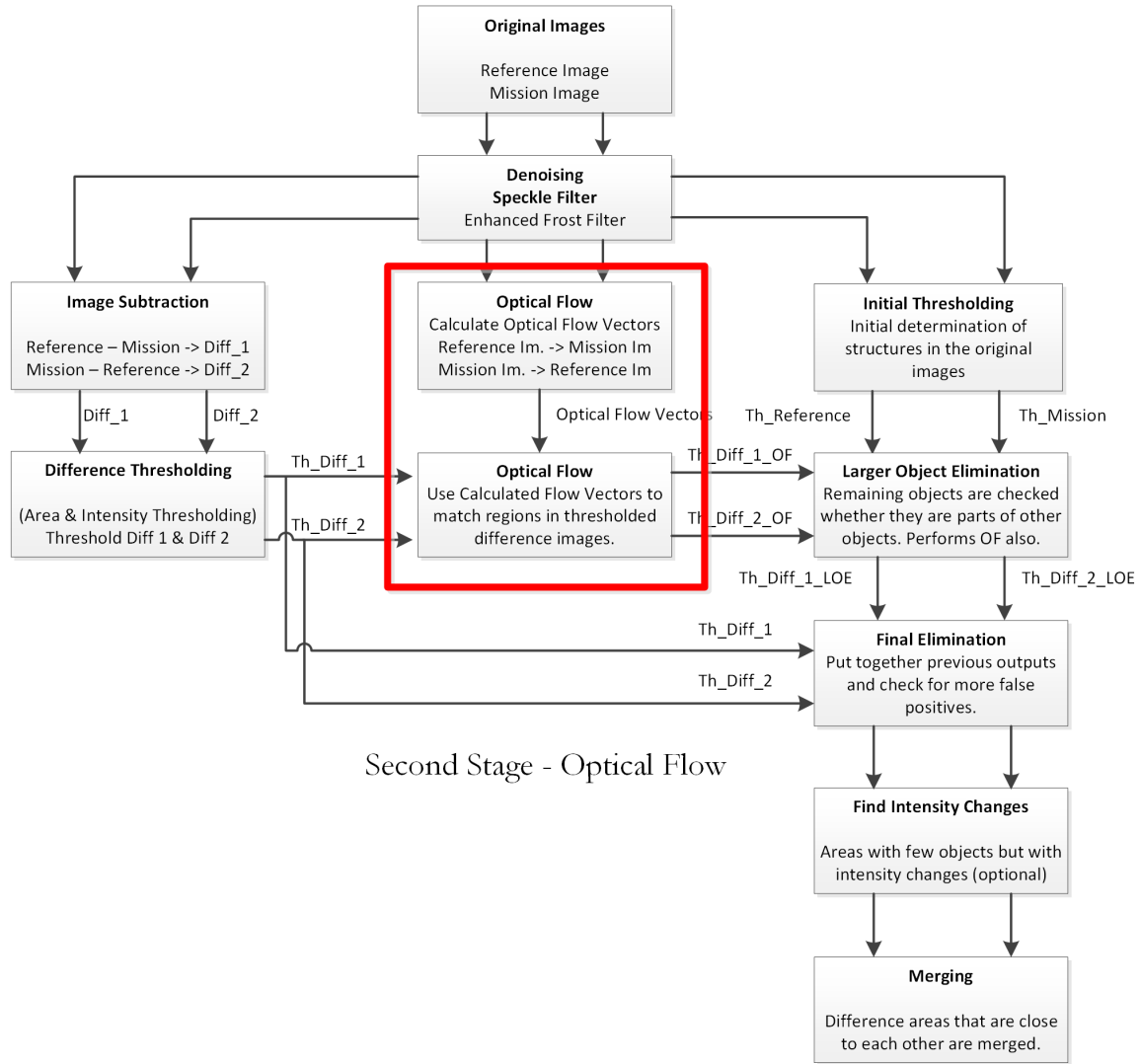
Figure 24. Flow diagram second stage: optical flow.
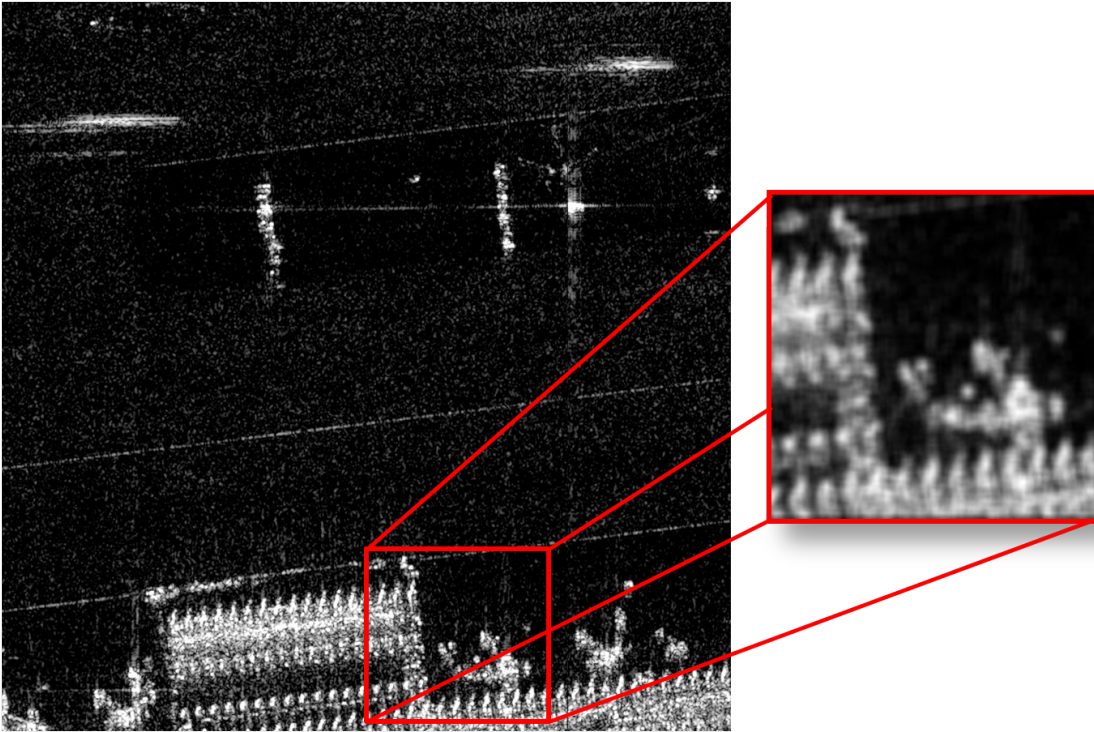
Figure 25. A 256x256 pixel image block to be processed with the optical flow algorithm. Note that a different area is shown in this Figure.

Reference image Differences of the reference image 30 Labeled areas

Mission image Differences of the mission image 30 Labeled areas
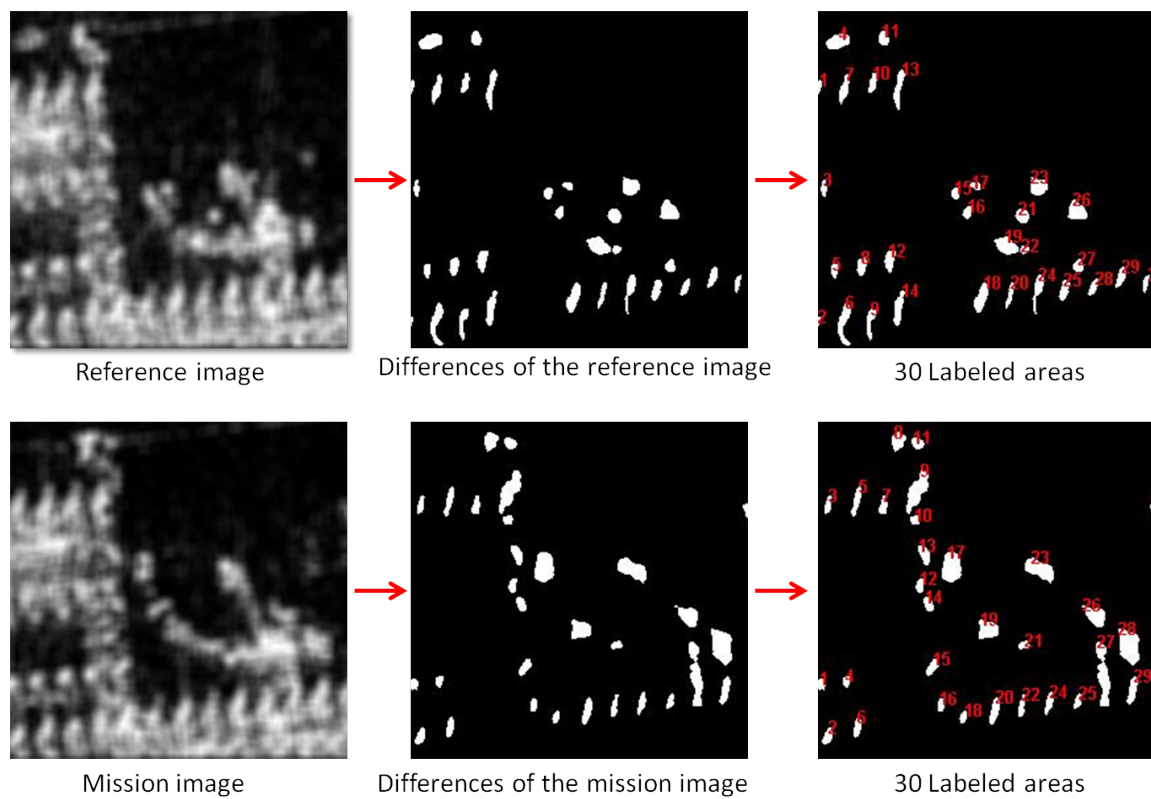
Figure 26. Difference areas are labeled and prepared to be matched via flow vectors.
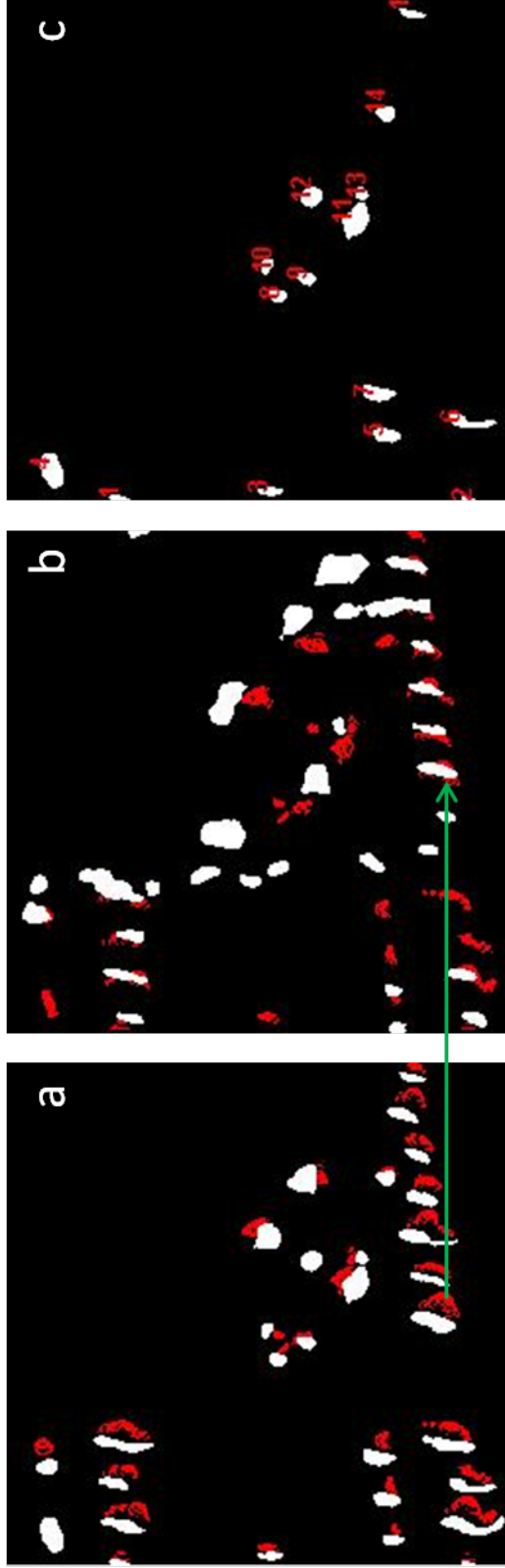
Figure 27. Subfigures show: a) after optical flow vectors are used to move the object pixels along the flow direction on the reference image difference map and b) after optical flow vectors are used to move the reference image object pixels along the flow direction on the mission image difference map. Note that after applying the optical flow vectors to the reference image, reference image difference object destinations match mission image difference object locations in many cases. The overlapped areas are then removed in c) where 15 labeled difference areas remain instead of 30.
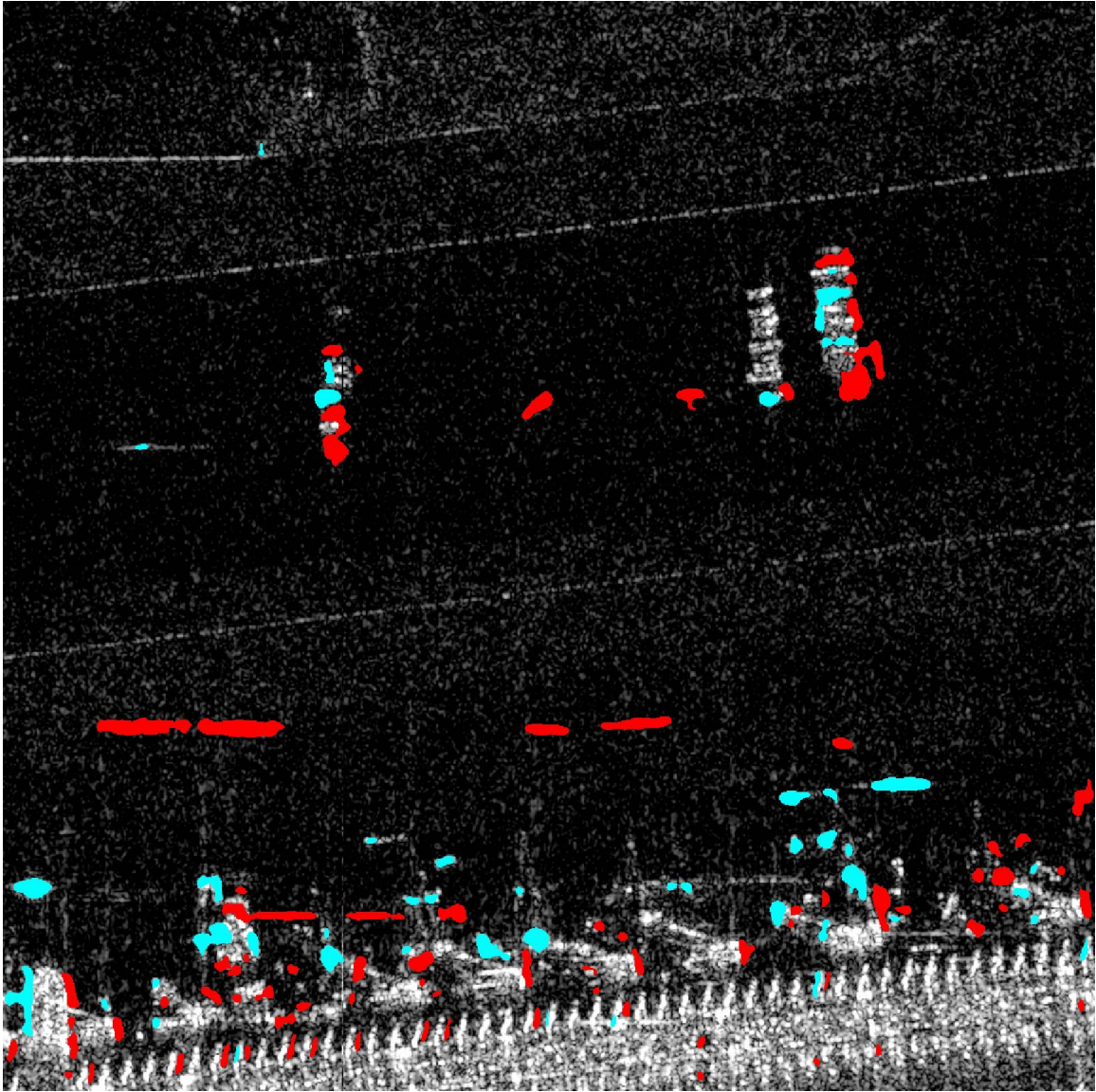
Figure 28. Final 2CMV image after optical flow processing. False positives are reduced.

Cropped Reference & Mission Images

Original Reference Image

Difference Image
35 labeled areas

Optical Flow Field

New Difference Image
18 labeled areas
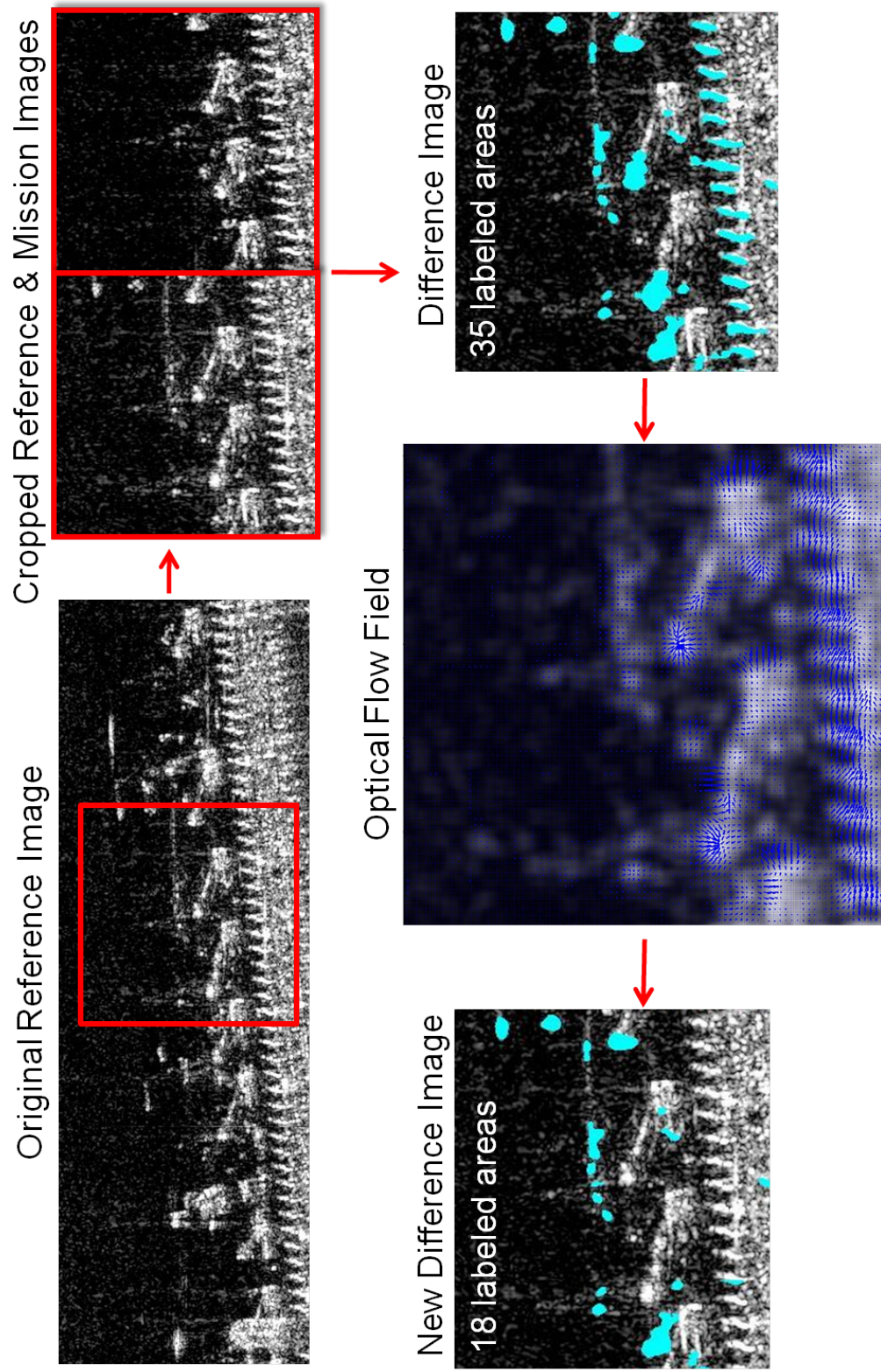
Figure 29. This shows how effective the OF algorithm is even if it is used by itself.

63

4.3.4   Third Stage Object Extraction & Optical Flow

This stage has two main parts: extraction and elimination. Extraction is performed by an adaptive thresholding method that is similar to the one used in the first stage. In this stage the thresholding is performed on the original images to extract(or label) objects. This is the 'Initial Thresholding' part in Figure 30. Then these two thresholded binary masks are processed in two ways. First the optical flow vectors are used on the images to match the objects. Again, the difference from the second stage is the vectors are used on the original thresholded images, not on difference maps. Since the goal is to find the objects that moved between two images, not all extracted objects are matched. The objects with the possibility of movement are checked. If there is a match, the difference map is checked again whether there is a change registered in that location. This step helps further reduce the false positives. After this process, the registered difference objects are checked again through original thresholded images. This part of the process checks whether the difference object is a part of a larger object in the original image. If the object is found to be a part of a larger object, the same location in the other image is checked for the same object. In the case of two similar objects around the same location, it can be assumed that the difference object is a false negative and excluded from the difference map. It can be seen how these two methods complement each other in Figure 31. After these two methods are performed, the output of this stage is generated by simply taking the intersection of the two results.
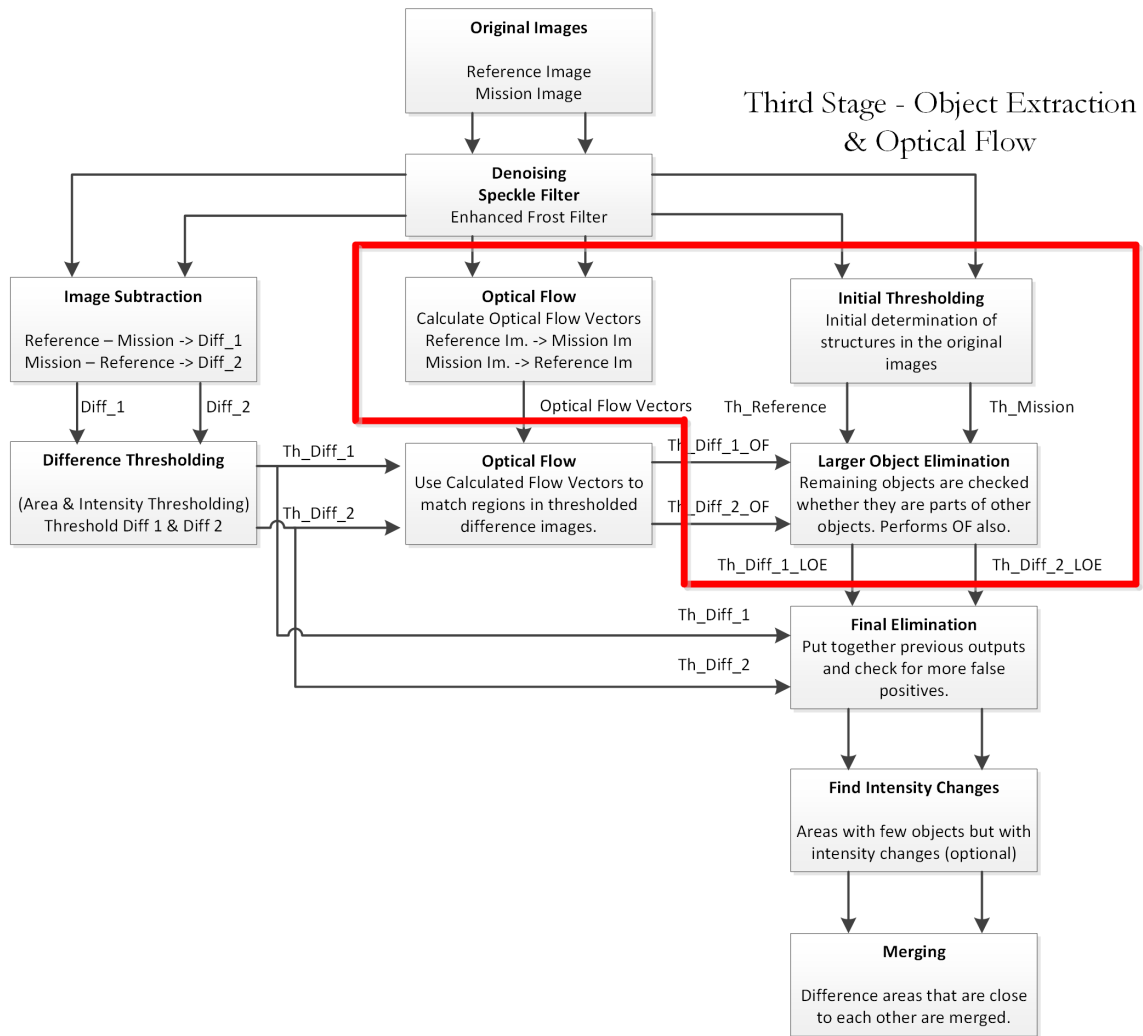
Figure 30. Flow diagram third stage: object extraction & optical flow.
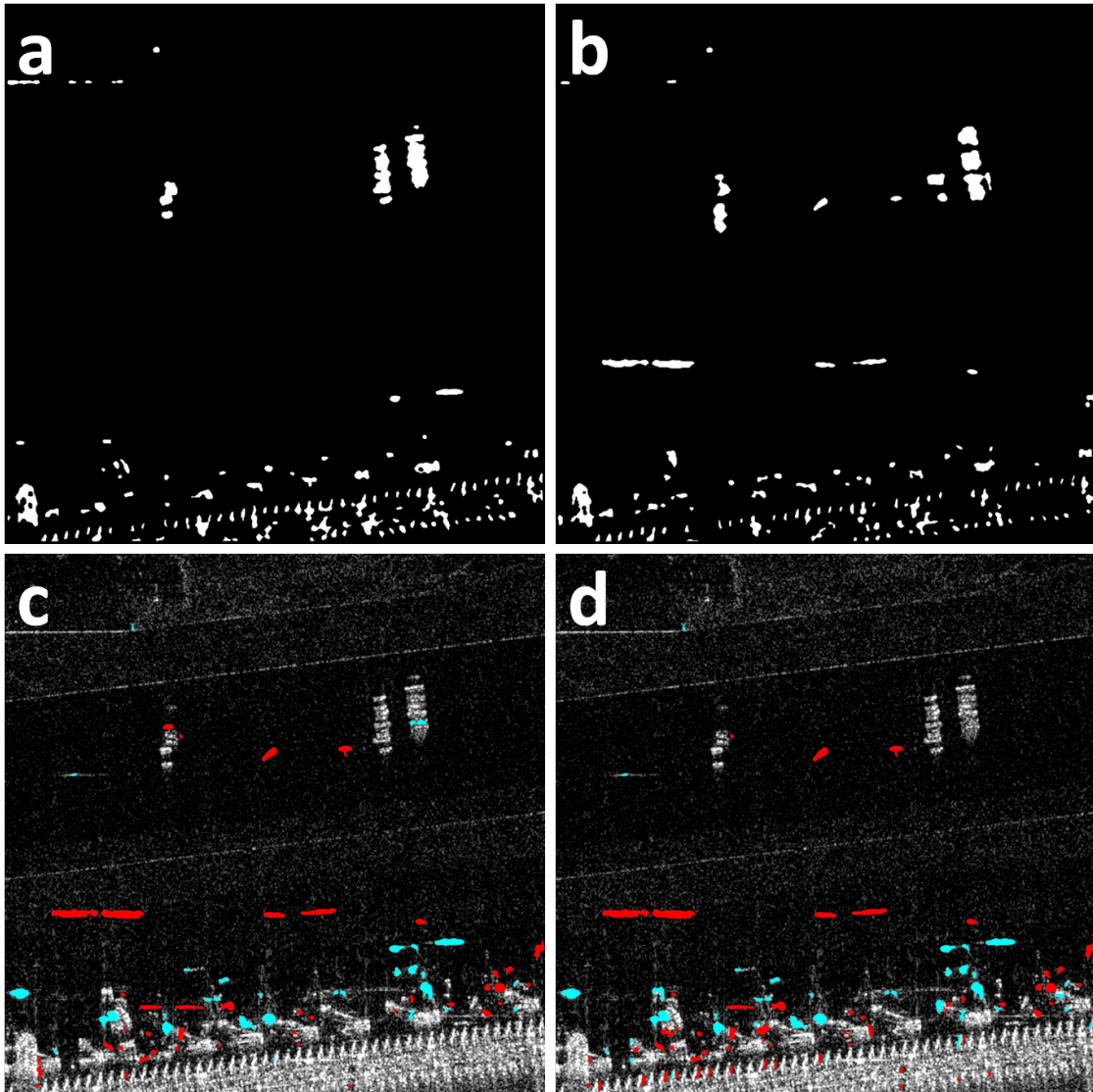
Figure 31. Third stage: object extraction & optical flow. a) thresholded reference image, b) thresholded mission image, c) optical flow vectors are used to match structures and compared with the difference map, d) difference objects are checked whether they are part of larger objects or not. Note that optical flow is efficient in removing structures that are close to each other and in a pattern.

4.3.5 Fourth Stage Final Elimination

This stage basically puts together the outputs of the previous stages and checks the vicinity of excluded objects in case there are more false positives around that location. Figure 32 shows the stage in the flow diagram and Figure 33 shows the output of this stage.
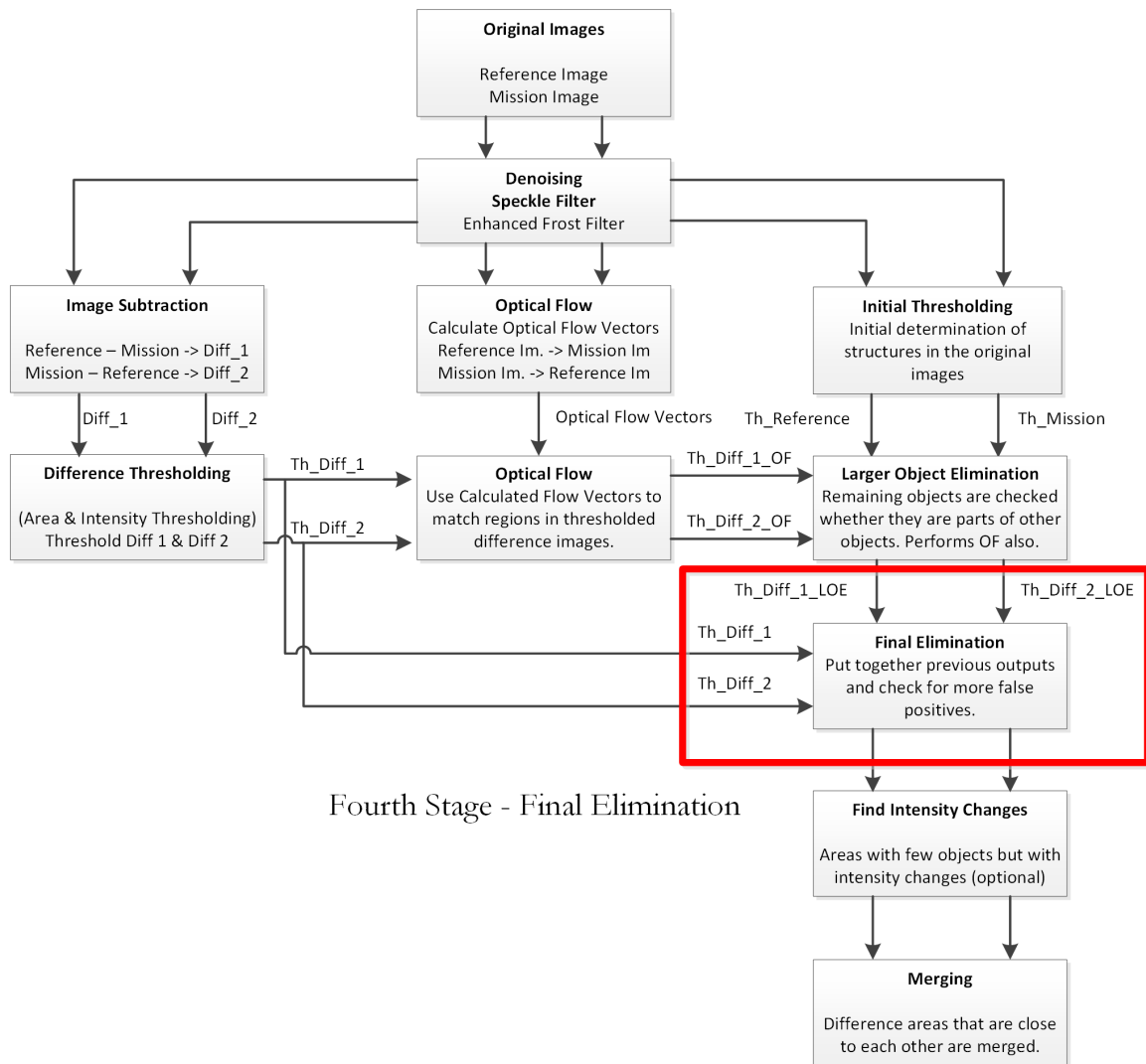
Figure 32. Flow diagram fourth stage: final elimination.
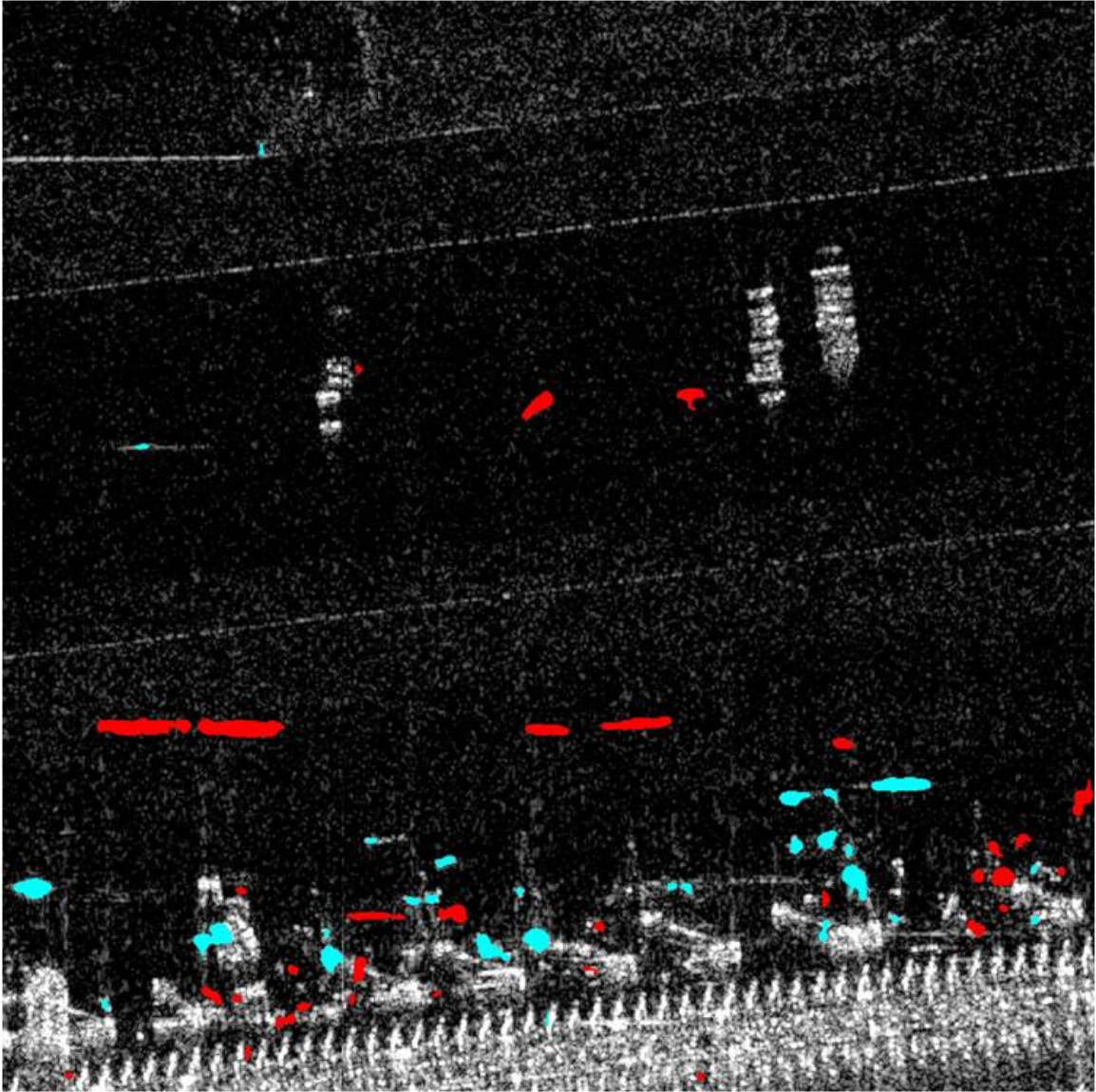
Figure 33. The output after stage 4. False positives are reduced.

4.3.6 Fifth Stage Intensity Changes without Objects (Optional)

This stage was added later based on the feedback received from LMC. It is shown in Figure 34. Some particular areas in the image may contain significant intensity changes even though there is no object in the scene. One example might be a newly painted surface in the mission image. It might be useful to notice this change between images. It is a challenge to obtain the areas without objects. A simple method was adopted to achieve this. First, the images are downsampled by a factor of 4(or 5). A 2D Wiener filter with a 5x5 window was used on the images (This is a built-in MATLAB function). Then an 11x11 averaging filter was used. This way, most of the high frequency content is filtered out. A simple threshold lights up most of the areas with changes. This small intensity change mask can be upsampled and overlaid on the original image. The method also checks for existing objects in the location. If objects are found the area is not highlighted. In the algorithm this stage can be turned on by a flag, because it is not as robust as the other parts of the algorithm. Unfortunately, there was not enough time to improve this method. Some examples are shown in Figure 35.

Original Images

Reference Image
Mission Image

Denoising
Speckle Filter
Enhanced Frost Filter

Image Subtraction

Reference − Mission -> Diff_1
Mission − Reference -> Diff_2

Optical Flow
Calculate Optical Flow Vectors
Reference Im. -> Mission Im
Mission Im. -> Reference Im

Initial Thresholding
Initial determination of
structures in the original
images

Diff_1   Diff_2

Optical Flow Vectors   Th_Reference   Th_Mission

Difference Thresholding

(Area & Intensity Thresholding)
Threshold Diff 1 & Diff 2

Th_Diff_1

Th_Diff_2

Optical Flow
Use Calculated Flow Vectors to
match regions in thresholded
difference images.

Th_Diff_1_OF

Th_Diff_2_OF

Larger Object Elimination
Remaining objects are checked
whether they are parts of other
objects. Performs OF also.

Th_Diff_1_LOE   Th_Diff_2_LOE

Th_Diff_1

Th_Diff_2

Final Elimination
Put together previous outputs
and check for more false
positives.

Fifth Stage - Find Intensity Changes

Find Intensity Changes

Areas with few objects but with
intensity changes (optional)

Merging

Difference areas that are close
to each other are merged.

Figure 34. Flow diagram fifth stage: find intensity changes.
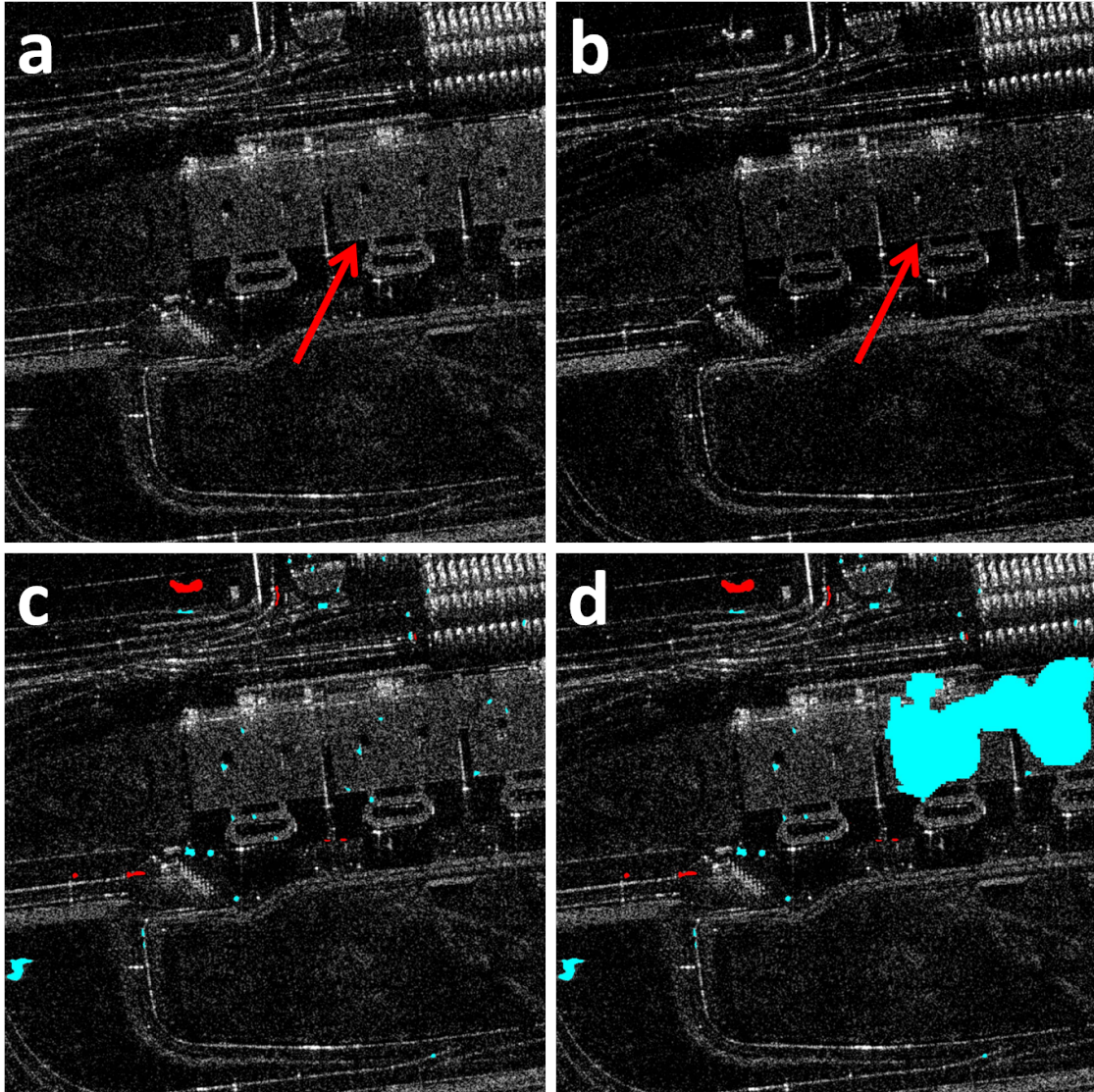
Figure 35. Sample results for the optional fifth stage of the algorithm. a) original reference, b) original mission, c) intensity change detection is off, d) intensity change detection is on. Note that there are no visible objects in the areas shown but there is a visible intensity increase in the area.

4.3.7   Sixth Stage Merging

Figure 36 shows the last stage of the algorithm. All the remaining difference objects are visited by an 11x11 moving window and merged with another object if the window is able to touch both objects simultaneously. 2CMV image comparisons are shown in Figure 37.
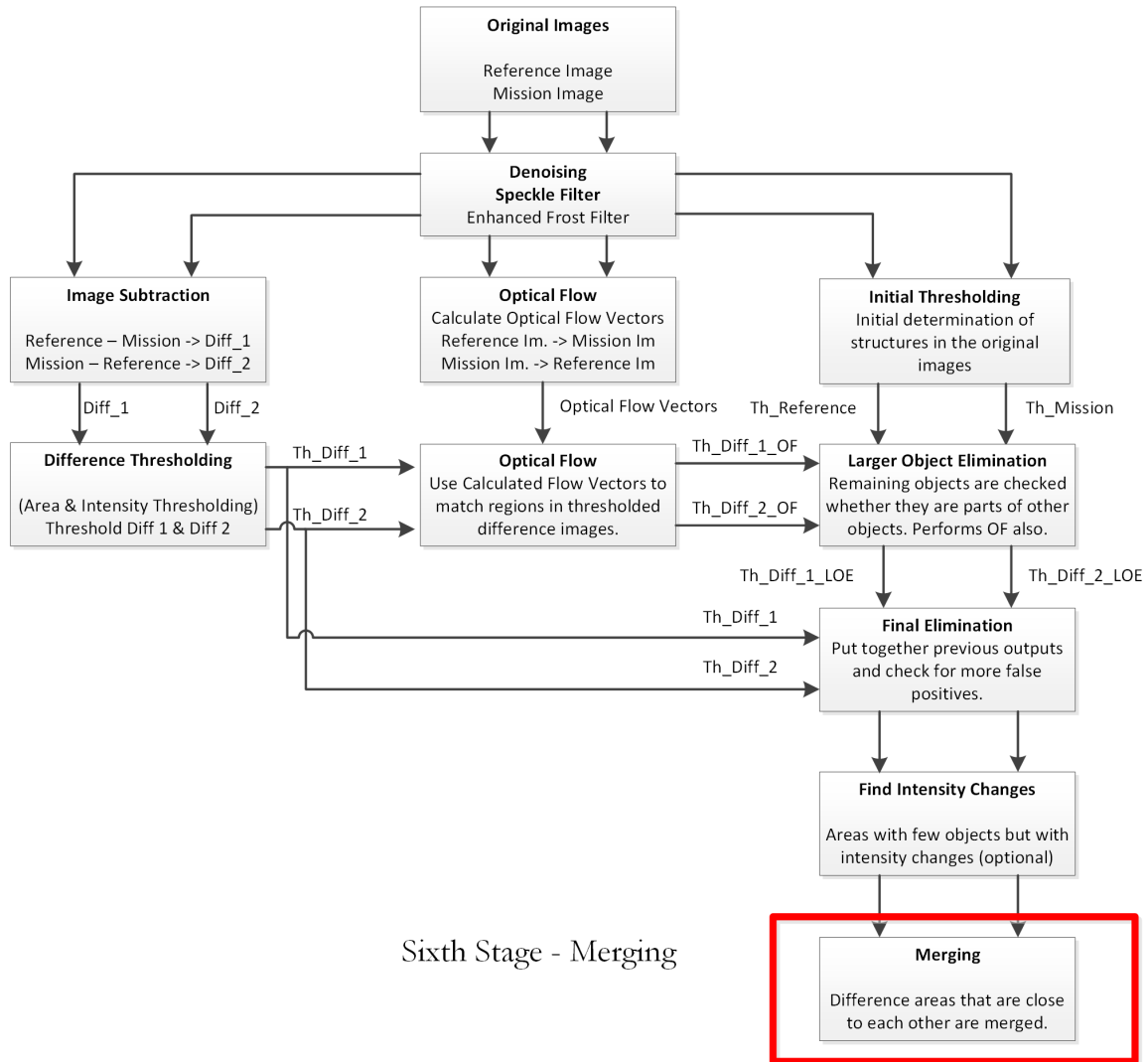
Figure 36. Flow diagram sixth stage: merging.
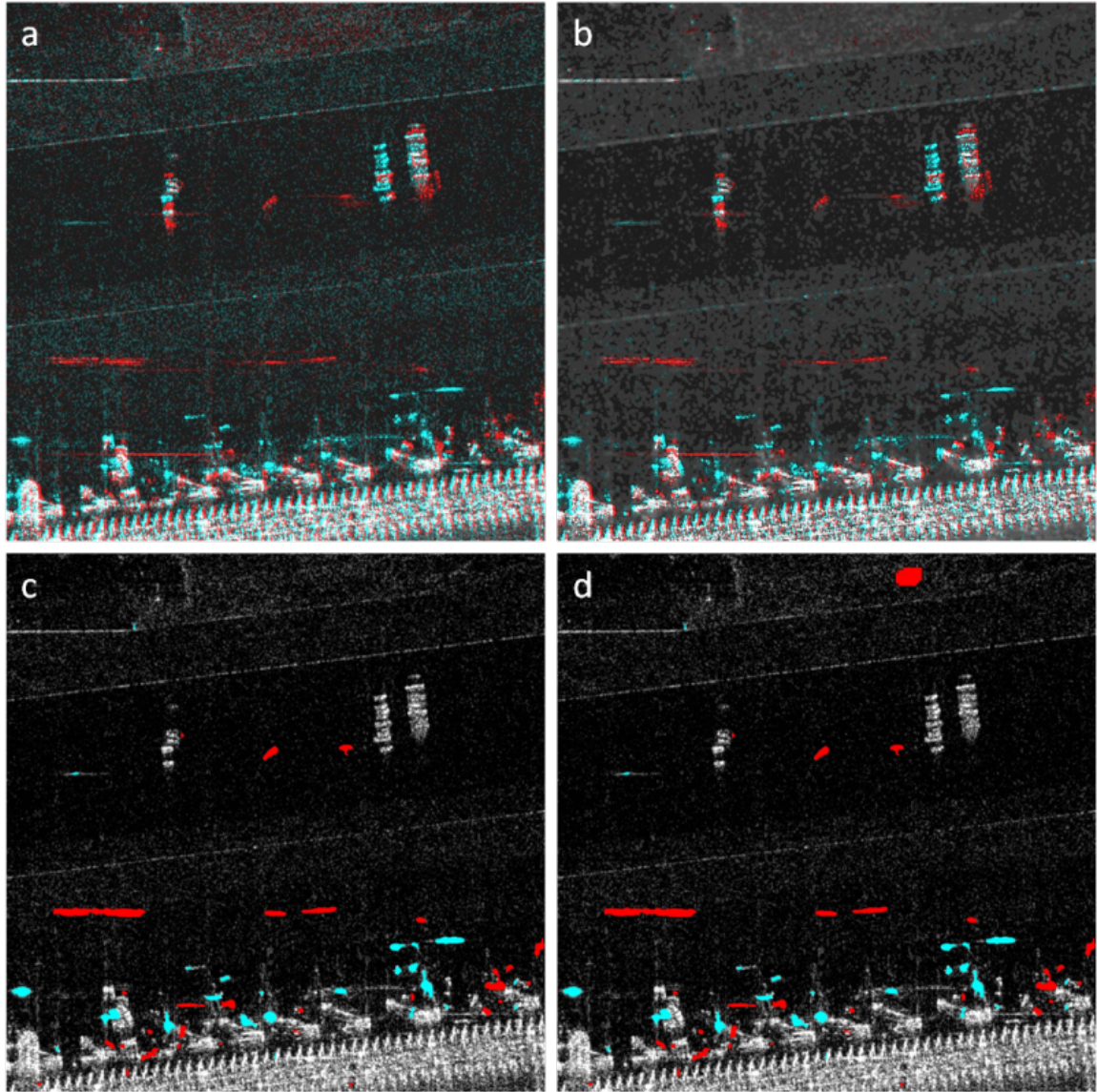
Figure 37. Comparison between original 2CMV and processed 2CMV images.

4.4 Results

Proposed method has been tested with 8 1024x1024 regions from the datasets provided by Lockheed Martin. It has been noted that statistical analysis has been effective for removing false positives that do not match object profiles. Optical flow has been effective for removing difficult false positives that result from registration and perspective problems. In many representative image regions, false positive detections have been reduced by over 50%. Object merging has helped reduce the number of the labeled objects and given a better unified representation of the change in a region. Adaptive thresholds improved the quality of the object extraction and helped identify false positives. Establishing false positive motion/error thresholds, an accord with initial image registration, can be key for continued improvement. In addition to the dataset that was provided for this work, the framework was also tested with a SAR dataset from Sandia National Laboratories. The final results for the Sandia dataset are given in Figures 38 and 39. Even though the computational complexity was not an issue during the course of this work, it should be noted that the speckle filtering, optical flow processing and merging are computationally expensive processes. On a 2.4GHz quad core computer (Intel Q6600 chip) with 8GB of memory, it takes around 5 minutes to process one region. There are many factors that are contributing to this time. Code was written in the MATLAB environment and it is not optimized for performance. MATLAB also does not utilize all the cores, so effectively it uses only a single core most of the time.
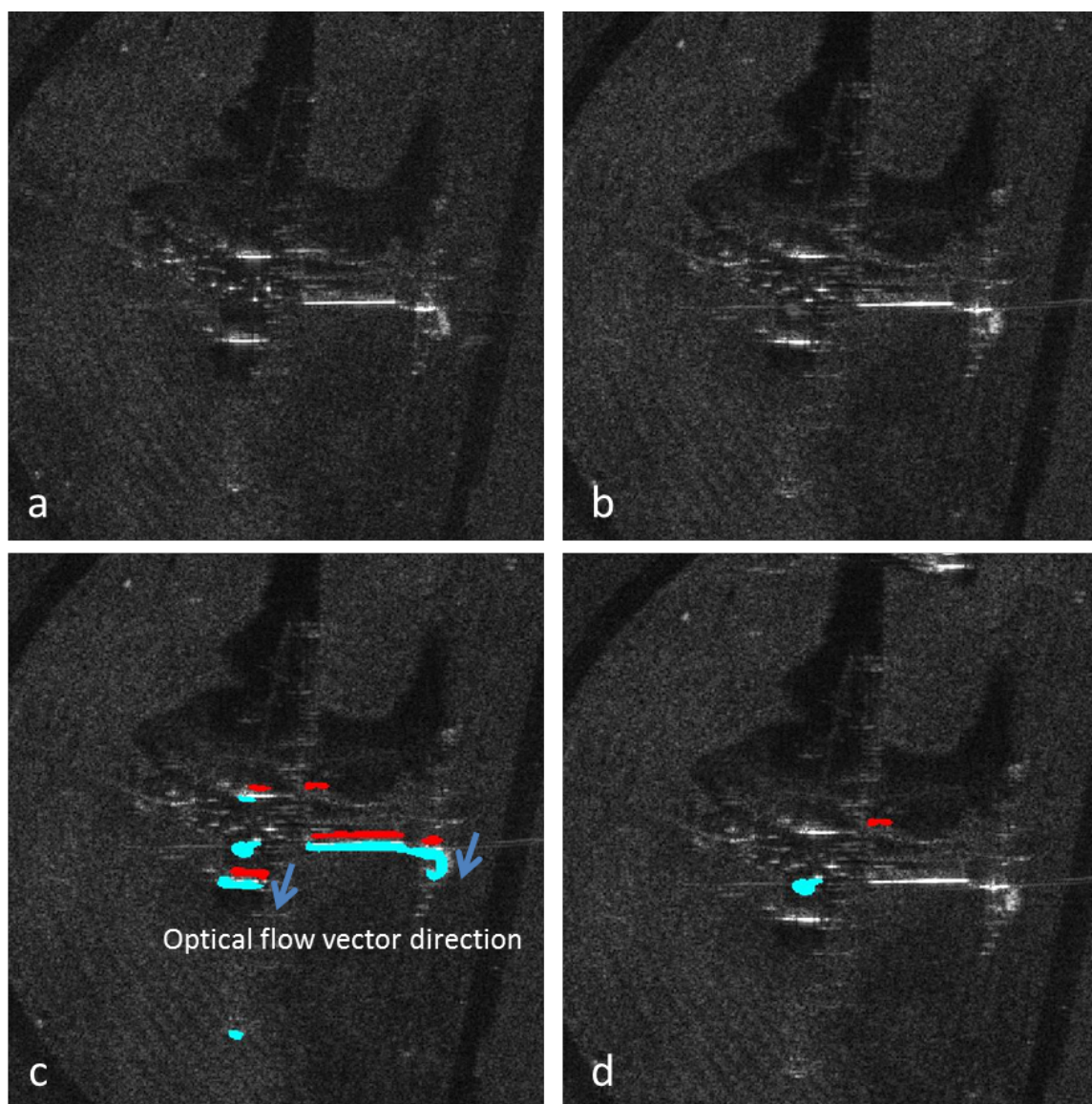
Figure 38. a) Original image 1, b) Original image 2, c) Difference image. Differences occur because the images are not registered. Optical flow vectors show that some of the larger differences are false positives. d) Final difference image. (Courtesy of Sandia National Laboratories)
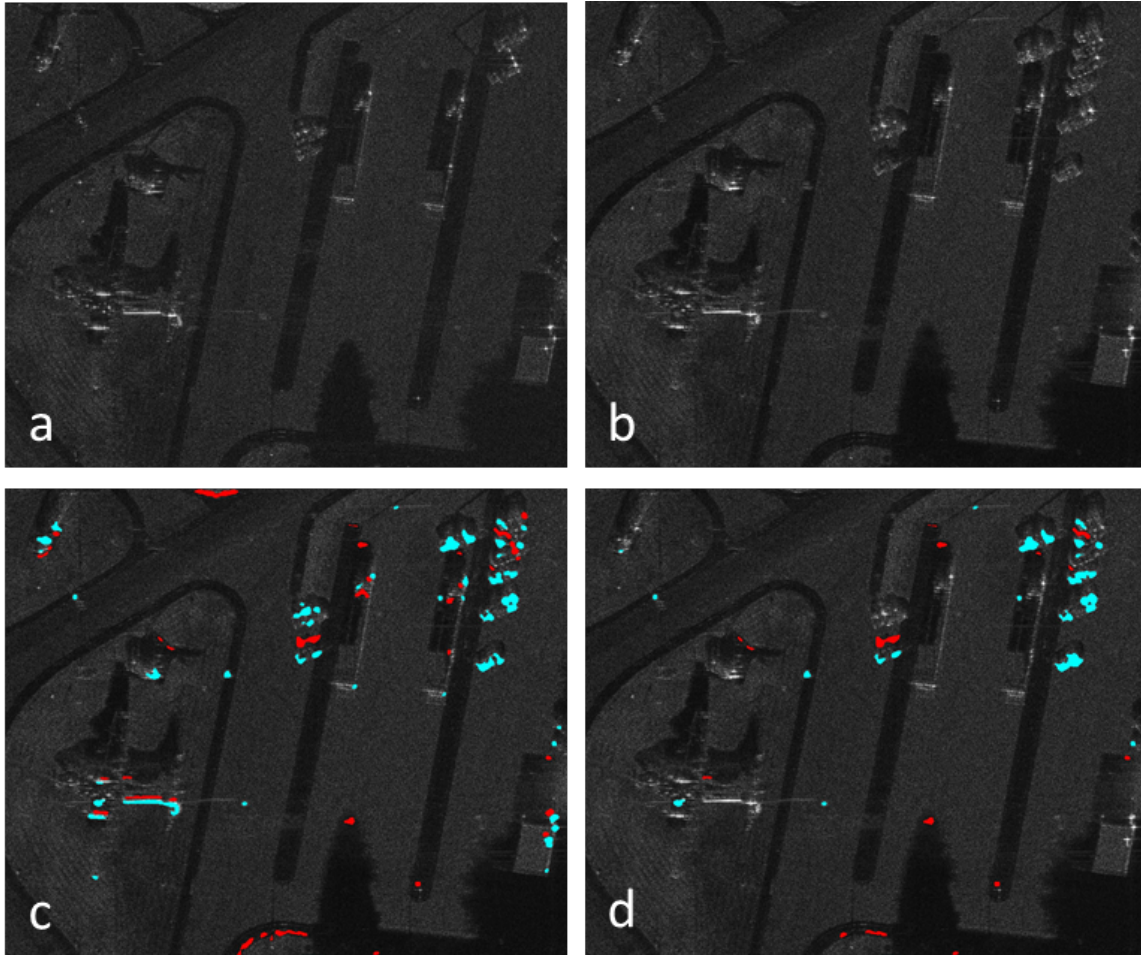
Figure 39. a) Original image 1, b) Original image 2, c) Difference image. Note that there are false positives in the image, d) Final difference image. (Courtesy of Sandia National Laboratories)

4.5   Discussion & Conclusions

Several image processing methods like noise reduction, intensity and area thresholding, and optical flow methods are used to improve object extraction from a SAR AGI product (2CMV imagery). Results demonstrate the ability of the techniques to reduce false positives up to 60% in the tested SAR image pairs. However, there is still room for further improvement. For example, it was noticed that optical flow object matches close to image block borders can be overlooked due to the inaccuracy of flow vectors near the block borders. This problem can be addressed with a multigrid approach that leverages overlapping image blocks. Using this approach, if an object pair is close to the border in one block, then it will be near the center of an overlapping block. Objects that are close to one another can also be merged to provide a more holistic analysis of the scene and further reduce the number of false positive object detections. However, it must be concurrently ensured that false positive reduction is not overly aggressive to the point that false negatives are generated. One obstacle that has hindered the progress thus far is a fundamental unavailability of ground truth, correctly processed 2CMV data to be used in training the algorithms. It is also a challenge to extract only regions with intensity value changes. It is possible that wavelet based methods might be more successful with such a task.

Chapter 5

IMPROVING THE ACCURACY OF TWO-COLOR MULTIVIEW (2CMV) PRODUCTS USING UNSUPERVISED FEATURE LEARNING AND OPTICAL FLOW

This section presents an alternative solution to the problem that was introduced in the preceding section, Chapter 4.

5.1 Introduction

In 2CMV AGI products, the changes between two SAR images are colorized and overlaid on an initial image such that new features are represented in cyan, and features that have disappeared are represented in red. In order to create the change maps, images are cross-correlated pixel-by-pixel to detect the changes. 2CMV products show changes at the pixel level and are dominated with red and cyan colors. Figure 40 shows a portion of a sample 2CMV image. It can be seen that most of the pixels in the 2CMV image are colored either red or cyan even if there is no change in the area. There are inherent problems in change detection in SAR images. These problems are described and a solution is proposed in Chapter 4. This chapter introduces an alternative framework of computer vision methods for the generation of 2CMV products toward extraction of advanced geospatial intelligence. Before false positive and object detection algorithms are performed, speckle and smoothing filters are used to mitigate the effects of speckle noise. Then, the number of false positive detections is reduced by applying: 1) unsupervised feature learning algorithms

and 2) optical flow algorithms that track the motion of objects across time in small regions of interest.

There have been a number of change detection studies using thresholding [Bazi *et al.* (2005); Bovolo and Bruzzone (2005); Moser and Serpico (2006); Sumaiya and Kumari (2016); Kanberoglu and Frakes (2017)], extreme learning machine [Jia *et al.* (2016); Gao *et al.* (2016)], Markov random fields [Melgani and Bazi (2006); Yousif and Ban (2014)] and combinations of feature learning and clustering algorithms [Celik (2009); Li *et al.* (2012); Lu *et al.* (2017); Ghosh *et al.* (2011); Nguyen and Tran (2010); Li *et al.* (2015); Gong *et al.* (2014)]. Optical flow fields can be used to distinguish between objects that have actually moved between frames and those that are in the same location but are slightly misregistered. Both cases of apparent motion can result in 2CMV detection, but they obviously differ greatly in terms of meaning. Investigation of the state-of-the-art in SAR image processing indicates that differentiating between these two general cases is a problem that has not been well addressed. Algorithms that mitigate speckle noise effects well and distinguishing between actual motion and misregistration can lead better change detection. As mentioned in the preceding chapter, there is a lack of published methods for efficient generation of 2CMV products from SAR images, which serves as another motivating factor for this work.

The remainder of this chapter is organized in four sections. Following the introduction, Section 5.2 gives a brief background on the filtering, unsupervised feature learning, and optical flow techniques that were used and describes the stages of the proposed framework. Section 5.4 presents simulation results. Section 5.5 discusses the results and the contributions of the proposed methods.
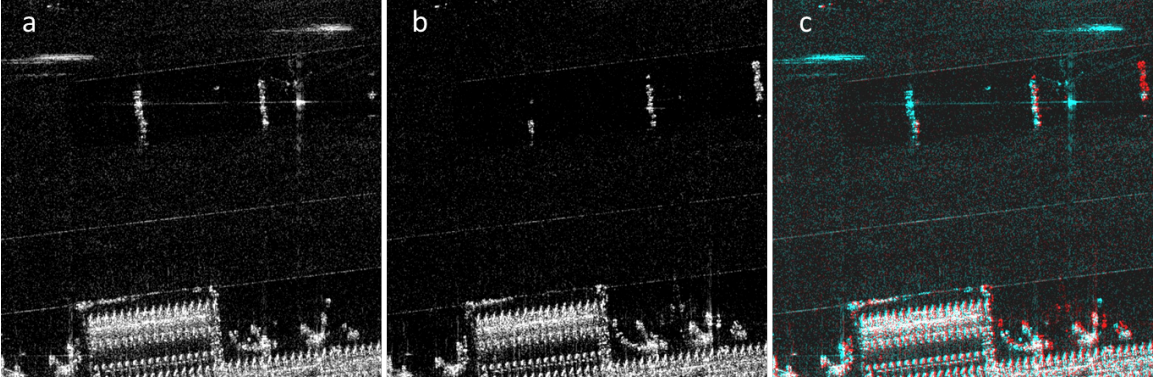
Figure 40. a) Reference image, b) Mission image, c) Two-color multiview (2CMV) image. In all the images, there is an airplane visibly parked next to a building near the bottom center. Note: Reference and Mission images are used as the source of the sample figures and results throughout this chapter.

5.2   Methods

This section provides the background for the key methods that are utilized in the proposed framework for generating change maps and eliminating false positives in those maps that drive the 2CMV representation. Denoising and optical flow techniques are already described in 4.2. This section gives an overview of the unsupervised feature learning techniques that are used in the framework .

5.2.1 k-means Clustering

The k-means clustering algorithm attempts to partition p observations into k clusters such that each observation belongs to the nearest cluster mean (centroid) [Gonzalez and Woods (2006)]. The k-means algorithm iteratively tries to find k centroids for each cluster, while minimizing a within-cluster sum of squares

$$argmin \sum_{i=1}^{k} \sum_{x_j \epsilon S} \|x_j - \mu_j\|^2$$

80

Outline k-means clustering algorithm

---

1. Initialize the centroids: Assign k points as the initial group centroids.
2. Calculate the distance of each point to the centroids and assign the point to the cluster that has the closest centroid.
3. After the assignment of all the points, recalculate the new values of the centroids.
4. Repeat Steps 2 and 3 until the centroid locations converge to a fixed value.

Table 2. Basic steps of the k-means algorithm.

where x_j is the jth observation and μ_j is the mean point (centroid) in the cluster. The basic steps of the algorithm are given in Table 2.

5.2.2   K-SVD

K-SVD is a dictionary learning algorithm that is used for training overcomplete dictionaries for sparse representations of signals [Aharon *et al.* (2006); Rubinstein *et al.* (2008)]. It is an iterative method that is as a generalization of the k-means clustering algorithm. The K-SVD algorithm alternates between two stages: 1) sparse coding stage, and 2) dictionary update stage. In the first stage, a pursuit algorithm is used to sparsely code the input data based on the current dictionary. Based on Rubinstein *et al.* (2008), the Batch Orthogonal Matching Pursuit (Batch-OMP) algorithm can be used in this step. In the second stage, the dictionary atoms are updated to better fit the data via a singular value decomposition (SVD) approach. The basic steps of the K-SVD algorithm are given in Table 3.

Outline K-SVD algorithm

Task: Find the best dictionary to represent the data samples $\{y_i\}_{i=1}^N$, $y_i \epsilon R^N$ as sparse compositions by solving:

$$min_{D,X}\{\|Y - DX\|_F^2\} \ \ \text{subject to} \ \forall_i, \|x_i\|_0 \leq T_0.$$

Initialization: Set the dictionary matrix $D^{(0)} \ \epsilon \ R^{n \times K}$ with l^2 normalized columns. Set $J = 1$.

Iterations: Repeat until convergence:

- Sparse coding stage: Use any pursuit algorithm to compute the representation vectors x_i for each sample y_i by approximating the solution of

$$i = 1, 2, ..., N, \quad min_{x_i}\{\|y_i - Dx_i\|_2^2\} \ \ \text{subject to} \ \|x_i\|_0 \leq T_0.$$

- Dictionary update stage: For each column $k = 1, 2, ..., K$ in D^{J-1},
    - Define the group of samples that use this atom,

    $$w_k = \{i \ |1 \leq i \leq N, x_T^k(i) \neq 0\}$$

    - Compute the overall representation error matrix, E_k, by

    $$E_k = Y - \sum_{j \neq k} d_j x_T^j$$

    - Restrict E_k by choosing only the columns corresponding to w_k, and obtain E_k^R.
    - Apply SVD decomposition $E_k^R = U \Delta V^T$. Choose the updated dictionary column $\widetilde{d}_k$ to be the first column of U. Update the coefficient vector x_R^k to be the first column of V multiplied by $\Delta(1, 1)$.

- Set $J = J + 1$.

Table 3. Steps of the K-SVD algorithm

5.3 Image Processing Steps

In this section, we describe the image processing approach for extracting change maps. The inputs are two registered SAR images of the same field of view that were taken at different times, i.e. "reference" image and "mission" image. Due to the large size of the images, images were divided into subimages for processing.

In the denoising step, an Enhanced Frost filter, as described in Sec. 4.2.4.1, with a 5x5 window size was first used to mitigate the speckle noise effects. Then, a 9x9 low pass filter was used to smooth the test areas in order to obtain more uniform flow fields in the optical flow processing step. The remaining steps are grouped in three stages and described in the following subsections. The detailed flow diagram shown in Figure 41 can be used as a guide for the following descriptions.

STAGE 1

Differrence Image
|Reference − Mission | = Diff_Im

Training Data
Divide the image into hxh non-overlapping blocks

Dictionary Generation
Use the blocks as training data to generate K-SVD dictionary.

Create Feature Space
Use OMP algorithm to find the approximated projections of data onto the K-SVD dictionary.

Clustering
Use k-means clustering algorithm to divide the feature space into two clusters (Change and No-Change)

Change Maps
Generate two separate change maps based on
Reference − Mission -> CM_1
Mission − Reference -> CM_2

Reference Image
Mission Image

Denoising
Speckle and smoothing filters

STAGE 2

Optical Flow
Calculate Optical Flow Vectors
Reference -> Mission
Mission -> Reference

Optical Flow Vectors

Optical Flow
Use Calculated Flow Vectors to match regions in Change Maps.

STAGE 3

Initial Thresholding
Initial determination of structures in the original images

Larger Object Elimination
Remaining objects are checked whether they are parts of other objects.

Final Elimination
Difference areas that are close to each other are merged.

Figure 41. Flow diagram of the proposed framework.

84

5.3.1　First stage: Generation of change maps using unsupervised feature learning

Two change maps are needed for a 2CMV representation of a SAR image pair. Each change map represents the changes that exist in the corresponding SAR image. In this stage, we generate a combined change map and separate it into two change maps. In order to generate the combined change map, we used an approach similar to that was used in Celik (2009). In the original approach, an eigenvector space is created by performing principle component analysis (PCA) on the difference image and k-means algorithm classifies the projections onto the eigenvector space into two classes, e.g. change and no-change. The basic steps are given in Table 4. It should be noted that in our framework, PCA was replaced with K-SVD because one can adjust the dictionary size and the sparsity constraint to obtain change maps with different levels of details. Figure 42 shows two change map results with different dictionary sizes.

After the change maps are generated, object properties such as area and location are calculated and based on a user-defined area threshold, insignificant change areas are excluded from the change maps. The remaining change areas are then overlaid onto the reference image. In the 2CMV image, the areas that exist only in the reference image are colored in cyan and the areas that exist only in the mission image are colored in red. A sample 2CMV image after this stage is shown in Figure 43. In Kanberoglu and Frakes (2017) and in Chapter 4, this stage is replaced by adaptive thresholding.

Table 4. Steps of the proposed method for generating change maps.

Outline

---

1. **Difference Image:**

$$X_{dif} = |Reference - Mission|$$

2. **Training Data:** Divide X_{dif} into hxh non-overlapping blocks.
3. **Dictionary Generation:** Use the K-SVD algorithm to generate an overcomplete dictionary.
4. **Create Feature Space:**
   - Generate hxh blocks for each pixel in X_{dif} where the pixel is in the center of the block.
   - Use OMP algorithm to generate the projections of the data onto the dictionary.
5. **Clustering:** Use the k-means algorithm to classify the feature space into two classes, e.g. change and no-change.
6. **Change maps:** Use the two classes to generate the combined change map. Divide the combined change map into two separate change maps based on the changes that occur in the images.
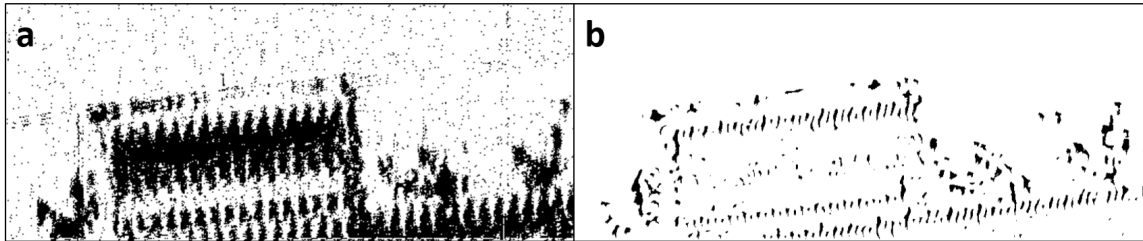
Figure 42. a) Change map with dictionary size = 30 atoms with 30 non-zero coefficients, b) Change map with dictionary size = 15 with 3 non-zero coefficients. Note that a larger dictionary size with more non-zero coefficients captures more changes.
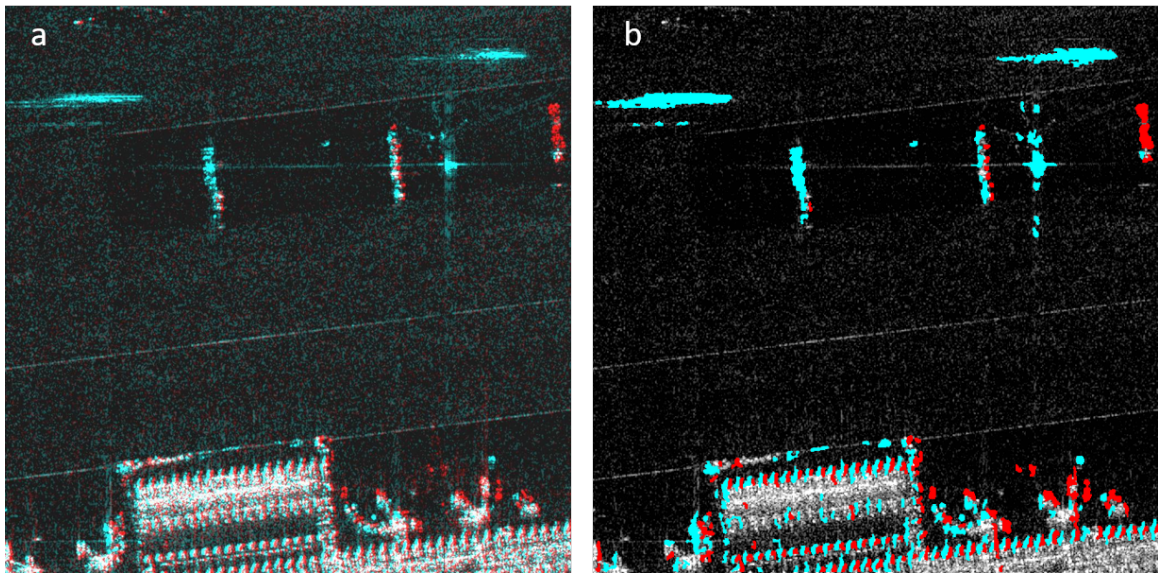
Figure 43. a) Original 2CMV image, b) 2CMV image after Stage 1. Note that there are several false positives around the ridges of the building. In the second image, change colors (red and cyan) were made more pronounced to highlight the false positives.

5.3.2 Second stage: Optical flow

Figure 43 displays a 2CMV image after the first stage wherein it is clear that additional processing is needed to improve results because the ridges of the building in both images are slightly misregistered and they are shown as changes in both images. The primary improvement that is targeted with additional processing is reducing the number of false positives in the image. This goal can be accomplished with the use of the optical flow (OF) method described in Sec. 4.2.1. To manage computational complexity, the optical flow algorithm is performed on 256x256 pixel image blocks. Note that optical flow is calculated based on the original reference and mission images.

After obtaining the flow vectors, the direction of the majority of flow vectors is determined. The flow vectors that are in this direction are applied to the two first stage change maps to find matches. In the reference image, OF vectors are used to move the detected change areas in the flow direction. The destination of an area is then compared with the same location in the mission image. If there is a matching area based on location and size, then the two change areas are excluded from the change maps. The same process is performed in the opposite direction to match mission image change areas in the reference image. Figure 44 illustrates this step.
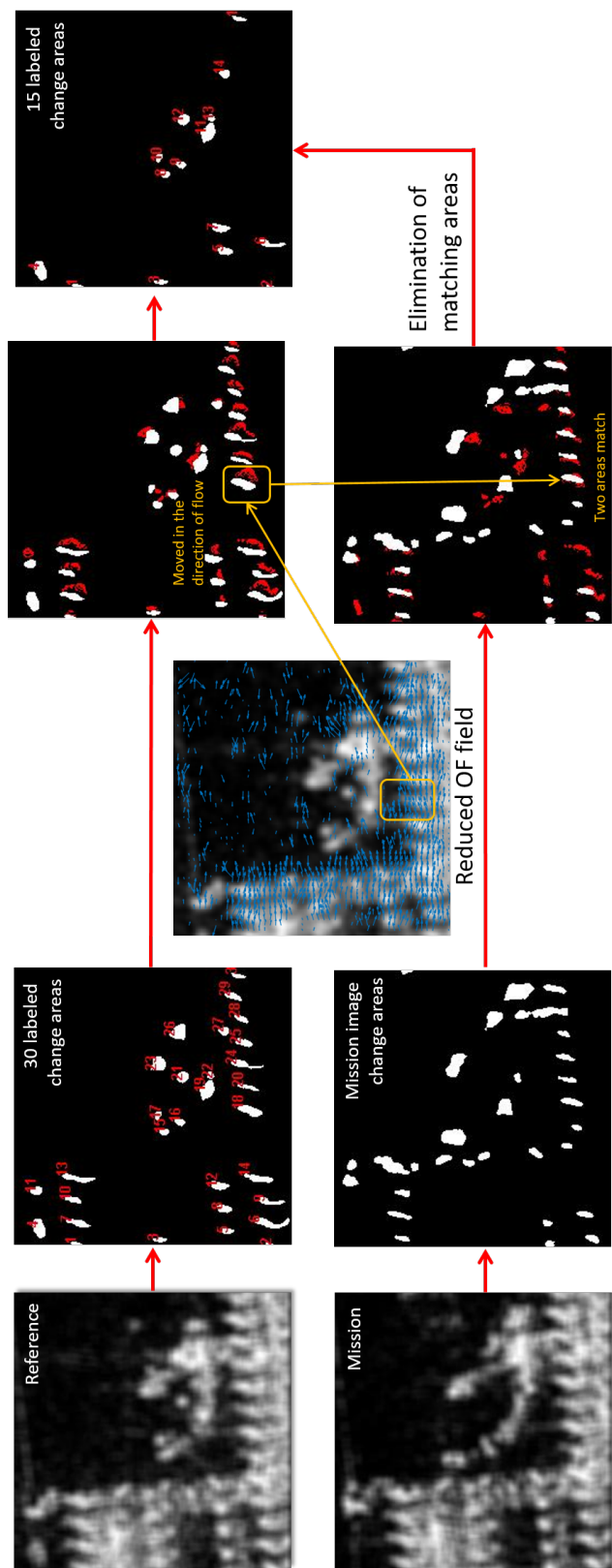
Figure 44. Elimination of false positives using OF. Change areas are moved along the flow direction in the reference image change map. Moved areas (shown in red) from the reference image are overlaid onto the mission image change map. The overlapped areas are then removed.

5.3.3 Third stage: OF assisted object extraction

This stage has two main parts: extraction and elimination. Extraction is performed by an adaptive thresholding method that is similar to the one used in Kanberoglu and Frakes (2017). In this stage, the thresholding is performed on the original images to extract/label objects. The resulting two thresholded images are processed in two ways. First OF vectors are used on the images to match the objects. The main difference from the second stage is that the flow vectors are used on the original thresholded images, not on the change maps. Change maps do not necessarily contain objects, and the goal is to find objects that moved between the two images. Objects with possibility of movement are labeled and compared against the areas in the change maps. It should also be noted that only some parts of an object can be detected as a change, and these detected changes can be used as a guide to extract the full object.

After this process, the labeled areas in the change maps are overlaid on the reference image and checked whether they are a part of a larger object in the image. If the labeled area is found to be a part of a larger object, then the same location in the mission image is checked for the same object. In the case of two similar objects around the same location, it can be assumed that the detected object is a false negative and excluded from the difference map. After these two methods are performed, the output of this stage is generated by simply taking the intersection of the two results. Figure 45 shows how this process converts the reference image in a) to the final output in e).
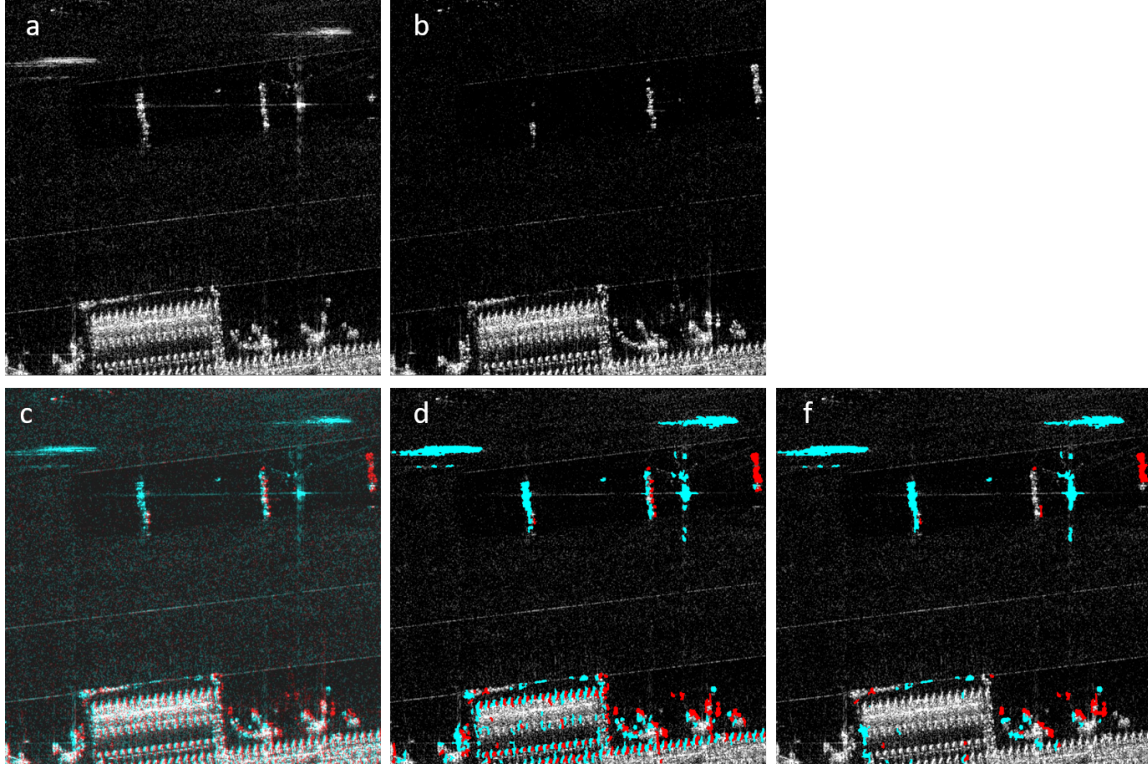
Figure 45. a) Reference image, b) Mission image, c) Original 2CMV image, d) 2CMV image after using dictionary learning and clustering (Stage 1), e) Final 2CMV image. False positives are reduced.

5.4   Results

In addition to the final results shown in Figure 45, proposed framework was tested with eight 1024x1024 regions from a SAR image pair provided by Lockheed Martin. It was noted that unsupervised dictionary learning and clustering algorithms were effective at removing false positives that did not match object profiles. Optical flow was effective for removing difficult false positives that resulted from registration and perspective problems. In many representative image regions where registration errors are prevalent, false positive detections have been reduced. The results are consistent with the results in Chapter 4.
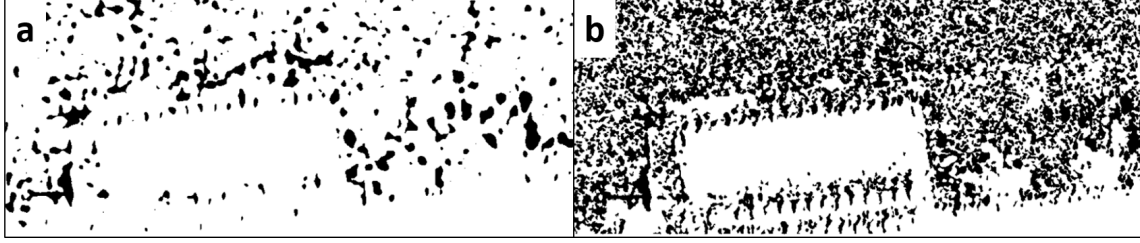
Figure 46. a) GaborTLC change map , b) NR-ELM change map.

Even though the computational complexity was not an issue during the course of this work, it should be noted that the speckle filtering, optical flow processing and merging are computationally expensive processes. On a dual core computer (Intel Core i7 6500U) with 16GB of memory, it takes about 2.5 minutes to process one region. There are many factors that are contributing to this time. Code was written in the MATLAB environment and it is not optimized for performance.

It should be noted that the methods proposed in [Li *et al.* (2015); Gao *et al.* (2016)], GaborTLC and NR-ELM respectively, were also tested on the dataset as possible alternatives to the K-SVD method. Both methods heavily detected intensity changes in the terrain pixels along with the object changes in the images; however, when several of these intensity changes are close to the objects that should be highlighted in the 2CMV image, the effectiveness of the optical flow step would be hindered. Even though these methods were effective in detecting changes, for the purposes of this paper, they were not chosen to be incorporated in the proposed framework. It is possible to utilize these methods in the framework with different preprocessing/filtering steps. Figure 46 shows the change maps of the two methods where the structures are not well defined in the change maps.

5.5   Discussion & Conclusions

It was shown that unsupervised feature learning algorithms can be effectively used in conjunction with optical flow methods to generate 2CMV AGI products. Other image processing methods like noise reduction and adaptive thresholding are used to improve object extraction in the proposed methodology. Results demonstrate the ability of the techniques to reduce false positives up to 60% in the tested SAR image pairs. More recent optical flow or motion estimation algorithms can be investigated as an alternative to the one utilized in this work. It should be noted that the chosen optical flow method is suitable for the tested dataset and performs adequately as expected since it takes into account the intensity changes between images. The choice of K-SVD over PCA increased the computational complexity while allowing flexibility over the details of the change maps by changing the dictionary size and the number of non-zero coefficients. Dictionaries with higher number of non-zero coefficients provided more detailed change maps. Two other methods were investigated as an alternative to the K-SVD method. It was seen that they also detected changes in the intensity of the terrain pixels. This was counter productive when the goal was mainly detecting the changes around the objects and generate 2CMV images emphasizing these changes. Additional pre-processing methods can be explored to work around this drawback.

Chapter 6

INTEGRATION OF 3D ^{1}H-MAGNETIC RESONANCE SPECTROSCOPY
DATA INTO NEURONAVIGATION SYSTEMS FOR TUMOR BIOPSIES

6.1   Introduction

Many important applications in clinical medicine can benefit from the fusion of
spectroscopy data with anatomical imagery. For example, the correlation of metabo-
lite profiles with specific regions of interest in anatomical tumor images can be useful
in characterizing and treating heterogeneous tumors that appear structurally homo-
geneous. Such applications can build on the correlation of data from *in vivo* Proton
Magnetic Resonance Spectroscopy Imaging (^{1}H-MRSI) with data from genetic and *ex
vivo* Nuclear Magnetic Resonance spectroscopy. To establish that correlation, tissue
samples must be neurosurgically extracted from specifically identified locations with
high accuracy. A clinical workflow and neuronavigation purposed custom software
tool complete with unique image and data processing capabilities and a graphical
user interface were developed to integrate three-dimensional (3D) ^{1}H-MRSI data
into industry standard image-guided neuronavigation systems. MRSI spectra were
processed and analyzed, and specific voxels were selected based on their chemical
contents. 3D neuronavigation overlays were then generated and applied to anatomi-
cal image data in the operating room. The proposed methods improve upon the cur-
rent state-of-the-art in neuronavigation through the use of detailed three-dimensional
^{1}H-MRSI data.

Without such technology, neurosurgeons must rely on limited two-dimensional neu-

ronavigation or on memory and other qualitative resources alone for guidance in accessing specific MRSI-identified voxels. The newly proposed 3D methods also fully account for scanner calibration and leverage tools that are now publicly available. The result is a progressive form of online MRSI-guided neuronavigation that is demonstrated in this study through phantom validation and clinical application. Toward that end, this chapter presents new neuronavigation technology that enhances current clinical capabilities in the context of neurosurgical planning and execution. 3D MRSI spectra are processed and analyzed, and specific voxels are selected based on their chemical contents. 3D neuronavigation overlays are then generated and applied to anatomical image data in the operating room. In contrast, 3D MRSI-based overlays provide comprehensive, quantitative visual cues and location information during neurosurgery.

The remainder of this chapter is organized in four sections. This section gives a brief background and a summary of related previous work. Section 6.2 describes the methods, tools, and systems that were vital to the study. Section 6.3 presents phantom study and clinical results. Section 6.5 discusses the results and the contributions of the proposed methods.

6.1.1 Background

Biopsy plays a key role in the histopathological diagnosis of tumors. The primary function of biopsy in that role is to extract tissue samples from specific tumor locations with high accuracy. However, identifying and accessing the most important locations for sampling can be challenging since anatomical Magnetic Resonance Imaging (MRI) data provide a limited description of tumor properties. Non-invasive

Proton Magnetic Resonance Spectroscopy Imaging (^{1}H-MRSI), also known as Chemical Shift Imaging (CSI), can provide valuable guidance in this regard. Specifically, ^{1}H-MRSI can be used to quantify the chemical contents of voxels in an image, and the origin of extracted tissue can then be validated based on chemical profile. Note that previous work provides support for using three-dimensional (3D) spectroscopy data in this process [McKnight *et al.* (2002); Kanberoglu *et al.* (2010)].

6.1.2   Summary of Related Previous Work in Tumor Spectroscopy

A number of previous studies have applied Nuclear Magnetic Resonance (NMR) spectroscopy to examine *ex-vivo* samples from meningiomas. For example, several studies have shown that the aggressiveness of a meningioma can be determined based on its spectral profile [Pfisterer *et al.* (2007, 2010)]. Other studies have leveraged ^{1}H-MRSI to distinguish effectively among different types and/or grades of *in vivo* brain tumors based on their characteristic biochemical markers [Pfisterer *et al.* (2007, 2010); Majos *et al.* (2003); Preul *et al.* (1996, 1998); Sibtain *et al.* (2007)]. More recently, several studies have demonstrated the use of spectroscopic information to help guide brain tumor biopsies and neurosurgeries [Stadlbauer *et al.* (2004b); Chernov *et al.* (2009); Stadlbauer *et al.* (2004a); Hermann *et al.* (2008); Ng and Lim (2008); Son *et al.* (2001)]. Of particular interest are Ganslandt *et al.* (2005), where two-dimensional (2D) ^{1}H-MRSI was used to better delineate glioma infiltration zones, and Frati *et al.* (2011), where 2D spectroscopy data were used in grading gliomas for a large number of patients. However, the authors of Frati *et al.* (2011) specifically noted the difficult challenge of positioning the 2D spectroscopy grid optimally, and further methodological advancement was motivated in a subsequent note [Chernov *et al.* (2012)]. In

a related study, our group has proposed that 3D ^{1}H-MRSI may permit *in vivo* grading of the meningioma subset of intracranial tumors through the examination of spectra from specifically identified tumor voxels [Moore (2011)].

6.2   Materials & Methods

6.2.1   Scanner Calibration

Effective MRI-based neuronavigation requires high quality image data. Unfortunately, images that are obtained from the MR scanner can suffer from various distortions. Because of static magnetic and applied gradient field inhomogeneities, there may be warping effects in acquired images. There may also be intensity imperfections due to eddy currents. To mitigate these distortions, the MR scanner should be calibrated so as to produce images with accurate spatial positioning and intensity information. Typical procedures make use of phantoms on the order of 10cm to calibrate scanner gradients, which leaves regions beyond the span of the phantom subject to gradient non-linearities. This shortcoming becomes important when imaging is to cover a larger field of view, to span the human brain for example.

Prior to each MRI examination in this study, a special methodology to calibrate the scanner [Kanberoglu *et al.* (2009)] was used for accurate anatomical image acquisition (thereby ensuring accurate localization to follow). The methodology is based on work from the Alzheimer's Disease Neuroimaging Initiative (ADNI) [Jr *et al.* (2008)] and uses freely available correction and analysis software to calibrate the scanner for geometric accuracy prior to scanning [Jovicich *et al.* (2006); Jovicich and Czanner (2005); Sled *et al.* (1998); Sled (1998a,b); ADNI-Aqual2 (2018)]. Use of the
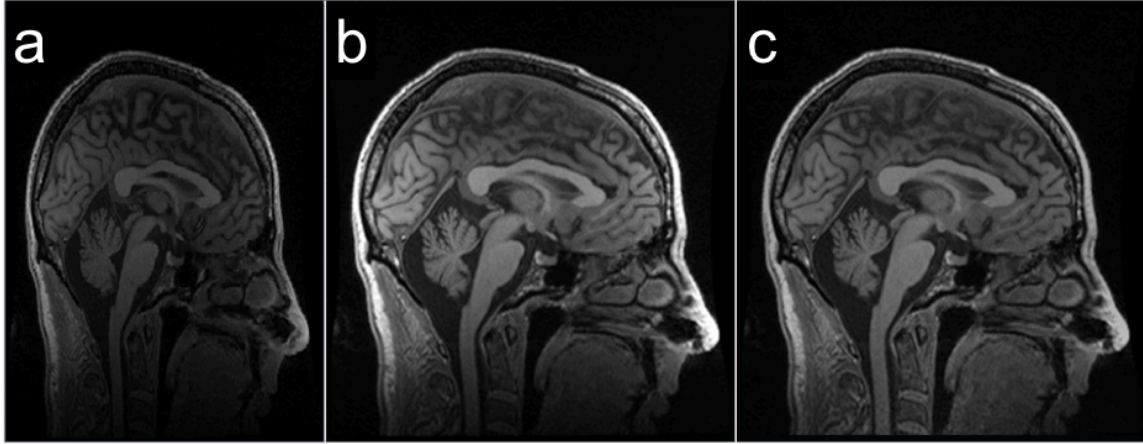
Figure 47. Results of scanner calibration including an originally acquired image (a), the image after correcting warping effects (b), and the image after correcting warping effects and intensity imperfections (c).

ADNI-based methodology calibrates scanner gradients over a much larger field of view (approximately 25cm) than standard approaches. The result is better average non-linearity over a field of view on the order of the human brain. Figure 47 shows images before and after the calibration procedure that demonstrate typical benefits of the process.

6.2.2   3D ^{1}H-MRSI and MRI Data Acquisition

3D ^{1}H-MRSI and MRI data were acquired with a 3T long-bore GE Signa scanner (General Electric Healthcare, Waukesha, WI, USA). First, an axial T1-weighted spoiled gradient recalled (SPGR) pulse sequence (TE: 2.8ms, TR: 6.7ms, slice thickness: 2mm, matrix size: 320x224, FOV: 26x26mm, flip angle: 13°) was used to acquire 3D anatomical data with gadolinium enhancement. Those data were then used as a guide for specifying the MRSI ROI, and high-order shimming was performed to obtain better magnetic field homogeneity in that region. For the MRSI scan, a

point-resolved spectroscopy (PRESS) 3D CSI sequence, GE Probe-P, was used (TE: 144ms, TR: 2000ms, slice thickness: 7mm, matrix size: 8x8, FOV: 7x7mm). All acquired frequency domain (k-space) data were transformed into the spatial domain using a standard Inverse Fourier Transform.

6.2.3   MRSI Biopsy Guidance Tool (MRSI-BGT)

A custom MATLAB (Mathworks, Natick, MA, USA) software tool and graphical user interface, the MRSI Biopsy Guidance Tool (MRSI-BGT), was developed on site to automatically combine 3D metabolite information with anatomical MRI data through overlays as shown in Figure 48. In Figure 48, the overall application workflow (culminating with overlay visualization in Stealth IGS) is illustrated in the top row of images, and the functional flow of MRSI-BGT is inlaid below. MRSI-BGT is publicly available at: *http://ipalab.asu.edu/MRSI-BGT*.

MRSI-BGT uses several different file types to generate the desired overlays. First, 3D anatomical MRI data are read and their header files are parsed. Since the anatomical MRI and MRSI scans have different spatial characteristics, it can be non-trivial to overlay the 3D spectroscopy grid onto the anatomical images. The spectroscopy grid information is stored on the scanner in raw data files (proprietary P-files in a GE system). MRSI-BGT extracts the grid location information from the P-files and also selects voxels of interest based on physician selected criteria (e.g., voxels with the highest metabolite concentrations). MRSI-BGT then uses location and selection information to create a spectroscopy grid to be overlaid onto anatomical images. Information from the anatomical MRI data header is examined next in order to automatically determine the appropriate anatomical image upon which to overlay the spec-

99

Figure 48. Flow diagrams of the overall application workflow (top row) and MRSI-BGT software functions (bottom inlay).

troscopy grid. After the grid is registered with the anatomical image data (any number of registration algorithms can be used, see Zitova and Flusser (2003)), LCModel [Provencher (1993)] is used to quantify metabolite peaks based on ^{1}H-MRSI data.

MRSI-BGT then uses LCModel metabolite concentration tables (i.e., text files containing relative concentrations of the metabolites) to create voxel-specific metabolite concentration heat maps for overlay onto the anatomical data. The 3D concentration values are stored natively in an array and, after the bicubic interpolation method [Keys (1981)] is performed on the array in MATLAB, the resulting interpolated values are overlaid onto the anatomical image data as a semi-transparent heat map for visualization in neuronavigation systems.

It is noteworthy that MRSI-BGT can also be used to manually select voxels for overlay. DICOM format overlays are then created that display 3D blobs at locations corresponding to the manually selected voxels. Since the underlying gray scale voxels offer sufficient dynamic range for effective mapping to other color maps, the 3D blobs can be illuminated during an operation with different ROI-specific colors as desired.

6.2.4 Phantom Validation

Before using the proposed methods and tools for actual biopsy, a phantom validation study were performed to ensure that the MRSI-BGT overlays were generated correctly. Eight specific voxels were selected from a 3D anatomical MRI data set describing a phantom, and measurements of distances between the voxels and intra-image landmarks (taken using the original images) were recorded in MRSI-BGT. 3D overlays highlighting the eight voxels were generated and voxel positions within the overlays were validated against ground truth (the voxel positions in the original images) by comparing the distances measured in MRSI-BGT to equivalent measurements taken in Stealth IGS. Several examples of the validation distance measure-
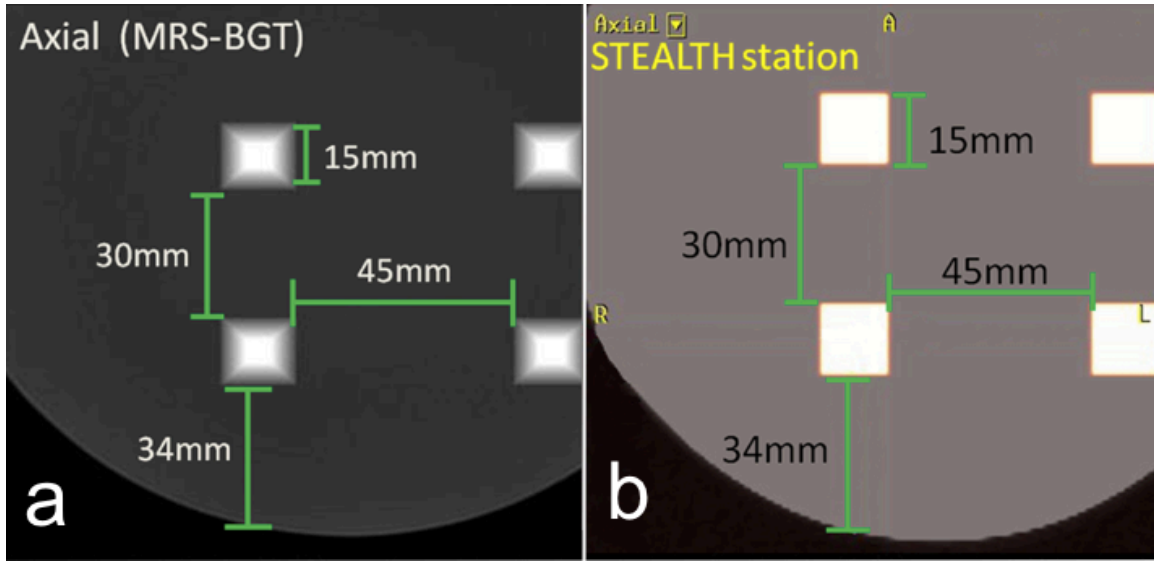
Figure 49. MRSI-BGT (a) and Stealth IGS (b) distance measurement comparisons in two of three dimensions. Note that the measurements indicated in the figure are graphical representations of the actual measurements and do not represent the actual measurements exactly.

ments are shown in two of three dimensions in Figure 49. Note that the Stealth IGS overlays, which were newly generated as a product of this work, were based on information read from both 3D MRSI data headers and anatomical MRI data headers. Specifically, the location of the spectroscopy grid was obtained from the 3D MRSI header and voxel dimensions were obtained from the anatomical MRI header.

6.2.5 Clinical Application: Meningioma Biopsy

After phantom studies, the proposed methods were used in a meningioma study at the Barrow Neurological Institute of St. Joseph's Hospital and Medical Center. Specifically, the methods were used to prospectively target tumor voxels for the first time based on subtle differences in the concentrations of metabolites uniquely linked

to meningioma heterogeneity and outcome. Meningiomas are especially heterogeneous in nature and are globally characterized by a high alanine peak that differentiates them from other intracranial neoplasms [Pfisterer *et al.* (2007, 2010); Preul *et al.* (1996, 1998)]. To serve the goals of the study, it was important to obtain biopsy specimens from specific meningioma regions with high and low concentrations of alanine (and other metabolites, choline for example). Further, because of the heterogeneous nature of meningiomas, biopsy accuracy was especially critical. Twenty-seven patients demonstrating meningioma were selected for a preoperative 3D ^{1}H-MRSI scan by neurosurgeons. Of those patients, 15 had meningiomas with usable spectra and tissue samples collected. Of the remaining 12 patients, three did not have meningiomas, two were claustrophobic and would not enter the MRI scanner, one moved during the scan, two did not undergo surgery, and four did not have usable spectra due to problems with water suppression or difficulties with 3D ^{1}H-MRSI ROI placement.

The 3T GE Signa scanner was calibrated for each of the 15 suitable meningioma patients and high-order shimming was performed to optimize data acquisition in the area of the tumor. Spectroscopy data were acquired using the 3D CSI Probe-P sequence. Functool software (General Electric Healthcare, Waukesha, WI, USA) was used to verify spectral quality immediately after scanning. Due to the limited processing capabilities of Functool, 3D ^{1}H-MRSI data files were processed offline using GE SAGE software V7 (General Electric Healthcare, Waukesha, WI, USA). LCModel was then used to quantify metabolite peaks based on the processed 3D ^{1}H-MRSI data. Note that processing 3D ^{1}H-MRSI data requires the GE SAGE/LCModel interface presented in McLean *et al.* (2000). Next, ROI selection and 3D ^{1}H-MRSI overlay creation for Stealth IGS were executed automatically by MRSI-BGT based

103
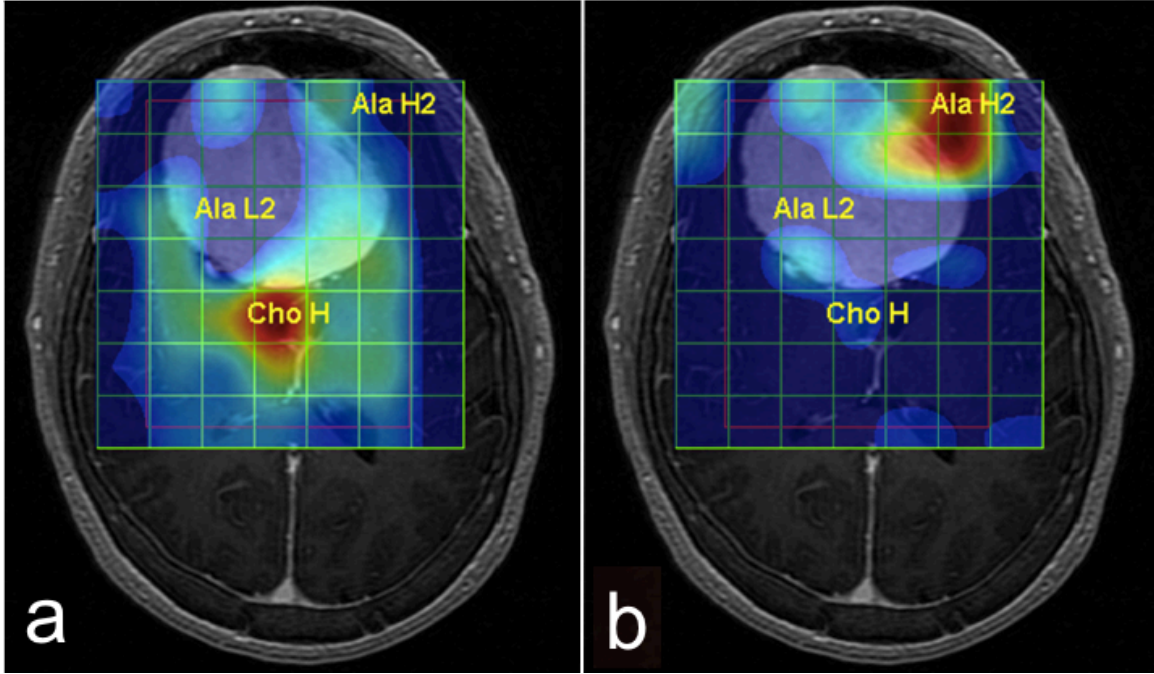
Figure 50. Snapshots of choline (a) and alanine (b) metabolite heat maps overlaid onto anatomical MRI data. Selected voxels are labeled based on their metabolite concentrations ranging from lowest (blue) to highest (red) according to a standard jet colormap. Highest and second highest values are labeled H and H2, respectively, while lowest (not shown) and second lowest values are labeled L and L2, respectively. Note that not all labels appear in each heat map since not all highest and lowest metabolite values for the entire volumetric data set were found in the displayed slices.

on physician selected criteria. Specifically, metabolite concentrations for each voxel (from LCModel) were used to generate color-coded, semi-transparent alanine and choline[1] heat maps, examples of which are shown in Figure 50. The tumor voxels containing the two lowest and two highest alanine and/or choline concentrations were automatically highlighted in overlays generated as DICOM series. The overlays were then loaded into Stealth IGS along with corresponding anatomical MRI data, and both were visualized within a standard multi-planar reconstruction display

---

[1]Alanine and choline serve as focal examples in this study because of their importance in the context of meningiomas, but other metabolites can be treated similarly with the proposed methods.
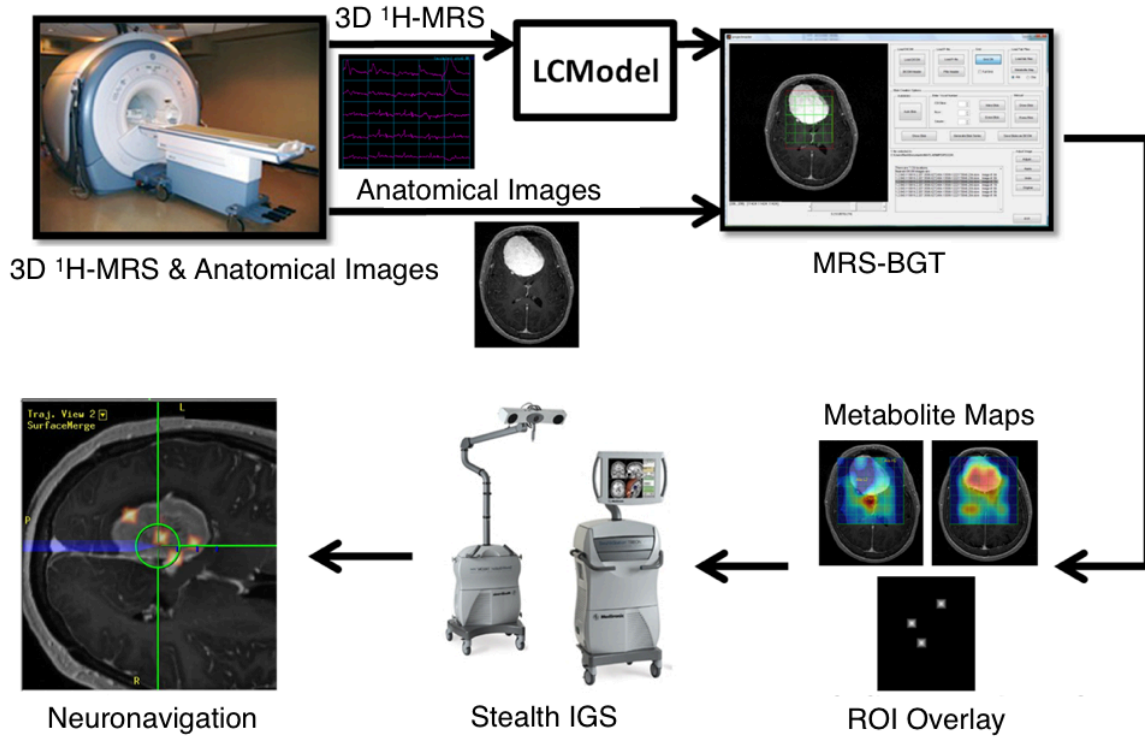
Figure 51. Flow diagram of the clinical workflow driven by the proposed methods.

configuration. Finally, biopsies were taken at locations corresponding to the four highlighted voxels prior to any meningioma excision (so that excision would not disrupt the accurate biopsy of tissue identified through pre-excision imaging). A flow diagram of the complete workflow described in this subsection is shown in Figure 51.

6.3   Results

6.3.1   Phantom Validation

Since the discrete distance measurements taken for validation were recorded in units of voxels, there should have been no errors between measurements taken from

the original images and those taken with Stealth IGS (in excess of the native lower bound on resolution characteristic of the cumulative acquisition/processing/display system, that is). A total of ten measurements between the selected voxels and intra-image landmarks were taken in three dimensions to validate the MRSI-BGT over-lays. Specifically, the distances between and across the voxels themselves as well as distances between the voxels and phantom boundaries were measured. As expected, there were no discrepancies between measurements taken with Stealth IGS and those from the original images taken with MRSI-BGT.

6.3.2 Clinical Application: Meningioma Biopsy

Integration of 3D ^{1}H-MRSI data into Stealth IGS successfully enabled pre-surgical selection of specific ROIs for later spectral and tissue analysis in the meningioma study. Specifically, the proposed methods were used to prospectively target tumor voxels based on subtle differences in metabolite concentrations. Figure 52 shows an example Stealth IGS overlay captured during an operation. As shown in the figure, ROI locations and metabolic characteristics were communicated to neurosurgeons through the MRSI-BGT overlays both before and during operations.

Thirty-five tissue samples were harvested during the meningioma study. The sample sites were documented with Stealth IGS screenshots and samples were immediately frozen in liquid nitrogen or preserved in formaldehyde for later examination. Of the 35 samples, 27 were usable for *ex vivo* histological, immunohistochemical, and NMR analysis. A solid tissue volume of ~0.3ml from each biopsy sample was suspended in deuterium oxide and examined *ex vivo* with high resolution magic angle spinning (HR-MAS) NMR spectroscopy. The HR-MAS spectra were then
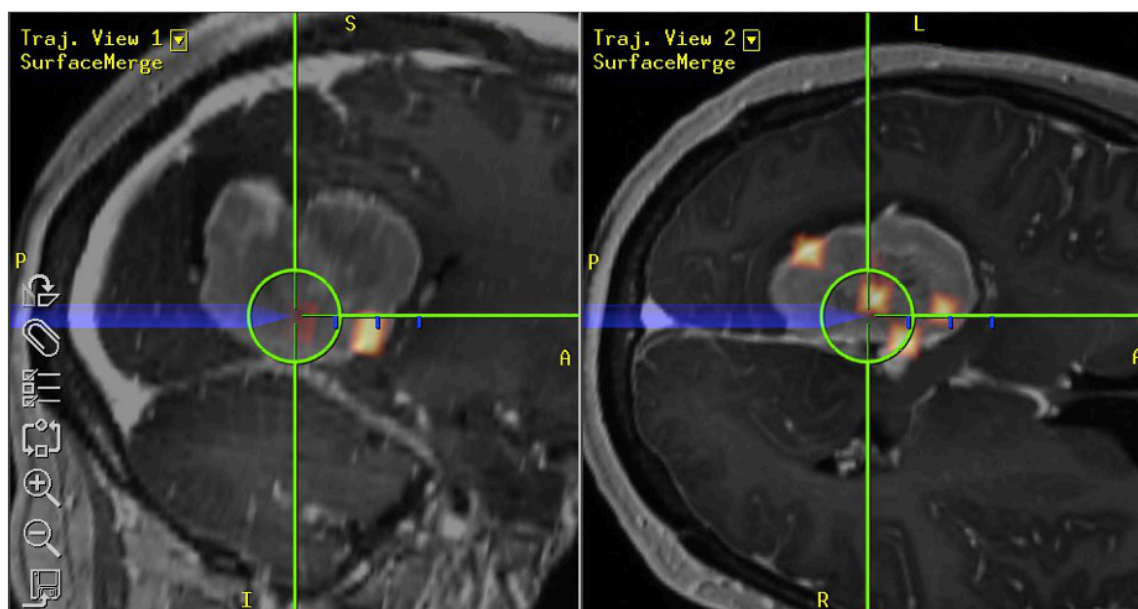
Figure 52. Screenshots of different perspectives from Stealth IGS during an operation. In each image, the highlighted 3D blobs indicate ROIs selected based on their metabolic profiles, and the blue arrows indicate where a neurosurgeon is actively working.

compared to *in vivo* 3D ^{1}H-MRSI spectra (across metabolites) using a Pearson correlation. Concentrations of alanine, lactate, creatine, choline, and myo-inositol were compared. Overall, the comparisons provided strong additional validation of the proposed overlays' utility as neuronavigational aids [Ala-Korpela *et al.* (1996); Govindaraju *et al.* (2000); Lehnhardt *et al.* (2001); Monleon *et al.* (2008); Ratai *et al.* (2005); Xu *et al.* (2007)]. Specifically, HR-MAS spectra showed reliable correlation with corresponding *in vivo* 3D ^{1}H-MRSI spectra: 23 of 27 spectral correlations were positive, seven of the 27 spectral correlations were significantly positive ($p < 0.05$), and 17 of the 27 correlations were greater than 0.60. Proportions of creatine, alanine, lactate, myo-inositol, and choline were also consistent between corresponding *in vivo* and *ex vivo* spectra. More detailed results can be found in Moore (2011).

6.4   Potential Application of Optical Flow in MRS-BGT

This section describes a potential application of optical flow in the overlay process of MRS-BGT. As described in the previous sections, the biopsy guidance framework requires two sets of image sets. Anatomical image set usually has higher out-of-plane resolution than spectroscopy dataset. Because these data sets have different resolutions, it is challenging to overlay the slices that align in the z-direction. In practice, the nearest slices are used in the overlay process. There may be problems in the overlay if the change in geometry in the anatomical slices in the z-direction is significant. The spectroscopy slice may need a better match in the z-direction. Figure 53 shows a sample case describing the mentioned problem. It should be noted that this is an overly simplified artificial case for demonstration purposes. In this sample problem, it is assumed that the desired geometry is at z=9.5cm. In Figure 54, it can be seen that the existing slices at locations z=9cm and z=10cm do not exactly match the geometry at slice location z=9.5cm. Since the purpose of the biopsy guidance is providing visual cues to surgeons, a motion estimation technique like optical flow can be used to interpolate the geometry between these slices. This would provide a better match for the spectroscopy data for the overlay in the operating room. The interpolated geometry is shown in Figure 55. It should be emphasized that the interpolated slice can not be used for diagnosis for any other purpose that require accurate MR data where a single pixel is important. This can be used only for providing a better visual region of interest when the geometry change between slices is significant or the anatomical data do not match the spectrocopy data in the z-direction. The proposed technique was not implemented in MRS-BGT for the reasons mentioned but it is still an application that has the potential to improve the biopsy guidance process.
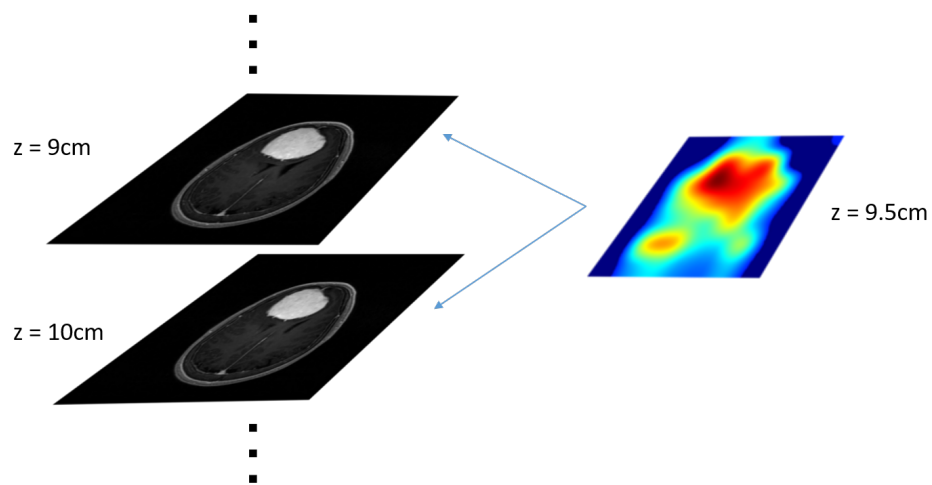
Figure 53. A simplified demonstration of a case where the spectroscopy and anatomical dataset slice locations are different. In this case the spectroscopy slice is in the middle of two slices in the anatomical dataset.
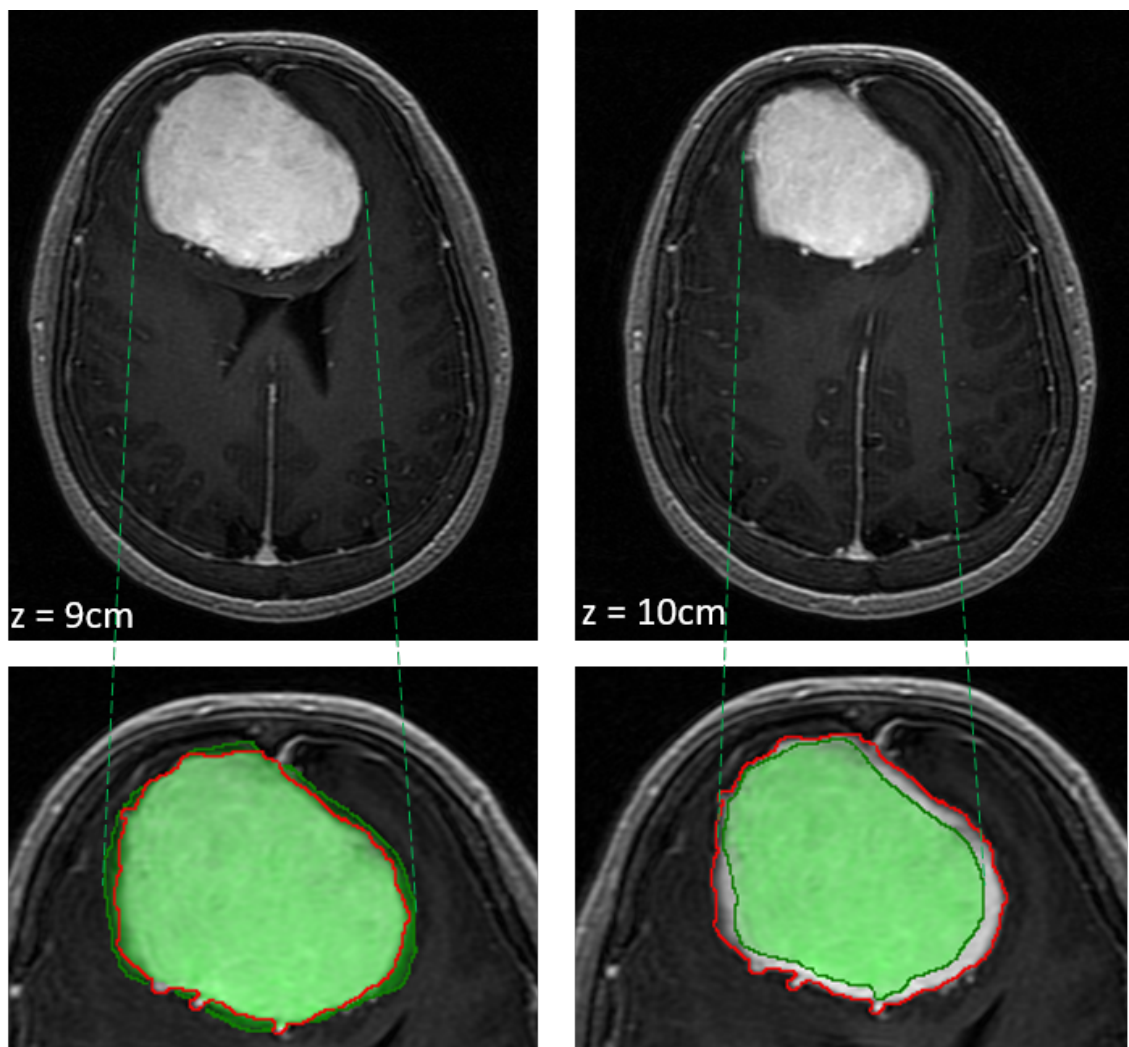
Figure 54. Slices overlaid on the original middle slice to demonstrate the change of geometry between slices. Red outlines the geometry in the desired slice. Green is the overlaid slice and it can be seen that the geometry is different than the desired slice geometry.

Interpolated with Optical Flow

Overlay on the original
middle slice

MRS overlay at z=9.5cm

Original
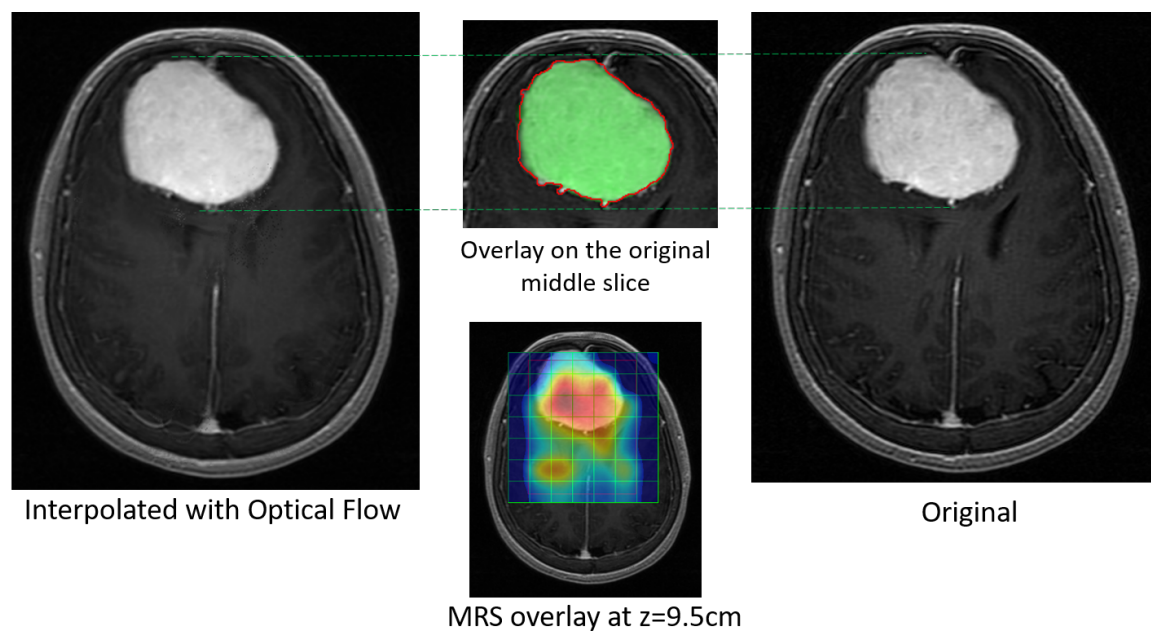
Figure 55. Interpolated middle slice at z=9.5cm and the desired slice comparison. It can be seen that the interpolated slice matches the desired geometry better than the neighboring slices.

6.5   Discussion & Conclusions

In this study, a proof of concept was demonstrated for neuronavigation framework driven by 3D MRI/MRSI data fusion. Specifically, 3D ^{1}H-MRSI data were integrated into an image-based neuronavigation system to provide online visualizations of both anatomy and *in vivo* biochemistry in the operating room. The proposed methods fully account for scanner calibration, and their accuracy was established through phantom validation and clinical application. The new methods make it possible to enhance tumor biopsy, characterization, and resection capabilities in comparison to standard neurosurgical practices that make no use of ^{1}H-MRSI data or rely on 2D data alone.

Note that using 3D ^{1}H-MRSI in this work (as opposed to more common 2D ^{1}H-MRSI) offers a number of important advantages. First, there is the well known improvement in signal-to-noise ratio (which increases proportionally with the square root of scan time). Second, there is the improved coverage, and flexibility of coverage, provided by a natively 3D sequence, which allows the region of support to be tailored well to tumor morphology. As a result, intra-tumor spectra can be measured both comprehensively and with high quality. Nevertheless, there are also several drawbacks to using 3D ^{1}H-MRSI. For one, a greater number of voxels will be affected by partial volume effects at the tumor interface in the 3D case, so spectra from those boundary voxels should be interpreted judiciously. There is also the aforementioned increase in scan time (in comparison to a single 2D ^{1}H-MRSI acquisition), which in some cases may be spent sampling extra-tumor voxels. However, a single 3D ^{1}H-MRSI scan may actually save time and money in comparison to previous

spectroscopic neuronavigation approaches that may call for multiple 2D ^{1}H-MRSI scans.

Integrating 3D MRSI data into standard neuronavigation systems is of great practical importance because neurosurgeons are already familiar with the systems and are comfortable using them in clinical workflows. With the proposed methods, 3D MRSI data can now be represented within those systems like data from any other compatible imaging modality. Specifically, the 3D MRSI data are represented in concert with anatomical MRI data through the use of color-coded, semi-transparent heat map overlays in DICOM format that communicate the metabolic characteristics and locations of selected ROIs. Similar (but differently purposed) overlays can also be generated easily using the tools that we have made publicly available. For example, overlays can be generated for manually specified data or for data from other MRI approaches (e.g., functional and/or perfusion MRI), both of which may be natively incompatible with standard neuronavigation systems.

Future work will address several noteworthy limitations of this study. First, the proposed methods should be applied to larger patients populations as in Frati *et al.* (2011) in order to more firmly establish their efficacy. Second, the current implementation of the methods is tailored to the GE platform, and thus should be generalized so as to facilitate widespread adoption. Lastly, the publicly available MRSI-BGT tool is compiled for Windows platforms, and should be translated for cross-platform use.

The proposed methods were applied clinically in this study after phantom validation to facilitate neuronavigated tissue biopsy, which provided valuable support for a recent meningioma grading study. Biopsy accuracy was favorable in that study: *in vivo* 3D ^{1}H-MRSI spectra agreed well with *ex vivo* HR-MAS spectra as well as histological and immunohistochemical analyses. Without spectroscopic guidance, volumes

113

of interest to be extracted in the meningioma study would have been identified based only on verbal and qualitative visual cues in the operating room, which would have prohibited any systematic validation of biopsy accuracy. With the proposed methods, however, 3D MRSI overlays were leveraged as quantitative neuronavigational aids to enhance neurosurgical capabilities, allowing neurosurgeons to pinpoint and access specific, confirmed biopsy targets. Our application of the methods demonstrates that 3D spectroscopy data can play a valuable role in the operating room, and more broadly that there is great potential for emerging imaging modalities to continue advancing the state-of-the-art in neuronavigation and neurosurgery.

Chapter 7

CONCLUSION

After presenting the proposed approaches and frameworks in the preceding chapters, a summary of conclusions is given in this final chapter. The main contributions of this dissertation are the collection of these methods that offer solutions to problems from three different areas of computer vision/image processing. All of them make use of modified optical flow methods for estimating motion fields to solve the encountered problems.

7.1 Summary of Methods and Contributions

In Chapter 3, we described a new optical flow-based framework for image interpolation that also reduces divergence. The proposed method uses flow velocity data to guide the interpolation toward lesser divergence in the interpolated data. The proposed method applies a symmetric interpolation setup and considers a new divergence term in addition to the brightness and smoothness terms in the energy functional. The method was applied to PIV, analytical, and CFD data and tested against two interpolation methods. The results indicate that the proposed method has potential to improve the interpolation of velocimetry data when it is difficult to achieve an out-of-plane resolution close to the in-plane resolution. The results also indicate that the effect of the new divergence term in the optical flow functional can be appreciated better as the distance between the interpolated slice and the neighboring slices increases.

In Chapter 4, we used optical flow and well established image processing methods to improve object extraction from SAR images. Optical flow fields have been effective for removing difficult false positives that result from registration and perspective problems. The proposed framework for distinguishing between actual motion and detected motion due to misregistration can lead to more accurate and meaningful change detection and improve object extraction from a SAR AGI product. Results demonstrate the ability of the optical flow based method to reduce false positives up to 60% in the tested SAR image regions where registration errors are prevalent.

In Chapter 5, we showed that unsupervised feature learning algorithms can be effectively used in conjunction with optical flow methods to generate 2CMV AGI products. Results demonstrate the ability of the techniques to reduce false positives in the tested SAR image pairs. For further improvement, more recent optical flow or motion estimation algorithms can be investigated as an alternative to the ones utilized in this work. It should be noted that the chosen optical flow method is suitable for the tested datasets and performs as expected since it takes into account the intensity changes between images.

In Chapter 6, we presented a proof of concept for neuronavigation framework driven by 3D MRI/MRSI data fusion. Specifically, 3D ^{1}H-MRSI data were integrated into an image-based neuronavigation system to provide online visualizations of both anatomy and *in vivo* biochemistry in the operating room. The proposed methods fully account for scanner calibration, and their accuracy was established through phantom validation and clinical application. The new methods make it possible to enhance tumor biopsy, characterization, and resection capabilities in comparison to standard neurosurgical practices that make no use of ^{1}H-MRSI data or rely on 2D data alone. Note that using 3D ^{1}H-MRSI in this work (as opposed to more com-

mon 2D ^{1}H-MRSI) offers a number of important advantages. First, there is the well known improvement in signal-to-noise ratio (which increases proportionally with the square root of scan time). Second, there is the improved coverage, and flexibility of coverage, provided by a natively 3D sequence, which allows the region of support to be tailored well to tumor morphology. As a result, intra-tumor spectra can be measured both comprehensively and with high quality. Nevertheless, there are also several drawbacks to using 3D ^{1}H-MRSI. For one, a greater number of voxels will be affected by partial volume effects at the tumor interface in the 3D case, so spectra from those boundary voxels should be interpreted judiciously. There is also the afore-mentioned increase in scan time (in comparison to a single 2D ^{1}H-MRSI acquisition), which in some cases may be spent sampling extra-tumor voxels. However, a single 3D ^{1}H-MRSI scan may actually save time and money in comparison to previous spectroscopic neuronavigation approaches that may call for multiple 2D ^{1}H-MRSI scans. With the proposed methods, however, 3D MRSI overlays were leveraged as quantitative neuronavigational aids to enhance neurosurgical capabilities, allowing neurosurgeons to pinpoint and access specific, confirmed biopsy targets. Proposed application of the methods demonstrates that 3D spectroscopy data can play a valuable role in the operating room, and more broadly that there is great potential for emerging imaging modalities to continue advancing the state-of-the-art in neuronavigation and neurosurgery. A potential application of optical flow was also proposed in the overlay portion of the biopsy guidance process. It was shown that optical flow-based interpolation can be used for providing a better visual region of interest when the geometry change between slices is significant or the anatomical data do not match the spectroscopy data in the out-of-plane direction.

7.2   Suggestions for Future Research

Possible future research may include applications of optical flow motion estimation in video inpainting. In various applications, videos may contain a reticle (crosshair) in the center of the frame. In some analysis software, the reticle may cause problems as it is not a part of the natural scene. Removal of the reticle and inpainting of the region may improve the reliability of the analysis software. A suitable motion estimator can track the movement of the reticle and its surrounding. This information can be used with an interpolator to fill in the reticle region with pixels that are consistent with their surrounding.

Investigating the use of machine learning techniques as a means to solve some of the inverse problems occurring in this work is a possible direction for continuing in this research area. It is known that several works have looked at machine learning to solve classic inverse problems like optical flow estimation, super-resolution etc. In addition to the unsupervised learning methods used in this work, supervised learning methods can be investigated. With training data, machine learning methods can be used for target extraction and classification in radar datasets. Replacing the feature learning or adaptive thresholding parts of the change detection framework with deep learning models may offer additional improvements. Generation of training and ground truth data would be essential to this application.

Another possible direction for future research can be the utilization of deep learning models to estimate optical flow. Recently, there have been some published works that use deep learning for estimating optical flow and the results indicate that while it is possible to use deep learning for optical flow estimation, there is still room for improvement. This can be a promising direction to advance the state-of-the-art in

optical flow. New loss functions can be researched and integrated into the presented framework for the interpolation of velocimetry data. The results obtained from these techniques can be compared to the results stated in this dissertation.

REFERENCES

ADNI-Aqual2, "Aqual2: A-cceptance qual-ification tool", http://adni.loni.usc.edu/methods/research-tools/, online; accessed October, 2018 (2018).

Adrian, R. J. and J. Westerweel, *Particle Image Velocimetry* (Cambridge University Press, 2011).

Aharon, M., M. Elad and A. Bruckstein, "K-SVD: An algorithm for designing overcomplete dictionaries for sparse representation", IEEE Trans. Signal Process. **54**, 11, 4311–4322 (2006).

Ala-Korpela, M., P. Posio, S. Mattila, A. Korhonen and S. Williams, "Absolute quantification of phospholipid metabolites in brain-tissue extracts by ^{1}H NMR spectroscopy", J Magn Reson B **113**, 184–189 (1996).

Alvarez, L., C. Castaño, M. García, K. Krissian, L. Mazorra, A. Salgado and J. Sánchez, "A variational approach for 3D motion estimation of incompressible PIV flows", in "Scale Space and Variational Methods in Computer Vision", edited by F. Sgallari, A. Murli and N. Paragios, pp. 837–847 (Springer Berlin Heidelberg, Berlin, Heidelberg, 2007).

Alvarez, L., C. Castaño, M. García, K. Krissian, L. Mazorra, A. Salgado and J. Sánchez, "A new energy-based method for 3D motion estimation of incompressible PIV flows", Computer Vision and Image Understanding **113**, 7, 802 − 810 (2009).

Alves, R. and J. Tavares, "Computer image registration techniques applied to nuclear medicine images", in "Computational and Experimental Biomedical Sciences: Methods and Applications", pp. 173–191 (Springer International Publishing, 2015).

Ashok, H. G. and D. R. Patil, "Survey on change detection in SAR images", IJCA Proceedings on National Conference on Emerging Trends in Computer Technology (NCETCT) **2**, 4–7 (2014).

Aubert, G. and P. Kornprobst, *Mathematical Problems in Image Processing: Partial Differential Equations and the Calculus of Variations* (Springer, 2006).

Babiker, M., L. Gonzalez, J. Ryan, F. Albuquerque, D. Collins, A. Elvikis and D. Frakes, "Influence of stent configuration on cerebral aneurysm fluid dynamics", J. Biomech. Eng. **45**, 440–447 (2011).

Baghaie, A. and Z. Yu, "Curvature-based registration for slice interpolation of medical images", in "Computational Modeling of Objects Presented in Images. Fundamentals, Methods, and Applications", pp. 69–80 (Springer International Publishing, 2014).

Baker, S. and I. Matthews, "Lucas-Kanade 20 years on: A unifying framework", Int J Comput Vision (IJCV) **56**, 221–255 (2004).

Barron, J., D. Fleet and S. Beauchemin, "Performance of optical flow techniques", Int J Comput Vision (IJCV) **12**, 43–77 (1994a).

Barron, J., D. Fleet and S. Beauchemin, "Performance of optical flow techniques", Int J Comput Vision **12**, 1, 43–77 (1994b).

Bazi, Y., L. Bruzzone and F. Melgani, "An unsupervised approach based on the generalized gaussian model to automatic change detection in multitemporal SAR images", IEEE Trans. Geosci. Remote Sens. **43**, 4, 874 – 887 (2005).

Beauchemin, S. and J. Barron, "The computation of optical flow", CSUR **27**, 433–466 (1995).

Bovolo, F. and L. Bruzzone, "A detail-preserving scale-driven approach to change detection in multitemporal SAR images", IEEE Trans. Geosci. Remote Sens. **43**, 12, 2963 – 2972 (2005).

Bruhn, A., J. Weickert, T. Kohlberger and C. Schnörr, "A multigrid platform for real-time motion computation with discontinuity-preserving variational methods", Int. J. Comput. Vis. **70**, 3, 257–277 (2006).

Bruhn, A., J. Weickert and C. Schnorr, "Lucas/Kanade meets Horn/Schunck: Combining local and global optic flow methods", Int J Comput Vision (IJCV) **61**, 211–231 (2005).

Brunet, F., E. Cid, A. Bartoli, E. Bouche, F. Risso and V. Roig, "Image registration algorithm for molecular tagging velocimetry applied to unsteady flow in Hele-Shaw cell", Experimental Thermal and Fluid Science **44**, 897–904 (2013).

Casa, L. and P. Krueger, "Radial basis function interpolation of unstructured, three-dimensional, volumetric particle tracking velocimetry data", Measurement Science and Technology **24**, 6, 065304 (2013).

Celik, T., "Unsupervised change detection in satellite images using principal component analysis and k-means clustering", IEEE Geosci. Remote Sens. Lett. **6**, 772–776 (2009).

Chen, Y., Y. Xie, Z. Zhou, F. Shi, A. G. Christodoulou and D. Li, "Brain MRI super resolution using 3D deep densely connected neural networks", in "2018 IEEE 15th International Symposium on Biomedical Imaging (ISBI 2018)", pp. 739–742 (2018).

Chernov, M., Y. Muragaki, T. Ochiai, T. Taira, Y. Ono, M. Usukura, T. Maruyama, K. Nakaya, R. Nakamura, H. Iseki, O. Kubo, T. Hori and K. Takakura, "Spectroscopy-supported frame-based image-guided stereotactic biopsy of paranchymal brain lesions: Comparative evaluation of diagnostic yield and diagnostic accuracy", Clin Neurol Neurosurg **111**, 527–535 (2009).

Chernov, M., Y. Muragaki, T. Taira and H. Iseki, "^{1}H-MRS-guided stereotactic brain biopsy", Stereotact Funct Neurosurg **90**, 63–65, letter to the editor (2012).

Corpetti, T., D. Heitz, G. Arroyo, E. Mémin and A. Santa-Cruz, "Fluid experimental flow estimation based on an optical-flow scheme", Experiments in Fluids **40**, 1, 80–97 (2006).

Coupe, P., P. Hellier, C. Kervrann and C. Barillot, "Nonlocal means-based speckle filtering for ultrasound images", IEEE Trans. Image Process. **18**, 2221–2229 (2009).

Dekker, R. J., "Speckle filtering in satellite SAR change detection imagery", Int. J. Remote Sens. **19**, 6, 1133 – 1146 (1998).

Dosovitskiy, A., P. Fischer, E. Ilg, P. Hausser, C. Hazirbas, V. Golkov, P. van der Smagt, D. Cremers and T. Brox, "Flownet: Learning optical flow with convolutional networks", in "The IEEE International Conference on Computer Vision (ICCV)", (2015).

El-Darymli, K., E. W. Gill, P. McGuire, D. Power and C. Moloney, "Automatic target detection in synthetic aperture radar imagery: A state-of-the-art review", IEEE Access **4**, 6014–6058 (2016).

El-Darymli, K., P. McGuire, D. Power and C. Moloney, "Target detection in synthetic aperture radar imagery: A state-of-the-art survey", J. Appl. Remote Sens. **7**, 1, 071598 (2013).

Elkins, C. and M. Alley, "Magnetic resonance velocimetry: applications of magnetic resonance imaging in the measurement of fluid motion", Exp. Fluids **43**, 6, 823–858 (2007).

Fortun, D., P. Bouthemy and C. Kervrann, "Optical flow modeling and computation: A survey", Comput Vis Image Und **134**, 1–21 (2015a).

Fortun, D., P. Bouthemy and C. Kervrann, "Optical flow modeling and computation: A survey", Computer Vision and Image Understanding **134**, 1–21 (2015b).

Frakes, D., C. Conrad, T. Healy, J. Monaco, M. Smith, M. Fogel, S. Sharma and A. Yoganathan, "Application of an adaptive control grid interpolation technique to morphological vascular reconstruction", IEEE Trans. Biomed. Eng. **50**, 197–206 (2003).

Frakes, D., K. Pekkan, L. Dasi, H. Kitajima, D. Zelicourt, H. Leo, J. Carberry, K. Sundareswaran, H. Simon and A. Yoganathan, "Modified control grid interpolation for the volumetric reconstruction of fluid flows", Exp. Fluids **45**, 987–997 (2008).

Frakes, D., M. Smith, D. de Zelicourt, K. Pekkan and A. Yoganathan, "Three-dimensional velocity field reconstruction", J. Biomech. Eng. **126**, 727–735 (2004).

Frati, A., A. Pichierri, S. Bastianello, A. Raco, A. Santoro, V. Esposito, F. Giangaspero and M. Salvati, "Frameless stereotactic cerebral biopsy: Our experience in 296 cases", Stereotact Funct Neurosurg **89**, 234–245 (2011).

Frost, V., J. A. Stiles, K. S. Shanmugan and J. C. Holtzman, "A model for radar images and its application to adaptive digital filtering of multiplicative noise", IEEE Trans. Pattern Anal. Machine Intell. **PAMI-4**, 157–166 (1982).

Ganslandt, O., A. Stadlbauer, R. Fahlbusch, K. Kamada, R. Buslei, I. Blumcke, E. Moser and C. Nimsky, "Proton magnetic spectroscopic imaging integrated into image-guided surgery: Correlation to standard magnetic resonance imaging and tumor cell density", Neurosurgery **56**, 291–298 (2005).

Gao, F., J. Dong, B. Li, Q. Xu and C. Xie, "Change detection from synthetic aperture radar images based on neighborhood-based ratio and extreme learning machine", J. Appl. Remote Sens. **10**, $10 - 10 - 14$ (2016).

Gennert, M. and S. Negahdaripour, "Relaxing the brightness constancy assumption in computing optical flow", A.I. Lab Memo 975, Massachusetts Institute of Technology (1987).

Ghosh, A., N. Mishra and S. Ghosh, "Fuzzy clustering algorithms for unsupervised change detection in remote sensing images", Information Sciences **181**, 4, $699 - 715$ (2011).

Głomb, G. and G. Świrniak, "Particle image models for optical flow-based velocity field estimation in image velocimetry", in "Proc. SPIE 10679, Optics, Photonics, and Digital Technologies for Imaging Applications V", vol. 10679 (2018).

Głomb, G., G. Świrniak and J. Mroczka, "An optical flow-based method for velocity field of fluid flow estimation", in "Proc. SPIE 10329, Optical Measurement Systems for Industrial Inspection X", vol. 10329 (2017).

Gong, M., L. Su, M. Jia and W. Chen, "Fuzzy clustering with a modified mrf energy function for change detection in synthetic aperture radar images", IEEE Trans. Fuzzy Syst. **22**, 1, $98 - 109$ (2014).

Gonzalez, R. and R. Woods, *Digital Image Processing* (Upper Saddle River, NJ: Prentice-Hall, 2006), 3 edn.

Govindaraju, V., K. Young and A. Maudsley, "Proton nmr chemical shifts and coupling constants for brain metabolites", NMR Biomed **13**, 129–153 (2000).

Gupta, S. N. and J. L. Prince, "On div-curl regularization for motion estimation in 3-d volumetric imaging", in "Proceedings of 3rd IEEE International Conference on Image Processing", vol. 1, pp. 929 – 932 (1996a).

Gupta, S. N. and J. L. Prince, "Stochastic models for div-curl optical flow methods", IEEE Signal Processing Letters **3**, 2, 32–34 (1996b).

Habermehl, C., J. Steinbrink, K. Muller and S. Haufe, "Optimizing the regularization for image reconstruction of cerebral diffuse optical tomography", J. Biomed. Opt. **19** (2014).

Heitz, D., E. Mémin and C. Schnörr, "Variational fluid flow measurements from image sequences: synopsis and perspectives", Experiments in Fluids **48**, 3, 369–393 (2010).

Herlin, I., D. Béréziat, N. Mercier and S. Zhuk, "Divergence-free motion estimation", in "Computer Vision – ECCV 2012", edited by A. Fitzgibbon, S. Lazebnik, P. Perona, Y. Sato and C. Schmid, pp. 15–27 (Springer Berlin Heidelberg, Berlin, Heidelberg, 2012).

Hermann, E., E. Hattingen, J. Krauss, G. Marquardt, U. Pilatus, K. Franz, M. Setzer, T. Gasser, D. Tews, F. Zanella, V. Seifert and H. Lanfermann, "Stereotactic biopsy in gliomas guided by 3-Tesla [1]H-chemical-shift imaging of choline", Stereotact Funct Neurosurg **86**, 300–307 (2008).

Hoon, N. D., A. Jalba, E. Eisemann and A. Vilanova, "Temporal interpolation of 4D PC-MRI blood-flow measurements using bidirectional physics-based fluid simulation", in "Eurographics Workshop on Visual Computing for Biology and Medicine", (The Eurographics Association, 2016).

Horn, B. and B. Schunck, "Determining optical flow", A.I. Memo 572, Massachusetts Institute of Technology (1980).

Jia, L., M. Li, P. Zhang and Y. Wu, "SAR image change detection based on correlation kernel and multistage extreme learning machine", IEEE Trans. Geosci. Remote Sens. **54**, 10, 5993 – 6006 (2016).

Jovicich, J. and S. Czanner, "Gradient non-linearity distortion correction", https://na-mic.org/wiki/Mbirn:_Gradient_non-linearity_distortion_correction, online; accessed October, 2018 (2005).

Jovicich, J., S. Czanner, D. Greve, E. Haley, A. V. D. Kouwe, R. Gollub, D. Kennedy, F. Schmitt, G. Brown, J. Macfall, B. Fischl and A. Dale, "Reliability in multi-site structural mri studies: Effects of gradient non-linearity correction on phantom and human data", Neuroimage **30**, 436–443 (2006).

Jr, C. J., M. Bernstein, N. Fox, P. Thompson, G. Alexander, D. Harvey, B. Borowski, P. Britson, J. Whitwell, C. Ward and et al, "The alzheimer's disease neuroimaging initiative (adni): Mri methods", J Magn Reson Imaging **27**, 685–691 (2008).

Kanberoglu, B., J. Debbins and L. Karam, "Accurate brain tumor biopsy using ^{1}H-MRS neuronavigation", in "Proc Intl Soc Mag Reson Med", (2010).

Kanberoglu, B. and D. Frakes, "Extraction of advanced geospatial intelligence (AGI) from commercial synthetic aperture radar imagery", in "Proc. SPIE", vol. 10201, pp. 1020106–1020106–9 (2017), URL http://dx.doi.org/10.1117/12.2262359.

Kanberoglu, B., L. Karam, T. Trouard and J. Debbins, "Scanner calibration for multisite geometric accuracy: How to do it", in "Proc Intl Soc Mag Reson Med", (2009).

Kanberoglu, B., P. Nair and D. Frakes, "An optical flow-based approach for the interpolation of minimally divergent velocimetry data", in "2017 IEEE 14th International Symposium on Biomedical Imaging (ISBI 2017)", pp. 538–542 (2017).

Karani, N., C. Tanner, S. Kozerke and E. Konukoglu, "Reducing navigators in free-breathing abdominal mri via temporal interpolation using convolutional neural networks", IEEE Trans. Med. Imag. (2018).

Keys, R., "Cubic convolution interpolation for digital image processing", IEEE Trans Acoust, Speech, Signal Process **29**, 1153–1160 (1981).

Lee, J. S., "Digital image enhancement and noise filtering by use of local statistics", IEEE Trans. Pattern Anal. Machine Intell. **PAMI-2**, 165–168 (1980).

Lehman, T., C. Gonner and K. Spitzer, "Survey: Interpolation methods in medical image processing", IEEE Trans. Med. Imag. **18**, 291–294 (1999).

Lehnhardt, F., G. Rohn, R. Ernestus, M. Grune and M. Hoehn, "^{1}H-and ^{31}P-MR spectroscopy of primary and recurrent human brain tumors in vitro: malignancy-characteristic profiles of water soluble and lipophilic spectral components", NMR Biomed **14**, 307–317 (2001).

Li, H., T. Celik, N. Longbotham and W. J. Emery, "Gabor feature based unsupervised change detection of multitemporal SAR images based on two-level clustering", IEEE Geosci. Remote Sens. Lett. **12**, 12, 2458–2462 (2015).

Li, W., J. Chen, P. Yang and H. Sun, "Multitemporal SAR images change detection based on joint sparse representation of pair dictionaries", in "2012 IEEE Int. Geosci. and Remote Sens. Symp.", pp. 6165–6168 (IEEE, 2012).

Liberman, G., E. Solomon, M. Lustig and L. Frydman, "Multiple-coil k-space interpolation enhances resolution in single-shot spatiotemporal mri", Magnetic Resonance in Medicine **79**, 2, 796–805 (2018).

Lin, Q., Q. Zhang and L. Tongbin, "Slice interpolation in mri using a decomposition-reconstruction method", in "2017 4th International Conference on Information Science and Control Engineering (ICISCE)", pp. 678–681 (2017).

Liu, Y., X. Chen, Z. Wang, Z. Wang, R. Ward and X. Wang, "Deep learning for pixel-level image fusion: Recent advances and future prospects", Information Fusion **42**, 158–173 (2018).

Lopes, A., E. Nezry, R. Touzi and H. Laur, "Maximum a posteriori filtering and first order texture models in SAR images", in "10th Annu. Int. Symp. GeoSci. Remote Sens.", pp. 2409–2412 (IEEE, 1990a).

Lopes, A., R. Touzi and E. Nezry, "Adaptive speckle filters and scene heterogeneity", IEEE Trans. Geosci. Remote Sens. **28**, 992–1000 (1990b).

Lu, X., Y. Yuan and X. Zheng, "Joint dictionary learning for multispectral change detection", IEEE Trans. Cybern. **47**, 884–897 (2017).

Lucas, B. and T. Kanade, "An iterative image registration technique with an application to stereo vision", in "In IJCAI81", pp. 674–679 (1981).

Majos, C., J. Alonso, C. Aguilera, M. Serralonga, J. Perez-Martin, J. Acebes, C. Arus and J. Gili, "Proton magnetic resonance spectroscopy (^{1}h-mrs) of human brain tumors: Assessment of differences between tumor types and its applicability in brain tumor categorization", Eur Radiol **13**, 582–591 (2003).

McKnight, T., M. V. dem Bussche, D. Vigneron, Y. Lu, M. Berger, M. McDermott and W. Dillon, "Histopathological validation of a three-dimensional magnetic resonance spectroscopy index as a predictor of tumor presence", J Neurosurg **97**, 794–802 (2002).

McLean, M., F. Woermann, G. Barker and J. Duncan, "Quantitative analysis of short echotime ^{1}h-mrsi of cerebral gray and white matter", Magn Reson Med **44**, 401–411 (2000).

Melgani, F. and Y. Bazi, "Markovian fusion approach to robust unsupervised change detection in remotely sensed imagery", IEEE Geosci. Remote Sens. Lett. **3**, 4, 457–461 (2006).

Melnikov, D. and V. Shevtsova, "Liquid particles tracing in three dimensional buoyancy driven flows", Fluid Dyn. Mater. Process **1**, 189–199 (2005).

Monleon, D., J. Morales, J. Gonzalez-Darder, F. Talamantes, O. Cortes, R. Gil-Benso, C. Lopez-Gines, M. Cerda-Nicolas and B. Celda, "Benign and atypical meningioma metabolic signatures by high-resolution magic-angle spinning molecular profiling", J Proteome Res **7**, 2882–2888 (2008).

Moore, N., *Meningiomas assessed with in vivo 3D ^{1}H-magnetic resonance spectroscopy integrated into a standard neurosurgical image guidance system: determining biochemical markers of clinically aggressive behavior and providing a resection advantage*, Ph.D. thesis, University of Arizona (2011).

Moser, G. and S. B. Serpico, "Generalized minimum-error thresholding for unsupervised change detection from SAR amplitude imagery", IEEE Trans. Geosci. Remote Sens. **44**, 10, 2972 – 2982 (2006).

Ng, W. and T. Lim, "Targeting regions with highest lipid content on mr spectroscopy may improve diagnostic yield in stereotactic biopsy", J Clin Neurosci **15**, 502–506 (2008).

Nguyen, L. H. and T. D. Tran, "A sparsity-driven joint image registration and change detection technique for SAR imagery", in "2010 IEEE ICASSP", pp. 2798–2801 (2010).

Oktay, O., W. Bai, M. Lee, R. Guerrero, K. Kamnitsas, J. Caballero, A. de Marvao, S. Cook, D. O'Regan and D. Rueckert, "Multi-input cardiac image superresolution using convolutional neural networks", in "Medical Image Computing and Computer-Assisted Intervention – MICCAI 2016", pp. 246–254 (Springer International Publishing, 2016).

Ozturk, C., J. Derbyshire and E. McVeigh, "Estimating motion from mri data", in "Proc. IEEE Inst. Electr. Electron Eng.", pp. 1627–1648 (IEEE, 2003).

Park, S., M. Park and M. Kang, "Super-resolution image reconstruction: a technical overview", IEEE Signal Process. Mag. **20** (2003).

Pedlosky, J., *Geophysical fluid dynamics* (Springer, 1987).

Penney, G., J. Schnabel, D. Rueckert, M. Viergever and W. Niessen, "Registrationbased interpolation", IEEE Trans. Med. Imag. **23**, 922–926 (2004).

Pfisterer, W., W. Hendricks, A. Scheck, R. Nieman, T. Birkner, W. Krampla and M. Preul, "Fluorescent in situ hybridization and ex vivo ^{1}h magnetic resonance spectroscopic examinations of meningioma tumor tissue: Is it possible to identify

a clinically-aggressive subset of benign meningiomas?”, Neurosurgery **61**, 1048–1059 (2007).

Pfisterer, W., R. Nieman, A. Scheck, S. Coons, R. Spetzler and M. Preul, “Using ex-vivo proton magnetic resonance spectroscopy to reveal associations between biochemical and biological features of meningiomas”, Neurosurg Focus **28** (2010).

Pham, C., A. Ducournau, R. Fablet and F. Rousseau, “Brain mri super-resolution using deep 3d convolutional networks”, in “2017 IEEE 14th International Symposium on Biomedical Imaging (ISBI 2017)”, pp. 197–200 (2017).

Preul, M., Z. Caramanos, D. Collins, J. Villemure, R. Leblanc, A. Olivier, R. Pokrupa and D. Arnold, “Accurate, noninvasive diagnosis of human brain tumors by using proton magnetic resonance spectroscopy”, Nat Med **2**, 323–325 (1996).

Preul, M., Z. Caramanos, R. Leblanc, J. Villemure and D. Arnold, “Using pattern analysis of in vivo proton mrsi data to improve the diagnosis and surgical management of patients with brain tumors”, NMR Biomed **11**, 192–200 (1998).

Provencher, S., “Estimation of metabolite concentrations from localized in vivo proton nmr spectra”, Magn Reson Med **30**, 672–679 (1993).

Raffel, M., C. Willert and J. Kompenhans, *Particle Image Velocimetry: A Practical Guide* (Springer, 2013).

Ratai, E., S. Pilkenton, M. Lentz, J. Greco, R. Fuller, J. Kim, J. He, L. Cheng and R. Gonzalez, “Comparisons of brain metabolites observed by hr-mas [1]h nmr of intact tissue and solution [1]h nmr of tissue extracts in siv-infected macaques”, NMR Biomed **18**, 242–251 (2005).

Ren, W., J. Song, S. Tian and W. Wu, “Survey on unsupervised change detection techniques in SAR images1”, in “2014 IEEE China Summit International Conference on Signal and Information Processing (ChinaSIP)”, pp. 143–147 (IEEE, 2014).

Roszelle, B., P. Nair, L. Gonzalez, M. Babiker, J. Ryan and D. Frakes, “Comparison among different high porosity stent configurations: Hemodynamic effects of treatment in a large cerebral aneurysm”, J. Biomech. Eng. **136** (2014).

Roszkowiak, L., A. Korzynska, J. Zak, D. Pijanowska, Z. Swiderska-Chadaj and T. Markiewicz, “Survey: interpolation methods for whole slide image processing”, Journal of Microscopy **265**, 148–158 (2017).

Rubinstein, R., M. Zibulevsky and M. Elad, “Efficient implementation of the K-SVD algorithm using batch orthogonal matching pursuit”, Tech. rep., Technion (2008).

Ruhnau, P. and C. Schnörr, "Optical stokes flow estimation: an imaging-based control approach", Experiments in Fluids **42**, 1, 61–78 (2007).

Ruhnau, P., A. Stahl and C. Schnörr, "Variational estimation of experimental fluid flows with physics-based spatio-temporal regularization", Measurement Science and Technology **18**, 3, 755 (2007).

Scarano, F., "Iterative image deformation methods in piv", Measurement Science and Technology **13**, 1, R1–R19 (2002).

Shaw, C. and P. Yalavarthy, "Effective contrast recovery in rapid dynamic near-infrared diffuse optical tomography using ℓ_1-norm-based linear image reconstruction method", J. Biomed. Opt. **17** (2012).

Shi, Z. and K. Fung, "A comparison of digital speckle filters", in "GeoSci. Remote Sens. Symp. (IGARSS'1994)", vol. 4, pp. 2129–2133 (IEEE, 1994).

Sibtain, N., F. Howe and D. Saunders, "The clinical value of proton magnetic resonance spectroscopy in adult brain tumours", Clin Radiol **62**, 109–119 (2007).

Sled, J., "Non-parametric non-uniform intensity normalization", https://en.wikibooks.org/wiki/MINC/Tools/N3, online; accessed October, 2018 (1998a).

Sled, J., "Non-parametric non-uniform intensity normalization software", https://github.com/BIC-MNI/N3, online; accessed October, 2018 (1998b).

Sled, J., A. Zijdenbos and A. Evans, "A non-parametric method for automatic correction of intensity non-uniformity in mri data", IEEE Trans Med Imaging **17**, 87–97 (1998).

Son, B., M. Kim, B. Choi, E. Kim, H. Baik, B. Chloe, S. Naruse and J. Kang, "Proton magnetic resonance chemical shift imaging (^{1}H CSI)-directed stereotactic biopsy", Acta Neurochir (Wien) **143**, 45–49, discussion 49-50 (2001).

Song, S. M. and R. Leahy, "Computation of 3-D velocity fields from 3-D cine CT images of a human heart", IEEE Trans. Med. Imag. **10**, 3, 295 – 306 (1991).

Stadlbauer, A., E. Moser, S. Gruber, R. Buslei, C. Nimsky, R. Fahlbusch and O. Ganslandt, "Improved delineation of brain tumors: An automated method for segmentation based on pathologic changes of ^{1}h-mrsi metabolites in gliomas", Neuroimage **23**, 454–461 (2004a).

Stadlbauer, A., E. Moser, S. Gruber, C. Nimsky, R. Fahlbusch and O. Ganslandt, "Integration of biochemical images of a tumor into frameless stereotaxy achieved using a magnetic resonance imaging/magnetic resonance spectroscopy hybrid data set", J Neurosurg **101**, 287–294 (2004b).

Sumaiya, M. N. and R. S. S. Kumari, "Logarithmic mean-based thresholding for SAR image change detection", IEEE Geosci. Remote Sens. Lett. **13**, 11, 1726 – 1728 (2016).

Sun, D., S. Roth and M. Black, "A quantitative analysis of current practices in optical flow estimation and the principles behind them", International Journal of Computer Vision **106**, 2, 115–137 (2014).

Suter, D., "Motion estimation and vector splines", in "1994 Proceedings of IEEE Conference on Computer Vision and Pattern Recognition", pp. 939–942 (1994).

Teoh, K., H. Ibrahim and S. Bejo, "Investigation on several basic interpolation methods for the use in remote sensing application", in "Proc. IEEE CITISIA", (IEEE, 2008).

This, A., L. Boilevin-Kayl, H. Morales, O. Bonnefous, P. Allain, M. Fernández and J. Gerbeau, "One mesh to rule them all: Registration-based personalized cardiac flow simulations", in "Functional Imaging and Modelling of the Heart", pp. 441–449 (Springer International Publishing, 2017).

Titus, J. and S. Geroge, "A comparison study on different interpolation methods based on satellite images", IJERT **2** (2013).

Verri, A., R. Verri and T. Poggio, "Motion field and optical flow: Qualitative properties", IEEE Trans. Pattern Anal. Mach. Intell **11**, 490–498 (1989).

Witwit, W., Y. Zhao, K. Jenkins and Y. Zhao, "Satellite image resolution enhancement using discrete wavelet transform and new edge-directed interpolation", Journal of Electronic Imaging **26** (2017).

Xu, M., J. Ye, D. Yang, X. Xu, T. Yeo, W. Ng and C. Lim, "Ex-vivo nmr of unprocessed tissue in water: A simplified procedure for studying intracranial neoplasms", Anal Bioanal Chem **389**, 2153–2159 (2007).

Yousif, O. and Y. Ban, "Improving SAR-based urban change detection by combining MAP-MRF classifier and nonlocal means similarity weights", IEEE J. Sel. Topics Appl. Earth Observ **7**, 10, 4288 – 4300 (2014).

Yu, Y. and S. Acton, "Speckle reducing anisotropic diffusion", IEEE Trans. Image Process. **11**, 1260–1270 (2002).

Zhong, Q., H. Yang and Z. Yin, "An optical flow algorithm based on gradient constancy assumption for piv image processing", Measurement Science and Technology **28**, 5, 055208 (2017).

Zitova, B. and J. Flusser, "Image registration methods: A survey", Image Vis Comput **21**, 977–1000 (2003).

APPENDIX A

DERIVATION STEPS

$$\epsilon = \iint \left[I_x\alpha + I_y\beta + I_z\right]^2 + \gamma^2 \left[D_x\alpha + D_y\beta + D_z\right]^2 + \lambda^2 \left[\|\nabla\alpha\|^2 + \|\nabla\beta\|^2\right] dx\, dy$$

(A.1)

This can be minimized by solving the associated Euler-Lagrange equations.

$$\frac{\partial L}{\partial\alpha} - \frac{\partial}{\partial x}\frac{\partial L}{\partial\alpha_x} - \frac{\partial}{\partial y}\frac{\partial L}{\partial\alpha_y} = 0$$

$$\frac{\partial L}{\partial\beta} - \frac{\partial}{\partial x}\frac{\partial L}{\partial\beta_x} - \frac{\partial}{\partial y}\frac{\partial L}{\partial\beta_y} = 0$$

where L is the integrand of the energy functional.

$$L = \left[I_x\alpha + I_y\beta + I_z\right]^2 + \gamma^2 \left[D_x\alpha + D_y\beta + D_z\right]^2 + \lambda^2 \left[\|\nabla\alpha\|^2 + \|\nabla\beta\|^2\right]$$ (A.2)

$$\frac{\partial L}{\partial\alpha} = 2I_x\left(I_x\alpha + I_y\beta + I_z\right) + 2\gamma^2 D_x\left(D_x\alpha + D_y\beta + D_z\right)$$

$$\frac{\partial L}{\partial\beta} = 2I_y\left(I_x\alpha + I_y\beta + I_z\right) + 2\gamma^2 D_y\left(D_x\alpha + D_y\beta + D_z\right)$$

$$\frac{\partial}{\partial x}\frac{\partial L}{\partial\alpha_x} = 2\lambda^2\alpha_{xx}$$

$$\frac{\partial}{\partial y}\frac{\partial L}{\partial\alpha_y} = 2\lambda^2\alpha_{yy}$$

$$\frac{\partial}{\partial x}\frac{\partial L}{\partial\beta_x} = 2\lambda^2\beta_{xx}$$

$$\frac{\partial}{\partial y}\frac{\partial L}{\partial\beta_y} = 2\lambda^2\beta_{yy}$$

$$2I_x\left(I_x\alpha + I_y\beta + I_z\right) + 2\gamma^2 D_x\left(D_x\alpha + D_y\beta + D_z\right) - 2\lambda^2\Delta\alpha = 0$$
$$2I_y\left(I_x\alpha + I_y\beta + I_z\right) + 2\gamma^2 D_y\left(D_x\alpha + D_y\beta + D_z\right) - 2\lambda^2\Delta\beta = 0$$

After rearranging the terms, we get:

$$\left(I_x^2 + \gamma^2 D_x^2\right)\alpha + \left(I_x I_y + \gamma^2 D_x D_y\right)\beta = \lambda^2\Delta\alpha - I_x I_z - \gamma^2 D_x D_z$$
$$\left(I_x I_y + \gamma^2 D_x D_y\right)\alpha + \left(I_y^2 + \gamma^2 D_y^2\right)\beta = \lambda^2\Delta\beta - I_y I_z - \gamma^2 D_y D_z$$

approximating the Laplacians of α and β,

$$\Delta\alpha \approx \rho\left(\overline{\alpha} - \alpha\right)$$
$$\Delta\beta \approx \rho\left(\overline{\beta} - \beta\right)$$

133

where ρ is a proportionality constant and, $\overline{\alpha}$ and $\overline{\beta}$ are local averages. These approximations are substituted for Laplacians and the terms in the equation are rearranged.

$$\left(I_x^2 + \gamma^2 D_x^2 + \lambda^2\right)\alpha + \left(I_x I_y + \gamma^2 D_x D_y\right)\beta = \lambda^2 \overline{\alpha} - \left(I_x I_z + \gamma^2 D_x D_z\right)$$
$$\left(I_x I_y + \gamma^2 D_x D_y\right)\alpha + \left(I_y^2 + \gamma^2 D_y^2 + \lambda^2\right)\beta = \lambda^2 \overline{\beta} - \left(I_y I_z + \gamma^2 D_y D_z\right)$$

Determinants can be used to solve the above equations.

$$\alpha = \frac{Det_\alpha}{Det}$$
$$\beta = \frac{Det_\beta}{Det}$$

$$Det = \begin{vmatrix} \left(I_x^2 + \gamma^2 D_x^2 + \lambda^2\right) & \left(I_x I_y + \gamma^2 D_x D_y\right) \\ \left(I_x I_y + \gamma^2 D_x D_y\right) & \left(I_y^2 + \gamma^2 D_y^2 + \lambda^2\right) \end{vmatrix}$$
$$= \gamma^2 \left(I_x D_y - I_y Dx\right)^2 + \lambda^2 \left(\lambda^2 + I_x^2 + I_y^2 + \gamma^2 D_x^2 + \gamma^2 D_y^2\right)$$

$$Det_\alpha = \begin{vmatrix} \lambda^2 \overline{\alpha} - \left(I_x I_z + \gamma^2 D_x D_z\right) & \left(I_x I_y + \gamma^2 D_x D_y\right) \\ \lambda^2 \overline{\beta} - \left(I_y I_z + \gamma^2 D_y D_z\right) & \left(I_y^2 + \gamma^2 D_y^2 + \lambda^2\right) \end{vmatrix}$$
$$= \lambda^2 \left(I_y^2 + \gamma^2 D_y^2 + \lambda^2\right)\overline{\alpha} - \lambda^2 \left(I_x I_y + \gamma^2 D_x D_y\right)\overline{\beta} - \lambda^2 \left(I_x I_z + \gamma^2 D_x D_z\right)$$
$$\qquad - \gamma^2 \left(I_x I_z D_y^2 + I_y^2 D_x D_z - I_y I_z D_x D_y - I_x I_y D_y D_z\right)$$
$$A = \lambda^2 \left(I_x I_z + \gamma^2 D_x D_z\right) - \gamma^2 \left(I_x I_z D_y^2 + I_y^2 D_x D_z - I_y I_z D_x D_y - I_x I_y D_y D_z\right)$$
$$Det_\alpha = \lambda^2 \left(I_y^2 + \gamma^2 D_y^2 + \lambda^2\right)\overline{\alpha} - \lambda^2 \left(I_x I_y + \gamma^2 D_x D_y\right)\overline{\beta} - A$$

$$Det_\beta = \begin{vmatrix} \left(I_x^2 + \gamma^2 D_x^2 + \lambda^2\right) & \lambda^2 \overline{\alpha} - \left(I_x I_z + \gamma^2 D_x D_z\right) \\ \left(I_x I_y + \gamma^2 D_x D_y\right) & \lambda^2 \overline{\beta} - \left(I_y I_z + \gamma^2 D_y D_z\right) \end{vmatrix}$$
$$= -\lambda^2 \left(I_x I_y + \gamma^2 D_x D_y\right)\overline{\alpha} + \lambda^2 \left(I_x^2 + \gamma^2 D_x^2 + \lambda^2\right)\overline{\beta} - \lambda^2 \left(I_y I_z + \gamma^2 D_y D_z\right)$$
$$\qquad - \gamma^2 \left(I_y I_z D_x^2 + I_x^2 D_y D_z - I_x I_z D_x D_y - I_x I_y D_x D_z\right)$$
$$B = \lambda^2 \left(I_y I_z + \gamma^2 D_y D_z\right) - \gamma^2 \left(I_y I_z D_x^2 + I_x^2 D_y D_z - I_x I_z D_x D_y - I_x I_y D_x D_z\right)$$
$$Det_\beta = -\lambda^2 \left(I_x I_y + \gamma^2 D_x D_y\right)\overline{\alpha} + \lambda^2 \left(I_x^2 + \gamma^2 D_x^2 + \lambda^2\right)\overline{\beta} - B$$

$$Det \times (\alpha - \overline{\alpha}) = -\left[\gamma^2 \left(I_x D_y - I_y D_x\right)^2 + \lambda^2 \left(I_x^2 + \gamma^2 D_x^2\right)\right]\overline{\alpha}$$
$$\qquad - \lambda^2 \left(I_x I_y + \gamma^2 D_x D_y\right)\overline{\beta} - A$$
$$Det \times \left(\beta - \overline{\beta}\right) = -\left[\gamma^2 \left(I_x D_y - I_y D_x\right)^2 + \lambda^2 \left(I_y^2 + \gamma^2 D_y^2\right)\right]\overline{\beta}$$
$$\qquad - \lambda^2 \left(I_x I_y + \gamma^2 D_x D_y\right)\overline{\alpha} - B$$

$$\alpha^{n+1} = \overline{\alpha}^n - \frac{\left[\gamma^2 \left(I_x D_y - I_y D_x\right)^2 + \lambda^2 \left(I_x^2 + \gamma^2 D_x^2\right)\right]\overline{\alpha}^n + \lambda^2 \left(I_x I_y + \gamma^2 D_x D_y\right)\overline{\beta}^n + A}{Det}$$

$$\beta^{n+1} = \overline{\beta}^n - \frac{\lambda^2 \left(I_x I_y + \gamma^2 D_x D_y\right)\overline{\alpha}^n + \left[\gamma^2 \left(I_x D_y - I_y D_x\right)^2 + \lambda^2 \left(I_y^2 + \gamma^2 D_y^2\right)\right]\overline{\beta}^n + B}{Det}$$